

ENDOSOMAL PH MEDIATED STRUCTURAL TRANSITIONS IN ADENO-  
ASSOCIATED VIRUSES

By

BALASUBRAMANIAN VENKATAKRISHNAN

A DISSERTATION PRESENTED TO THE GRADUATE SCHOOL  
OF THE UNIVERSITY OF FLORIDA IN PARTIAL FULFILLMENT  
OF THE REQUIREMENTS FOR THE DEGREE OF  
DOCTOR OF PHILOSOPHY

UNIVERSITY OF FLORIDA

2012

© 2012 Balasubramanian Venkatakrisnan

To my mother Sujatha Venkatakrisnhan, my father Venkatakrisnhan Subramanian, my  
sister Padmaja Venkatakrisnhan and our precious Scoobie

## ACKNOWLEDGMENTS

I thank my mentors, Dr. Robert McKenna and Dr. Mavis McKenna for their guidance, patience and support. The time I have spent in their lab has gone a long way in molding me from a raw enthusiastic student to a mature researcher. They have been very involved in my professional and personal growth over the last five years. They have given me a lot of opportunity to learn and prove my abilities in their laboratory as well as in the general scientific community. I thank them for being gentle teachers and for guiding me in developing my philosophy on science and the world in general. It is my privilege to have worked with them.

I thank the past and present members of the McKenna lab for their help and collaboration. They have been of invaluable help to me in the last five years and I hope to have future collaborators and long term scientific acquaintances in them. I thank my undergraduate student Joseph Yarbrough for his help in this study.

I thank my committee members Dr. Joanna Long, Dr. Brian Cain, Dr. Linda Bloom and Dr. Nicholas Muzyczka for their guidance, critique and inputs. I could not have made it this far without the help of the administrative staff of the Biochemistry and Molecular Biology department and the IDP and I thank them for it. I thank my collaborators Dr. Shuo Qian, Dr. Lilin He (Oak Ridge National Laboratory), Dr. Richard Gillilan (Cornell University), Dr. Brian Bothner, Vamsee Rayaprolu (Montana State University), Dr. Olga Kozyreva (University of North Carolina), and Dr. Barry Byrne, Dr. Nicholas Muzyczka and Max Salganik (University of Florida) for their assistance and involvement in this study.

I thank my friends Matt Watts, Dennis Neeld, Lawrence Tartaglia and Mukundh Narayan for their support and counsel during tough times. They have been my family in Gainesville and I am grateful to them for making it a home away from home.

I thank my parents Venkatakrisnan Subramanian and Sujatha Venkatakrisnan, my sister Padmaja Venkatakrisnan and my dog Scoobie for their love and support. I am grateful for their confidence in me, their support and life lessons that have had a big role in my professional and personal development.

## TABLE OF CONTENTS

	<u>page</u>
ACKNOWLEDGMENTS.....	4
LIST OF TABLES.....	8
LIST OF FIGURES.....	9
LIST OF ABBREVIATIONS.....	11
ABSTRACT.....	15
CHAPTER	
1 BACKGROUND AND INTRODUCTION.....	17
Adeno-Associated Viruses.....	17
AAV Serotypes and their Tropisms.....	18
The Parvovirus Capsid Structure.....	19
The Infectious Pathway of AAVs.....	21
Intracellular Trafficking.....	23
VP1u Externalization.....	23
Capsid Stability and Uncoating.....	27
Overall Goals.....	29
2 MATERIALS AND METHODS.....	38
Production and Purification of AAV VLPs and Virions.....	38
AAV Capsid VLP Production in Sf9 Cells.....	38
AAV Mutant and DNA-packaged Capsid Production in HEK 293 Cells.....	39
Purification.....	39
Validation of Purified Sample Quality.....	40
Transmission Electron Microscopy (TEM).....	41
Circular Dichroism.....	41
Data Collection.....	41
Data Processing and Refinement.....	42
Secondary Structure Determination Algorithm.....	42
Differential Scanning Calorimetry.....	43
Data Collection.....	43
Data Processing and Refinement.....	44
Small-angle Scattering.....	44
X-ray Scattering Data Collection.....	44
Small-angle Neutron Scattering Data Collection.....	45
SAXS and SANS Data Processing and Refinement.....	46
X-ray Crystallography - Data Collection and Structure Determination.....	46
Protease Assays.....	47

Computational Analysis .....	48
Secondary Structure Prediction and Modeling .....	48
pI Calculations.....	49
Intrinsic Disorder Prediction.....	49
<b>3 GLOBAL CHANGES IN THE SOLUTION STRUCTURE OF AAV CAPSIDS AT DIFFERENT ENDOSOMAL PHS .....</b>	<b>54</b>
Crystal Structure of AAV8 at Different pHs .....	54
Small-angle Scattering.....	56
Results.....	57
Discussion .....	59
<b>4 STRUCTURAL AND BIOPHYSICAL ANALYSIS OF THE VP1-UNIQUE REGION ...</b>	<b>68</b>
Background.....	68
Results.....	69
Ordered Structural State of the VP1u.....	71
Loss of $\alpha$ -helicity with Increase in Temperature .....	71
Loss of $\alpha$ -helicity with Decrease in pH.....	72
Restoration of Secondary Structure .....	73
AAV5 and AAV8.....	73
Discussion .....	74
<b>5 THE ROLE OF STRUCTURAL STABILITY IN THE INFECTIVE PATHWAY OF ADENO-ASSOCIATED VIRUSES .....</b>	<b>92</b>
Background.....	92
Results.....	93
Discussion .....	95
<b>6 NOVEL PROTEOLYTIC ACTIVITY IN ADENO-ASSOCIATED VIRUSES.....</b>	<b>104</b>
Background.....	104
Results.....	104
Discussion .....	106
<b>7 SUMMARY AND FUTURE DIRECTIONS.....</b>	<b>114</b>
<b>LIST OF REFERENCES .....</b>	<b>119</b>
<b>BIOGRAPHICAL SKETCH.....</b>	<b>132</b>

## LIST OF TABLES

<u>Table</u>	<u>page</u>
1-1 Sequence similarities of the AAV serotype VP1s in comparison to AAV2.....	31
3-1 Rg values (Å) of AAV8 obtained from SANS data. All Rg values are expressed in Angstrom units.....	62
3-2 Rg values (Å) of empty VLPs from SAXS data. ....	63
4-1 Thermal VP1u structural transition temperatures (in ° C) for AAV1, AAV5 and AAV8*. The numbers in parenthesis are the errors associated with the values based on triplicate experiments.....	78
4-2 Percentage α-helicity from deconvolution of CD spectra of AAV1, AAV5 and AAV8 at different pHs. ....	79
5-1 Association energies and buried surface areas for AAV8 at pHs 7.5 and 4.0. This data was calculated using the VIPERdb server. ....	99
5-2 DSC melting temperatures (in ° C).....	100
6-1 Amino acid conservation in the catalytic triad region.....	108

## LIST OF FIGURES

<u>Figure</u>	<u>page</u>
1-1 Multiple sequence alignment of the VP1 capsid protein in AAV serotypes used in this study.....	32
1-2 AAV capsid VPs and their organization.....	33
1-3 Crystal structure of AAV1 capsid VP monomer (PDB ID: 3NG9).....	34
1-4 Interfaces of symmetry on an icosahedral AAV1 (PDB ID: 3NG9) capsid.....	35
1-5 Schematic of the AAV life cycle.....	36
1-6 Equatorial slices of wild-type AAV2 3D image reconstructions after incubation at RT and 65° C.....	37
2-1 Schematic of the production, purification and characterization of AAV empty capsid VLPs, DNA-packaged capsids and capsid mutants for further biophysical analysis.....	51
2-2 Experimental CD curves for pure $\alpha$ -helix (blue), $\beta$ -sheet (red) and random coil (green).....	52
2-3 Contrast matching in Small-angle Neutron Scattering.....	53
3-1 Conformational changes in pH quartet region with pH.....	64
3-2 Changes in AAV8 DNA propensity at A) pH 7.5 (blue) and B) pH 4.0 (purple). ....	65
3-3 Pairwise density distribution function for AAV8 VLPs at different pHs. ....	66
3-4 Pairwise distribution function of DNA containing AAV8 capsids.....	67
4-1 Cartoon rendition of superimposition of VP1u models on PLA <sub>2</sub> crystal structure. ...	80
4-2 Surface rendition of superimposition of VP1u on to the capsid monomer from the crystal structure. ....	81
4-3 PONDR-FIT plot showing intrinsic disorder in VP1/2 common region.....	82
4-4 Histogram showing pI values across all 12 AAV serotypes.....	83
4-5 CD spectrum of AAV VP1u. ....	84
4-6 CD spectrum of AAV1 empty capsid VLPs at different temperatures.....	85
4-7 Electron micrographs of the AAV1 capsid VLPs. ....	86

4-8 Plot of ellipticity values at 212 nm Vs temperature from CD experiments. ....	87
4-9 CD spectrum of AAV1 empty capsid VLPs at different pHs. ....	88
4-10 CD spectrum of empty AAV8 capsids at different pHs. ....	89
4-11 CD spectrum of empty AAV5 capsids at different pHs.. ....	90
4-12 AAV1 VP1u externalization model. ....	91
5-1 DSC curves for AAV1, AAV5 and AAV8. ....	101
5-2 Electron micrographs of AAVs 1, 5 and 8 at different pHs.. ....	102
5-3 Electron micrographs of AAVs 1,5 and 8 at different temperatures. ....	103
6-1 Western Blot of AAV2 wild type and mutants showing degradation products. ....	109
6-2 Superimposition of hypothesized aspartic protease sites (AAV2) onto catalytic aspartates of an aspartic protease (HIV1 protease). ....	110
6-3 AAV1 capsid structure.....	111
6-4 Protease activity for AAV1, AAV2, AAV5, and AAV8 at pH 7.5 and 5.5.....	112
6-5 Protease activity assay plots for AAV1, AAV2, AAV5 and AAV8 in presence of inhibitors. ....	113

## LIST OF ABBREVIATIONS

Å	Angstrom Units
AAV	Adeno-Associated Virus
ATP	Adenosine Triphosphate
Bp	base pair
°C	Degree Celsius
Ca <sup>2+</sup>	Calcium ion
CaCl <sub>2</sub>	Calcium Chloride
CASP	Critical Assessment of Techniques for Protein Structure Prediction
CD	Circular Dichroism
CHESS	Cornell High Energy Synchrotron Source
Cl <sup>-</sup>	Chloride ion
CO <sub>2</sub>	Carbon Dioxide
CPV	Canine Parvovirus
CsCl	Cesium Chloride
dAMP	Deoxy Adenosine Monophosphate
dCMP	Deoxy Cytidine Monophosphate
DEER	Double Electron-Electron Resonance
DMEM	Dulbecco's Modified Eagle Medium
DNA	Deoxy-ribonucleic acid
DSC	Differential Scanning Calorimetry
EDTA	ethylenediaminetetraacetic acid
EM	Electron Microscopy
ER	Endoplasmic Reticulum
FBS	Fetal Bovine Serum

FHV	Flock House Virus
FPLC	Fast Protein Liquid Chromatography
FRET	Forster's Resonance Energy Transfer
g	Rotational unit in terms of gravity
GE	General Electric Company
GFP	Green Fluorescent Protein
H <sup>+</sup>	Proton
HCl	Hydrochloric Acid
HEK 293	Human Embryonic Kidney 293 cell line
HFIR	High Flux Isotope Reactor
ITR	Inverted Terminal Repeats
K	Kelvin
Kb	kilobase
kDa	kilodalton
log	logarithm
M	Molar
m	meter
Mg	milligram
MgCl <sub>2</sub>	Magnesium Chloride
μL	microliter
ml	milliliter
mm	millimeter
mM	MilliMolar
mRNA	messenger ribonucleic acid
MVM	Minute Virus in Mice

MW	Molecular Weight
N	Normal (unit of concentration)
Na <sub>2</sub> HPO <sub>4</sub>	Sodium Phosphate (dibasic)
NaCl	Sodium Chloride
NH <sub>4</sub> Cl	Ammonium Chloride
NLS	Nuclear Localization Sequence
Nm	Nanometer
nM	nanoMolar
NωV	<i>Nudaurelia capensis</i> omega virus
ORF	Open Reading Frame
ORNL	Oak Ridge National Laboratory
PAGE	Polyacrylamide Gel Electrophoresis
PBS	Phosphate buffer Saline
pH	negative log of hydrogen ion concentration
pI	Isoelectric point
pKa	negative log of acid dissociation constant
PLA <sub>2</sub>	Phospholipase A <sub>2</sub>
rAAV	Recombinant Adeno-Associated Virus
<i>Rep</i>	AAV Replication protein gene
Rg	Radius of gyration
RNA	Ribonucleic acid
Rpm	Rotations Per Minute
SANS	Small-angle Neutron Scattering
SAXS	Small-angle X-ray Scattering
SDS	Sodium Dodecyl Sulfate

<i>Sf9</i>	<i>Spodoptera Frugiperda</i> (Fall Armyworm) clonal isolate cell line
SFM	Serum Free Media
ssDNA	Single stranded Deoxy-ribonucleic acid
T	Triangulation number
TM	Trademark
Tris	tris(hydroxymethyl)aminomethane
Triton X-100	polyoxyethylene octyl phenyl ether – a nonionic surfactant
UV	Ultraviolet
Vis	Visible light
VLP	Virus-Like Particle
VP	Viral protein
VP1u	VP1-unique N-terminal region
v/v	Volume per Volume
wt	wild type
w/v	Weight per Volume
X	Magnification

Abstract of Dissertation Presented to the Graduate School  
of the University of Florida in Partial Fulfillment of the  
Requirements for the Degree of Doctor of Philosophy

ENDOSOMAL PH MEDIATED STRUCTURAL TRANSITIONS IN ADENO-  
ASSOCIATED VIRUSES

By

Balasubramanian Venkatakrishnan

May 2012

Chair: Robert McKenna

Major: Medical Sciences - Biochemistry and Molecular Biology

Adeno-Associated Viruses (AAVs) are single stranded DNA viruses that belong to the *Parvoviridae* family. The AAV infective pathway involves the binding of the virus to a cell-surface receptor and subsequent clathrin-mediated endocytosis. Inside the endosome, the virus capsid undergoes structural changes that permit the virus to escape the endosome and traffick to the nucleus.

There are some clues, to what structural changes may occur, in the capsid during virus trafficking. The VP1 capsid protein contains a unique (VP1u) phospholipase A<sub>2</sub> domain (PLA<sub>2</sub>) and two nuclear localization signals. The phospholipase domain is required to remodel the endosome to allow escape and the nuclear localization signal is required for nuclear entry. While the VP1u and the VP1/2 common region are not seen in the crystal structures of the viruses, antibody assays confirm that the VP1u is not exposed on the surface of the capsid. Antibody assays have identified that heating the capsid to ~ 65° C exposes the VP1u. The externalization event has been shown to be crucial because capsids that are directly injected into the cytoplasm or the nucleus are ineffective in infection.

The cellular trigger for AAV VP1u externalization in the endosome is unknown. This study demonstrates that the VP1u is structurally ordered in solution in a predominantly  $\alpha$ -helical. This secondary structural state is transitioned by temperature and/or pH where a gradual loss of secondary structural propensity signal was seen with increasing temperature and/or decreasing pH. When the pH was restored to 7.5 the secondary structural signal was also restored.

Electron microscopy confirmed that the capsids were intact when the pH was decreased or temperature, increased. Differential Scanning Calorimetry and Small-angle scattering analysis show mild structural and stability changes in the capsid in response to pH. Small-angle Neutron Scattering analysis confirmed that there was a genomic rearrangement event that accompanied the structural changes seen in the capsid. A novel autoproteolytic activity was identified in the AAV capsids that could have a role in capsid disassembly. This data, taken as a whole, is the first physical evidence of the structural state of the VP1u during the effect of endosomal pH states.

## CHAPTER 1 BACKGROUND AND INTRODUCTION

Viruses are ubiquitous and infect everything from bacteria to humans. In order to be able to infect such a large diverse group of organisms, they are known to have evolved several strategies. These strategies are employed at every stage of the virus life cycle from host-cell recognition and intracellular trafficking, to replication, assembly and release of new progeny. These strategies have been optimized to effectively evade host defense mechanisms and use the host machinery for viral infectivity and replication. Viral infectivity is achieved despite having a relatively simple organization of a genetic material packaged by a capsid/lipid coat. The genetic material could be either DNA or RNA in single-stranded or double-stranded form. Based on the presence of a lipid membrane in the capsid coat, viruses are classified into either envelope viruses (lipid coat present) or non-envelope viruses (lipid coat absent) (39). Naturally, these differences in genetic material and coat composition lead to different strategies in host recognition, trafficking, replication, assembly and release. Since the genetic material is primarily involved in the replication process, the capsid is an important determinant of infectivity in the virus life cycle (39).

### **Adeno-Associated Viruses**

Adeno-Associated Viruses (AAVs) are ssDNA viruses of the *parvoviridae* family (64). They are non-envelope viruses that package a ~ 4.7 kb nucleotide genome (64). They belong to the Dependovirus genus and infect many different vertebrates including humans. They are nonpathogenic and replicate productively only in the presence of a helper virus, such as adenovirus or herpes virus, which supplies a number of early functions for AAV that are required for gene expression and replication (10). Like the

related autonomous parvoviruses, AAV capsids are icosahedral (approximately 260 Å in diameter) (64). The viral genome has two open reading frames (orfs), *rep* and *cap* (64). The *rep*orf codes for four overlapping proteins required for replication and DNA packaging (64). Three capsid proteins (VPs) are made from two alternately spliced mRNAs from the *cap*orf (Figure 1-1A). One of these messages contains the entire capsidorf and encodes VP1. The other mRNA encodes for VP2, from an alternate start codon (ACG), and VP3 from a conventional downstream ATG. VP3 is 61 kDa and constitutes 90% of the capsid's protein content. The less abundant capsid proteins, VP1 (87 kDa) and VP2 (73 kDa), share the same C-terminal amino acid sequence with VP3 but have additional N-terminal sequences (64). A total of 60 copies of the three viral structural proteins, VP1, VP2 and VP3, in a predicted ratio of 1:1:8/10, form the 60-subunit T=1 icosahedral viral particle (Figure 1-2B) (21). The only essential cis-active sequences in AAV are the 145 bp terminal repeats (ITRs) which function as origins for DNA replication, packaging sequences and integration sites (79). Recombinant AAV vectors (rAAV) are generated by retaining the ITRs and replacing the internal wild type (wt) AAV coding sequences with therapeutic genes (56, 79). rAAVs infect both dividing and non-dividing cells and can establish latency for the life of the animal in non-dividing cells (42).

### **AAV Serotypes and their Tropisms**

Twelve distinct human and non-human primate AAV serotypes (AAV1-12) have been sequenced to date, and numerous rAAVs have been identified in primate and human tissues through PCR studies (43, 84, 105). Their sequence similarities are described in Table 1-1. The viruses are not associated with any disease, are non-toxic, and can package and deliver foreign genes to target cells. Considerable interest has

been generated in their development as gene delivery vectors and numerous studies show that each virus has unique cellular transduction characteristics (16, 25, 43, 62, 84, 99, 121). Most of the gene therapy applications to date have been with AAV2, the most intensively studied serotype, but other serotypes have now been shown to have more promise for gene delivery to certain tissues. AAV1, for example, can transduce rodent skeletal muscle as much as a thousand-fold more efficiently than AAV2 (20) and is now in a human clinical trial for muscle delivery. AAV5 has more diverse targeting, in addition to being more efficient at transducing neuronal and lung tissues (16, 25). For the more recently discovered serotypes, AAV7 has also been shown to have superior muscle transduction compared to AAV2, while AAV8 and AAV9 are the most efficient serotypes discovered so far for transducing the liver (43, 44) and also show significant promise for muscle transduction (58, 91). Gene and protein expression by the AAVs have been shown to essentially last for the life span of the animal in numerous rodent studies, and several years in large animals (85, 101). The recent success of AAV2 mediated gene transfer for the treatment of blindness (75) highlights the potential of these vectors and generated a considerable amount of national and international media attention along with public interest in the use of AAV vectors.

### **The Parvovirus Capsid Structure**

The parvovirus VPs are capable of performing a wide variety of structural and biological functions during the viral life cycle. These functions include host cell surface receptor recognition, endosomal entry and trafficking, viral genomic encapsidation, self-assembly into capsids, maturation of virions to produce infectious virus progeny, nuclear import (for assembly) and export (after assembly) and host immune response detection and evasion (53). The relatively small parvoviral genome (~ 4.7 kb) has allowed the use

of genetic manipulation to identify functional domains/regions of the VPs/capsid.

Towards correlating these functions with structural features of the capsid in the AAV serotypes, structures have been determined for AAV1, AAV2, AAV3B, AAV4, AAV5, AAV6, AAV7, AAV8 and AAV9 (47, 72, 82, 83, 87, 88, 98, 120, 131).

A combination of sixty parvoviral VP1, 2, 3 (and 4 for the densoviruses) build up the T=1 icosahedral capsid (Figure 1-2B) in a 1:1:10 ratio (64). Only the common C-terminal VP3 region (~ 530 amino acids) is observed in crystal structures (Figure 1-3). The unique VP1 N-terminal region (VP1u), the N-terminal ~ 40-60 amino acids of VP2 that overlaps with VP1 (VP1/2-common region) and the first ~ 15-24 residues of VP3, that are located inside the assembled capsid (13, 24, 36, 119, 122) have been disordered in the crystal structures. The focus of this dissertation is mainly on the N-terminal VP1u region. This lack of N-terminal VP ordering has been attributed to the low copy numbers of VP1 and VP2 in mature capsids and to the possibility that the N-termini of VP1, VP2 and VP3 adopt different conformations in the capsid. These conformations could be averaged out from the icosahedral symmetry assumed during structure determination. Interestingly, cryo-EM studies of heat-shocked AAV2 capsids identified density “globules” located inside the capsid at the icosahedral 2-fold axis that have been interpreted as the N-terminal regions of VP1 and VP2 (69) but the structural topology of these regions remain to be elucidated.

The structural topology of the common VP region is highly conserved, even for parvovirus members that are ~ 20% or less identical at the amino acid sequence level. The VPs consist of a core eight-stranded anti-parallel  $\beta$ -barrel (designated  $\beta$ B- $\beta$ I) that forms the contiguous capsid shell, with loop insertions between the strands forming the

surface (Figure 1-3). The loops contain small stretches of  $\beta$ -strand structure and variable regions seen in all parvoviruses. The major capsid surface features include depressions at the icosahedral 2-fold symmetry axis and surrounding the 5-fold axis (blue surface regions), and protrusions at or surrounding the 3-fold axes (red surface regions). The floor of the 2-fold depression is only one polypeptide chain thick, making this the thinnest regions of the capsid (Figure 1-4A). A conserved  $\alpha$ -helix ( $\alpha$ A) forms the wall of the 2-fold depression. The 3-fold protrusions are formed from the intertwining of loops from 3-fold symmetry-related VP3 monomers and are the most variable regions within the parvovirus capsid with respect to sequence and structure (Figure 1-4B). Two small stretches of  $\beta$ -strand structure, between  $\beta$ D and  $\beta$ E, form a radial  $\beta$ -ribbon, which clustered at 5-fold icosahedral symmetry-related VPs (Figure 1-4C). This forms a conserved cylindrical channel that connects the interior to the exterior of the capsid. A structurally conserved loop between  $\beta$ H and  $\beta$ I (HI loop) forms the most extensive 5-fold related VP contacts and lies on the 5-fold surface.

### **The Infectious Pathway of AAVs**

Structural and mutational analyses have demonstrated that parvovirus host tropism, transduction properties of AAV vectors, and antigenic differences arise from variations in surface amino acids (53). Cell transduction phenotypes for the AAVs are dictated by the utilization of different cell surface glycans for cell binding and entry (53). Figure 1-5 is a simple schematic of the life cycle of the AAVs. Heparan sulfate proteoglycan, the first receptor identified for an AAV virus (116), appears to function primarily in attachment of AAV2 and AAV3 serotypes to the cell surface (89) whereas AAV1, which is ~ 83% identical to AAV2, binds both  $\alpha$  2,3 and  $\alpha$ -2,6-N-linked sialic acid but not heparin (25, 99, 129). AAV4 and AAV5, which are ~ 55% identical to each other

and to AAV2, also bind sialic acid, although AAV4 binds  $\alpha$  2,3 O-linked sialic acids, while AAV5 binds  $\alpha$ -2,3 N-linked sialic acids (62, 121). Platelet-derived growth factor receptor is the protein mediating AAV5 infection (93). AAV6, a recombinant of AAV1 and AAV2, binds both heparin sulfate and sialic acid (88, 129). The receptors utilized by AAV7-12 for cellular transduction have yet to be determined (106).

Studies aimed at deciphering AAV tissue tropism and transduction properties have utilized mutagenesis, cell binding, and transduction assays, mainly on AAV2, to identify individual capsid protein amino acid sequences that play a central role in cellular recognition and transduction. Mutagenic studies have identified the amino acids responsible for AAV2's heparin binding phenotype as R484, R487, K532, R585 and R588, with R585 and R588 being the most critical for this interaction (63, 89, 129). The availability of the high-resolution 3D structure for AAV2 (131) enabled the mapping of the AAV2 heparin-binding site. Residues are contributed from symmetry related VP monomers at the wall of the protrusions surrounding the icosahedral 3-fold axes and in the valley that runs from the 2- to 3-fold axis (63, 89, 129). Cryo-EM and image reconstruction studies of an AAV2-heparan sulfate oligosaccharide complex have confirmed the heparin-binding site at the icosahedral 3-fold axis (73). X-ray crystallographic studies of AAV5 complexed with sialic acid, glycan array analysis, and mutagenesis to map the receptor-binding site for this serotype also point to the icosahedral 3-fold axis, an analogous site to AAV2's heparan sulfate-binding region (unpublished). Interestingly, the receptor-binding site for these two viruses, which represent two of the most distantly related human AAV serotypes, is located adjacent to common variable surface loop regions on the capsid surface. Mutational analysis of the

AAV1, AAV2 and AAV8 capsids also identifies common variable regions as being involved in the determination of transduction efficiency (54, 99, 109). These observations suggest that analogous AAV capsid regions have evolved to perform similar functions. In this study, we use AAV1, AAV2, AAV5, AAV6 and AAV8 to represent the different clades in the AAVs to understand fundamental processes in the AAV life cycle.

### **Intracellular Trafficking**

The best characterized AAV with respect to cellular entry and trafficking is AAV2 (53). Once the AAV2 capsid binds heparin sulfate, entry occurs via dynamin dependent clathrin mediated endocytosis following interaction with co-receptors (108, 114). The acidic environment of the endosome is essential for virus infection, as inhibitors of the vacuolar H<sup>+</sup>-ATPases such as bafilomycin A1 or treatment of cells with NH<sub>4</sub>Cl, both inhibit AAV transduction and reduce trafficking to the nucleus (7, 30, 32, 52, 105).

### **VP1u Externalization**

Shortly after entering the early endosome, the N-termini of the minor capsid proteins VP1 and VP2 become externalized on the capsid surface while the capsid remains assembled (111). This serves two purposes; it exposes a phospholipase A<sub>2</sub> (PLA<sub>2</sub>) activity present in VP1 and nuclear localization sequences (NLSs) that are present in both VP1 and VP2 N-termini on the capsid surface. Genetic studies have shown that both the PLA<sub>2</sub> and NLS are necessary for efficient infection (12, 13, 35, 36, 77). Mutation of either region results in a 1 to 3 log reduction in infection or transduction (35, 105, 109, 122, 130). This PLA<sub>2</sub> domain has been identified in in VP1u sequence of ~ 30 different parvoviruses (17). Its sequence similarity with more potent PLA<sub>2</sub>s is very weak and is mainly restricted to the catalytic site histidine and aspartate residues and

the GXG calcium-binding motif. The parvoviral PLA<sub>2</sub> motifs lack cysteines, unlike all other previously characterized PLA<sub>2</sub>s. In contrast, multiple disulfide bonds are a hallmark of all nonparvoviral PLA<sub>2</sub>s and are used as the basis for their classification. Moreover, viral PLA<sub>2</sub>s lack the long loops between the  $\alpha$ -helices that contain the active site residues of classical PLA<sub>2</sub>s. The parvoviral PLA<sub>2</sub>s have display specific activities that are 100–1,000-fold lower than the most active PLA<sub>2</sub>s toward phospholipid vesicles (17, 110). The reasons for the relatively low activity of a subset of these PLA<sub>2</sub>s is not obvious from a comparison of their amino acid sequences of these enzymes as well as the x-ray structures of a subset of them. It is possible that the physiological substrates for these low activity enzymes have structures distinct from those of standard phospholipids.

Non-parvoviral PLA<sub>2</sub>s are known as key enzymes in lipid membrane metabolism, signal transduction pathways, inflammation, acute hypersensitivity, and degenerative diseases (4, 27, 67). They hydrolyze phospholipid substrates at the 2-acyl-ester (sn-2) position to release lysophospholipids and free fatty acids (134). Parvoviral PLA<sub>2</sub> shows the same enzymatic activity when expressed as a recombinant protein (17). The sequence similarity of non-parvoviral and parvoviral sPLA<sub>2</sub>s is largely confined to the catalytic HDXXY domain and to the calcium binding GXG motif (17). Recently, Farr *et al.* reported that polyethyleneimine (PEI)-induced endosomal rupture or co-infection with endosomolytically active adenoviruses partially rescued the infectivity of a catalytic center PLA<sub>2</sub> mutant (H42R) of the autonomously replicating parvovirus Minute Virus of Mice (MVM). They concluded that the PLA<sub>2</sub> activity plays a role in breaching the endosomal membrane to facilitate endosomal escape of incoming MVM particles (37).

Treatment of particles *in vitro* with the acidic pHs of the early endosome has been shown to induce the externalization of the VP1/2 N-terminus in autonomous canine parvovirus (CPV) and MVM (76, 111). However, acidic pHs do not induce VP1/2 N-termini extrusion in AAV2, suggesting that some combination of factors, perhaps receptor binding and pH, is necessary to cause the required capsid structural changes (111). It is possible that antibody binding is affected by change in pH in AAV2 (but not in CPV) and therefore the process of externalization needs to be studied more biophysically. A significant amount of the capsid is released into the cytoplasm: one current model is that the function of the PLA<sub>2</sub> activity is to rupture the endosome so that capsids are released (37, 111, 115), and then the NLS sequences facilitate virus trafficking to the nucleus (49, 74, 111). However, not all parvovirus PLA<sub>2</sub> activities appear to rupture endosomes in a way that would easily release virus particles. Studies with CPV showed that PLA<sub>2</sub> activity enabled the release of dextran molecules of 3kDa but not 10kDa, well below the capsid MW of ~ 4000 kDa (115). Comparative studies have shown a 3 log difference in PLA<sub>2</sub> enzymatic activity between porcine parvovirus and AAV2 (17, 115). What seems clear is that a structural change in the virus capsid, either during or early after entry, is necessary for efficient infection by promoting endosome escape, nuclear entry, and/or DNA uncoating. This structural change is at least in part responsible for the extrusion of the VP1/2 N-termini. Although the extrusion of the VP1 N-terminus is a feature common to all parvoviruses and appears to be essential for efficient infectivity, the biological mechanism that triggers this event is unclear. The channel at the 5-fold axis of the parvovirus capsid is postulated as the site of externalization of the PLA<sub>2</sub> activity and the N-termini of VP2 in capsids (134).

Mutational analysis also supports the proposal that this channel is the pore through which the viral DNA is threaded into the capsid during particle assembly (13) and release during infection (36). Although it is appreciated that capsid protein dynamics play a central role in parvovirus cell binding, entry, trafficking, DNA release, and egress following assembly, few studies have addressed this question.

Although it is generally believed that AAV is released into the cytoplasm from the endosome, a substantial portion of the capsids remain present in an endosomal compartment for 8-20 hours post infection (108, 111). The delayed onset of maximum gene expression after transduction *in vivo* (2-6 weeks) is believed to be due, at least in part, to slow trafficking to the nucleus following infection, as well as to the fact that the viral genome must synthesize a second strand prior to transcription (38, 40, 55, 99, 117). Evidence for this comes from the recent observation by the Kay group that AAV8 produced a much faster onset of expression than AAV2 in spite of both types of capsids having the same AAV2 derived recombinant genome (117). Their work and that of others suggests that AAV8 is significantly more efficient in delivering its payload to the nucleus than AAV2 and that intact capsids of AAV2 persist in infected cells for extended periods post infection prior to DNA release or degradation (55, 99, 117). During infection virus is found in the early endosome, recycling endosome, late endosome, and lysosomal fractions (7, 31, 32, 51, 52, 105, 130). One serotype, AAV5, has been observed in the Golgi (6) and is capable of transcytosis (92). The question of which virus fraction is critical for infection, the cytoplasmic or endosomal fraction, has not been resolved. A recent report suggests that the recycling endosome compartment, which becomes populated only at higher MOI, is the most efficient route for cell transduction

(31). The proteasome pathway also impacts viral infectivity. Proteasome inhibitors generally increase AAV transduction, albeit to different levels in different cell types (32, 133). This is in contrast to CPV, where proteasome inhibitors reduce infectivity (103). Another unresolved issue in parvovirus infection is the location of viral DNA uncoating. AAV accumulates around the nucleus and some intact virus is found within the nucleus (38, 111). It remains unclear if uncoating occurs in the cytoplasm or whether intact virus enters the nucleus and then uncoats; evidence for both possibilities has been presented (7, 52, 55, 76, 103, 108, 130).

### **Capsid Stability and Uncoating**

The AAV capsid is more thermally stable than most proteins. Particles remain intact at pH 4.0 and can tolerate temperatures of 65 °C for up to 60 minutes with only a modest reduction in infectivity (13). Calorimetry experiments demonstrate a unique transition that occurs at 70-80 °C, similar to that seen with MVM (24, 102). Moreover, computer analyses of buried surface and association energies at the icosahedral 2-, 3-, and 5-fold symmetry-related VP interfaces for the crystal structures of AAV2 and AAV8 revealed that the two viruses have similar values (87). Thus, the difference in onset of gene expression *in vivo* between AAV2 and AAV8 (24, 102) is likely to be due to specific variable surface features of the capsid and their cellular interactions rather than the overall stability of the capsids. This implies that in addition to the early structural changes that result in VP1/VP2 extrusion, there may be additional capsid-associated structural changes and events that are required for uncoating. Given that an endosomal acidic environment is essential for AAV infection (111) the hypothesis is that the trafficking events that occur prior to gene expression are due to subtle pH-mediated transitions of the capsid which facilitate the interaction of the virus with cellular proteins

that lead to more efficient trafficking, ubiquitination, nuclear entry, or uncoating. This study focuses on identifying, via biophysical analysis, the physiological transitions in the AAV capsids. The transition conditions include isolated capsids, receptor interaction at physiological pH, and some conditions encountered in the endocytic pathway.

The externalization of the N-terminus of VP1 for its PLA<sub>2</sub> function is important for parvovirus infectivity (24), yet as discussed above with the large number of structures available for these viruses, there is no structural information on this capsid region, other than the “globules” of density proposed as the N-terminal region of VP1 in low resolution cryo-EM density of heat-treated AAV2 (69) (Figure 1-6). All the parvovirus structures determined so far, other than for B19, suggest that N-termini of VP1 and VP2 reside inside the parvovirus virion, supporting a proposal that capsid dynamics and rearrangements must be an essential component of parvovirus trafficking to enable exposure of these domains for endosomal escape. The crystal and cryo-EM capsid structures available for these viruses represent low energy conformations since it is known that in solution both reversible fluctuations in protein domains and large-scale subunit rearrangements during maturation and infection occur for several other viruses (126). As an example, for poliovirus, exposure of the N-terminus (assayed by trypsin and *Staphylococcus* V8 protease sensitivity) upon receptor binding is essential for infectivity (41) and the VP4 polypeptide found on the inside surface of the virion is released early in infection while the particle is still intact. For many viruses, internalization and subsequent acidification of the endosome results in the rearrangement of capsid proteins (14, 33, 70, 94). These solution-based experiments show that domains of the subunit polypeptide that are clearly internal to the virion in the

crystal structure become intermittently exposed to the outer surface. Similar large-scale rearrangements are involved in the externalization of the parvovirus VP1 and VP2 N-termini. It is hypothesized that capsid protein dynamics occurs during AAV endocytosis in response to receptor/pH/environmental changes without disrupting capsid integrity.

The externalized VP2 N-terminal domain of MVM is crucial for nuclear exit of DNA-filled mature particles (76) and MVM VP2 cleavage by cellular proteases during entry removes approximately 20 N-terminal amino acids (24) in a maturation process. This rearrangement of MVM VP2 can be mimicked by heating the virus (57). For AAV2 heat is also able to expose VP1u, but unlike the autonomous parvoviruses, pH alone is unable to trigger this rearrangement as previously mentioned (57, 111). This observation suggests that there is a fundamental difference in the trafficking requirements for viruses that do not require helper function for infectivity versus those that do.

### **Overall Goals**

This study focuses on the structural transitions that occur in the AAV capsid in endosomal pH conditions. These structural changes include the externalization of the VP1u domain. Biophysical tools including small-angle scattering, Circular Dichroism (CD) and Differential Scanning Calorimetry (DSC) are used to characterize the steps in the externalization process along with the structural transitions that occur in other regions of the capsid. This study helps in the gaps in our understanding of the intracellular trafficking process in the AAVs. Additionally, it provides tools to biophysically characterize regions of the capsid that are not seen in the crystal structure. It is important to look at the stability of the capsid in synergy with these structural transitions because the capsid would have to disassemble at some point prior

to viral DNA replication. This study uses thermal stability as a parameter for structural stability of the capsid under different pH and receptor conditions.

Table 1-1. Sequence similarities of the AAV serotype VP1s in comparison to AAV2.

Serotype	Similarity
AAV1	83.70%
AAV3	89.16%
AAV4	57.30%
AAV5	57.06%
AAV6	83.65%
AAV7	82.39%
AAV8	82.20%
AAV9	81.21%

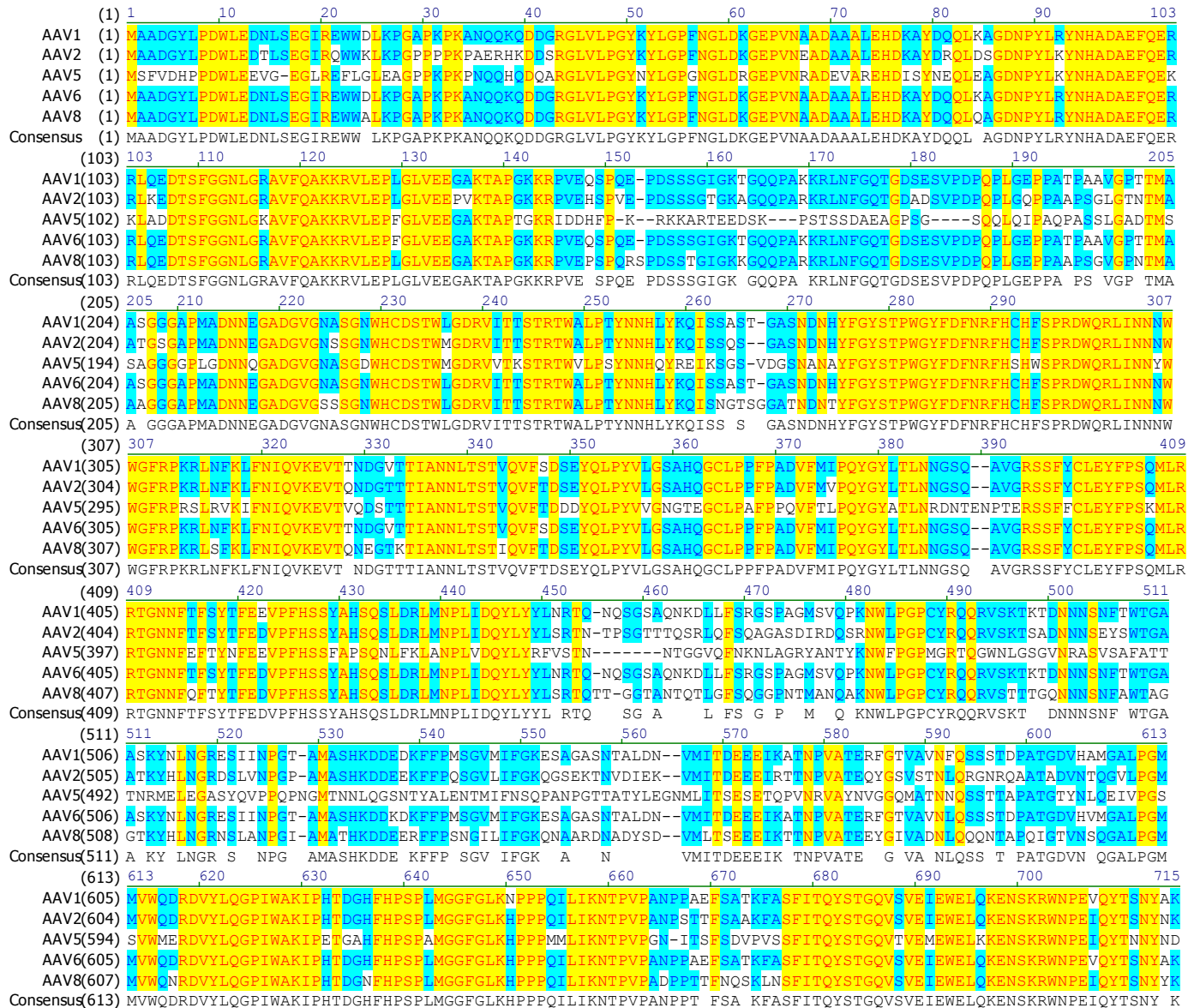


Figure 1-1. Multiple sequence alignment of the VP1 capsid protein in AAV serotypes used in this study. A sequence alignment of AAV1, AAV2, AAV5, AAV6 and AAV8 VP1 protein sequence show regions with identity (yellow) and similarity (blue). A consensus sequence is also shown below the alignment. The sequence alignment was done using ClustalW (118).

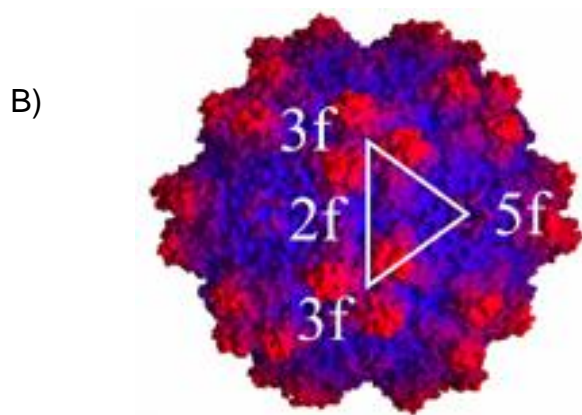
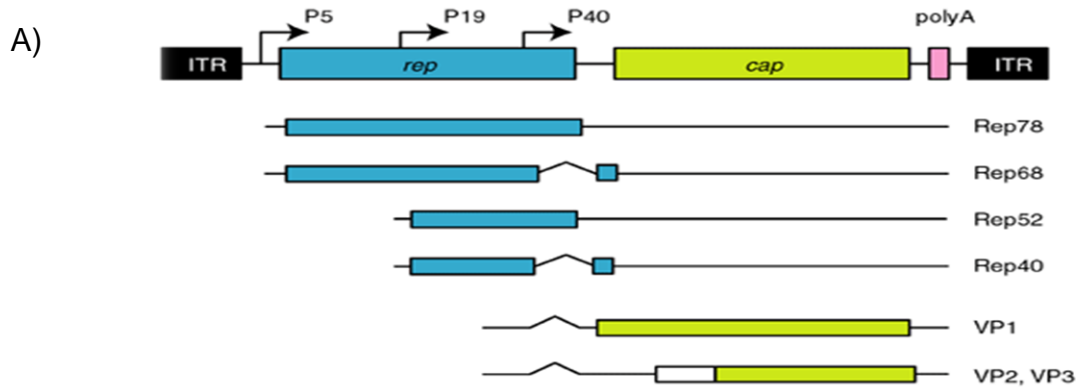


Figure 1-2. AAV capsid VPs and their organization. A) AAV capsid VPs are coded for by the same orf (*cap*) in green. The VP1 contains entire VP2 sequence and the VP1u. The VP2 contains the entire VP3 sequence and the VP1/2 common region. The other gene, *rep* (blue), and the flanking Inverted Terminal Repeat regions (ITRs) make the AAV genome. This figure has been adapted from Blechacz and Russell (2004) (11) B) The AAV1 capsid is a T = 1 icosahedral capsid made of 60 VP monomers. The 3-fold, 2-fold and 5-fold symmetrical elements are shown with surface peaks shown in red and valleys in blue.

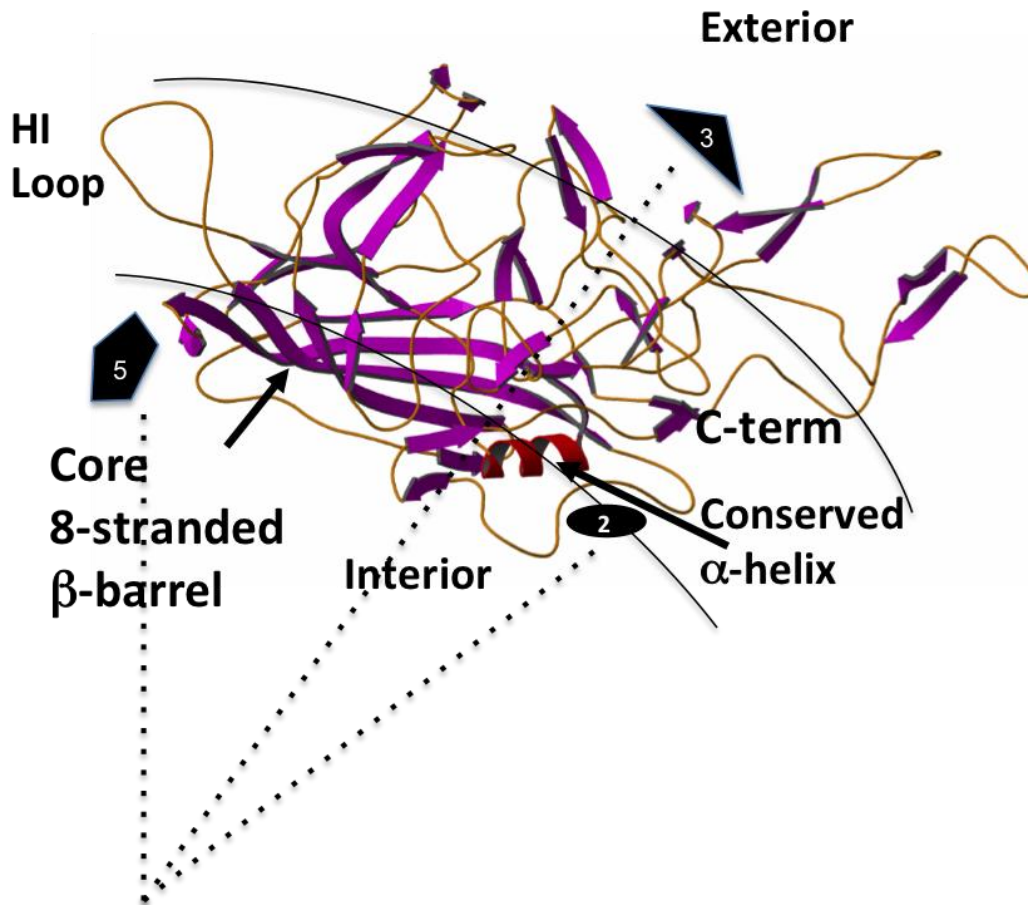
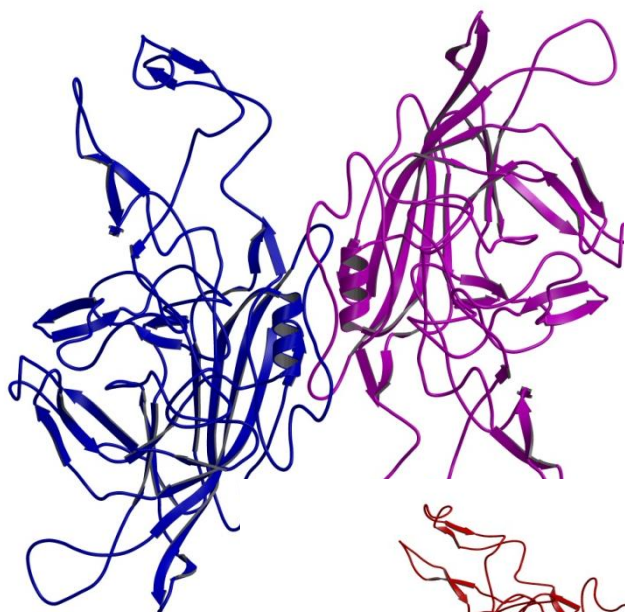
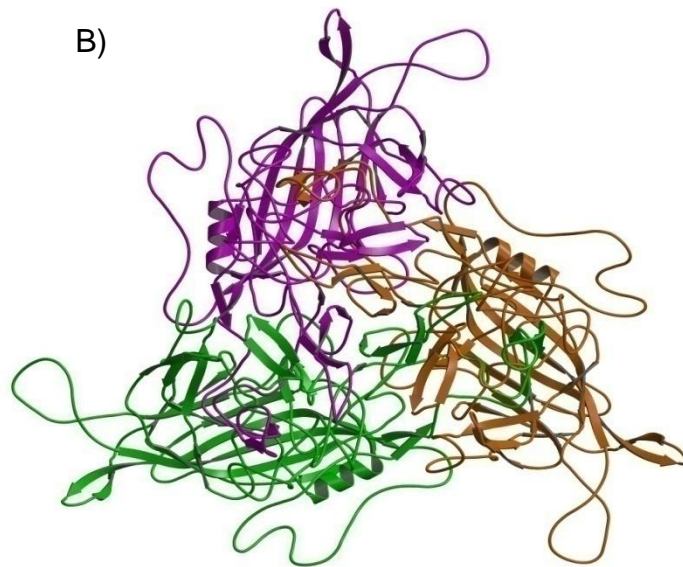


Figure 1-3. Crystal structure of AAV1 capsid VP monomer (PDB ID: 3NG9).  $\beta$ -strands are shown in purple,  $\alpha$ -helices in red and loops in orange. The dotted lines show the relative positions of the 5-fold, 3-fold and 2-fold interfaces of symmetry from the center of the capsid. A core 8-stranded  $\beta$ -barrel forms the fundamental unit of the monomer flanked by variable loop regions and other conserved regions.

A)



B)



C)

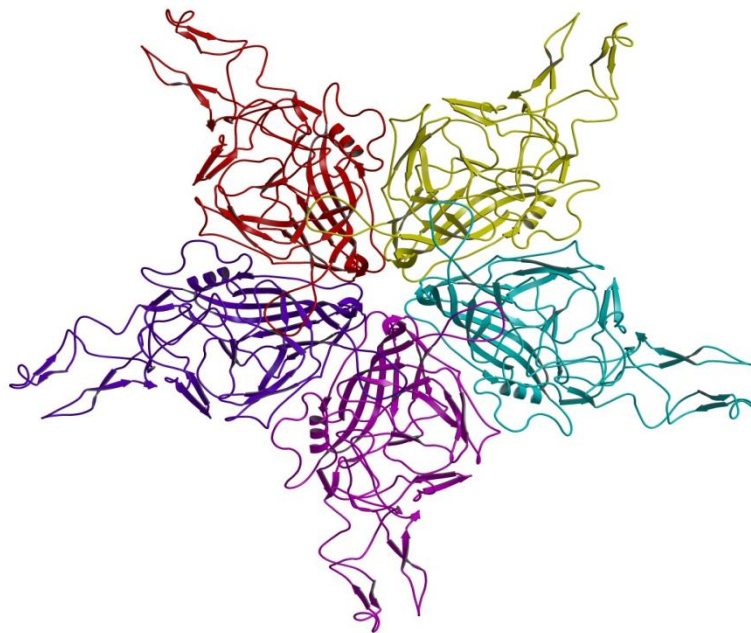


Figure 1-4. Interfaces of symmetry on an icosahedral AAV1 (PDB ID: 3NG9) capsid. A) The 2-fold interface B) The 3-fold interface C) The 5-fold interface

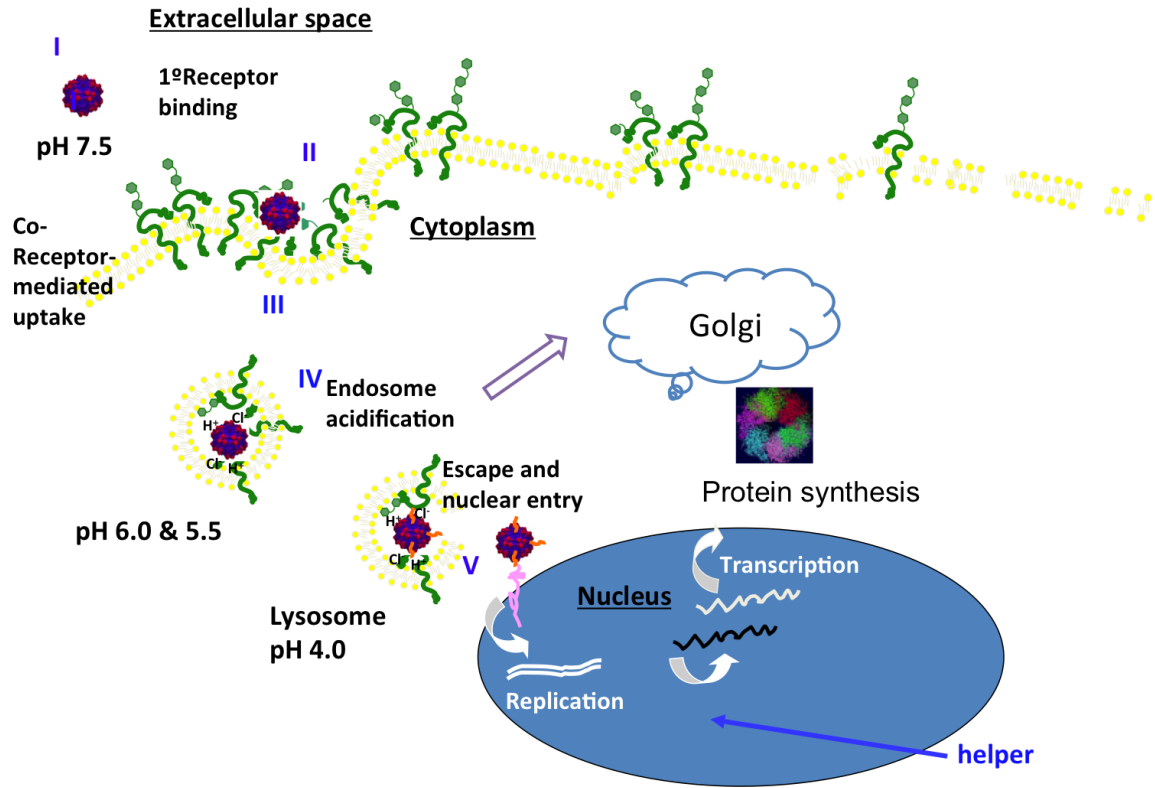


Figure 1-5. Schematic of the AAV life cycle. The AAV capsid (red and blue) trafficks to the cell surface after which it is internalized by endocytosis. It escapes the endosome and trafficks to the nucleus. Inside the nucleus the AAV genome is replicated (with helper genes from a co-infected autonomous virus) and transcribed to create more capsids that are then packaged with viral DNA inside the nucleus. Lipids are shown in yellow with cell surface receptors in green.

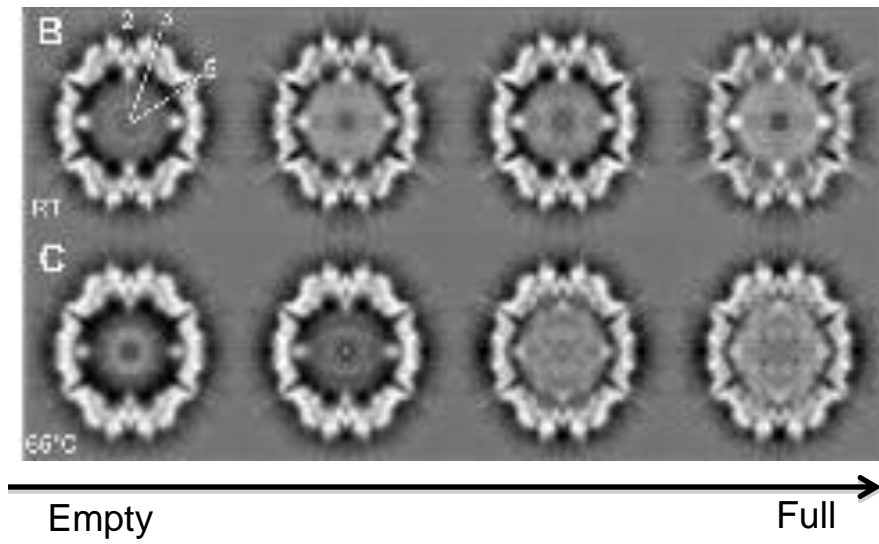


Figure 1-6. Equatorial slices of wild-type AAV2 3D image reconstructions after incubation at RT and 65° C. From left to right, the image shows empty capsids and capsids with increasing sizes of packaged DNA. This image has been adapted from Kronenberg *et al.* (69).

## CHAPTER 2 MATERIALS AND METHODS

This Chapter describes common experimental methods and reagents utilized in Chapters 3, 4, 5 and 6 of this dissertation. The first section of the Chapter describes the methods used to purify and produce large quantities of AAV VLPs and virions for subsequent experiments. The later sections describe the different experiments and assays done with the purified AAV VLPs and virions. The final section describes computational techniques and programs used in the study.

### **Production and Purification of AAV VLPs and Virions**

Depending on the quantity required and the type of sample needed, the AAV capsids were produced in either *Sf9* insect cells or HEK 293 cells. The cells were subsequently lysed and the VLPs or virions were purified from them.

#### **AAV Capsid VLP Production in *Sf9* Cells**

*Sf9* cells were used to produce AAV capsid VLPs that did not encapsidate DNA. Recombinant baculoviral vectors for AAV1, AAV2, AAV5, AAV6 and AAV8 were used to create the respective capsid VLPs. These vectors were transposed into *Sf9* cells and harvested 72 hours post transfection. The recombinant baculoviral vectors were a gift from the lab of Dr. Sergei Zolotukin (University of Florida). The cells were infected at a multiplicity of infection of 5.0 plaque-forming units per cell. The cells were grown in Erlenmeyer flasks at 300 K using Sf-900 II SFM media (Gibco/Invitrogen Corporation). The culture was then centrifuged at low speed (3000 rpm) to harvest and pellet the cells and the pellet was frozen before lysis and purification.

## **AAV Mutant and DNA-packaged Capsid Production in HEK 293 Cells**

HEK 293 cells were maintained in DMEM supplemented with penicillin and streptomycin at 100 U/ml and 10% FBS and they were maintained in 15 ml petri dishes at 37° C and 5% CO<sub>2</sub>. 40 such plates (one cell factory) were used to produce enough quantity of the AAV mutant VLP. The cells were passaged to achieve 75% confluence the next day. Each plate was then transfected with three different plasmids pIM45 (18 µg), pXX6 (54µg) and UF11 (18 µg). pIM45 was used to code for the capsid VP proteins. pXX6, contained the Ad helper genes needed for successful infection. UF11 contained the GFP gene driven by the CMV promoter and AAV terminal repeats. The UF11 was included to produce AAV capsids with packaged DNA coding for GFP. The plasmids were CsCl purified and used to transfect the cells by calcium phosphate precipitation and incubated for 48 hours at 37° C. The cells were then harvested by centrifugation at 1140g for 20 minutes and the pellet resuspended in 1 ml lysis buffer (1xTD with protease inhibitor cocktail). The sample was then freeze-thawed 3 times, treated with Benzonase for 30 minutes at 37° C and the cell lysate clarified by centrifugation at 3700xg for 20 minutes.

### **Purification**

A complete schematic representation of the purification process is shown in Figure 2-1. The cells were lysed by three freeze-thaw cycles in lysis buffer (50 mM Tris-HCl pH 8.0, 100 mM NaCl, 1 mM EDTA, 0.2% Triton X-100) with Benzonase added after the second cycle to remove the nucleic acid content. The sample was then centrifuged at 12100g in a Beckmann J2 centrifuge for 15 minutes at 4° C to separate the virus capsids from the cell debris. The virus capsids were then pelleted by sucrose cushion (20% w/v sucrose in 50 mM Tris, 100 mM NaCl, 1 mM EDTA and 0.2% Triton

X-100) centrifugation at 149,000 g for 3 hours at 4°C in vacuum using a 70Ti rotor. The pellet was further purified by sucrose gradient (10-40% w/v sucrose in 25 mM Tris, 100 mM NaCl, 0.2% Triton X-100 and 2 mM MgCl<sub>2</sub>) centrifugation at 151,000g for 3 hours at 4° C in vacuum using a SW41Ti rotor. For AAV2, the supernatant was then loaded onto a 15-60% iodixanol step gradient. The iodixanol gradient was then centrifuged at 55000rpm for 2 hours. For some of the samples requiring additional purification, a HiTrap™ Q column (GE Healthcare) chromatography step was used in an FPLC setup. 1 ml fractions of the eluate were collected from the column and chromatograms were used to select the fractions that contained the purified VLPs or virions.

### **Validation of Purified Sample Quality**

The purified samples were validated by UV/Vis Spectrometry (260/280/310 nm) in quartz cuvettes with 1 cm path length to check for protein content using the equation

$$A = \epsilon cl$$

Where A is the measured absorbance, c is the concentration, l is the path length of the cuvette used and  $\epsilon$  is the molar extinction coefficient (1.7 for empty AAV capsid VLPs for concentration in mg/ml). 10% SDS-PAGE stained with Coomassie blue stain was used to check for protein purity. Electron microscopy (50,000X) was used to check for capsid integrity. The purified samples were then exchanged into desired buffers. These protocols have been described previously (135). The samples were then buffer exchanged by either dialysis or filter centrifugation into Phosphate-Citrate buffers (with 150 mM NaCl) using specific ratios of 0.2 M Na<sub>2</sub>HPO<sub>4</sub> and 0.1 M Citrate to final pHs of 7.5, 6.0, 5.5 and 4.0. 100,000 kDa cutoff Apollo centrifugal concentrators (Orbital Biosciences) were used for the filter centrifugation.

## **Transmission Electron Microscopy (TEM)**

After buffer exchanging, 5  $\mu\text{L}$  of sample was loaded onto a carbon coated copper grid and allowed to settle for 5 minutes. The drop was then drained off the grid using a Wattmann filter paper and the grid was washed with 6-8 drops of ddH<sub>2</sub>O. The grid was then negatively stained with 5  $\mu\text{L}$  Nano-W (Nanoprobes) stain for 1 minute after which the excess stain was drained using a Wattmann filter paper. The grid was then examined in a JOEL 1200 EX transmission electron microscope at 50,000X magnification to check for capsid integrity.

## **Circular Dichroism**

CD is a spectrophotometric technique used to determine the secondary structural state of a protein. It is based on the differential absorption of left and right circularly polarized light by a protein. Based on the secondary structural state, different proteins absorb circularly polarized light differently in the near UV region (180-260 nm). The absorption spectrum is then deconvoluted mathematically to determine the amino-acid fractional content of secondary structural elements in the protein.

## **Data Collection**

All the CD experiments were done on an Aviv model 410 Circular Dichroism Spectrometer. All the data was collected between the wavelengths of 200 and 260 nm with sample concentrations of 0.4 mg/ml in triplicates with 50 scans per experiment taken at 30° C. For experiments that measured the thermal transition temperatures of the AAVs, CD spectra were collected between 200 and 260 nm between 30° C to 90° C with three degree intervals (21 spectra). 1 scan was collected for every wavelength (61 total scans) and this scan was averaged over a 5 second exposure time. Quartz cuvettes with 350  $\mu\text{L}$  volumes and 1 mm path-lengths were used. It was observed that

data collected below 200 nm was very noisy and hence the lower wavelength limit was restricted to 200 nm. In-house programs were used to deconvolute the data and estimate the degree of secondary structure in the samples.

### **Data Processing and Refinement**

The data collected in triplicate was averaged across the 50 scans and the triplicate experiments to improve the signal to noise. The averaged data was then scaled to molar ellipticity values to account for concentration and to compare with other CD spectra.

### **Secondary Structure Determination Algorithm**

CD data collection below 200 nm wavelength drastically overloaded the dynode and created large variation in the data accompanied by large error values. Therefore all the data was collected between 260-200 nm. Standard CD deconvolution programs require data collected to at least 190 nm and therefore these programs could not be used to deconvolute the data. For this CD data for pure  $\alpha$ -helix,  $\beta$ -sheet and random coil structures of poly-lysine were taken from data published by Greenfield and Fasman (Figure 2-2) (48) and used to generate an array of CD spectra corresponding to theoretical combinations of  $\alpha$ -helix,  $\beta$ -sheet and random coil between 0-100% with 10% intervals using the following equation:

$$\theta = \alpha\theta(\alpha) + \beta\theta(\beta) + \gamma\theta(\gamma)$$

Where  $\alpha$ ,  $\beta$ , and  $\gamma$  are the percentage (by residue) of  $\alpha$ -helix,  $\beta$ -sheet and random coil content in the sample respectively and  $\theta$  is the calculated resultant molar ellipticity.  $\theta(\alpha)$ ,  $\theta(\beta)$  and  $\theta(\gamma)$  are the measured molar ellipticities for a pure  $\alpha$ -helix,  $\beta$ -sheet and random coil respectively. This gave 66 possible combinations of  $\alpha$ -helix,  $\beta$ -sheet and random coil compositions.

For each experimental data set, the theoretical CD data was first scaled (by individual wavelength) to the experimental data. The experimental data was then fitted to each of the theoretical data sets and the best fit was determined by the least squares technique using the following equation:

$$f = \sum_{\lambda} (\theta_{\lambda}^2 - (\delta_{\lambda}\theta'_{\lambda})^2)$$

Where  $f$  is the least squares fit value,  $\theta$  is the calculated resultant molar ellipticity,  $\theta'$  is the experimental molar ellipticity, and  $\delta$  is its calculated scale factor corresponding to the wavelength  $\lambda$ . The scale factor  $\delta$ , was calculated using the following equation:

$$\delta_{\lambda} = \frac{\theta''_{\lambda}}{\theta'_{\lambda}}$$

Where  $\delta$  is the scale factor corresponding to the wavelength  $\lambda$ ,  $\theta'$  is the experimental molar ellipticity and  $\theta''$  is the calculated molar ellipticity averaged over the 66 possible combinations of  $\alpha$ -helix,  $\beta$ -sheet and random coil propensities.

### **Differential Scanning Calorimetry**

DSC is a calorimetry technique that measures the amount of heat required to raise the temperature of the sample by one degree. This value is directly compared to a reference buffer and the difference in heat required is plotted against temperature. This technique is useful in identifying thermal transition points and transition temperatures.

#### **Data Collection**

The DSC experiments were carried out on a MicroCal VP-DSC machine between temperatures of 10 and 100° C with sample concentrations of 0.7 mg/ml in triplicates. The sample and the buffer were loaded in the two different chambers in the machine. The data collected was plotted and analyzed using the Origin software suite (OriginLab).

## **Data Processing and Refinement**

The triplicate DSC data was averaged to improve the signal to noise ratio. The baseline was to remove background noise. Averaged data was used to calculate standard deviations, which provided error values.

## **Small-angle Scattering**

Small-angle scattering is a solution-based scattering technique that involves the deflection of light by the molecules in the solution by small angles ( $>10^\circ$ ). Based on the observed scatter, the size, shape and the orientation of the particles in solution can be determined at low resolution. It is used to observe and analyze multimeric assemblies of macromolecules and track global structural changes that occur in them.

## **X-ray Scattering Data Collection**

Some control Small-angle X-ray Scattering (SAXS) data was collected at ORNL to verify some of the Small-angle Neutron Scattering (SANS) results. The remainder of the SAXS data was collected at the Cornell High Energy Synchrotron Source (CHESS) using the Macromolecular Diffraction at CHESS (MacCHESS) facility on the G-1 beam line. 2 mg/ml sample concentrations were used with 30  $\mu\text{L}$  sample volume in plastic cuvettes. The wavelength used was 1.296  $\text{\AA}$  with a detector distance of 1210 mm. Exposure times of 1 and 5 seconds were used with 10X and 20X attenuation levels to achieve optimum signal to noise ratio while at the same time having minimal radiation damage to the sample. The data was collected between  $q$  of 0.001 and 0.275  $\text{\AA}^{-1}$ . The images were processed for intensity and  $q$  values using DATASQUEEZE (University of Pennsylvania).

## Small-angle Neutron Scattering Data Collection

All the SANS data was collected in two separate data collection trips at the BioSANS beam line of the High Flux Isotope Reactor (HFIR) source at Oak Ridge National Labs (ORNL). Quartz “banjo” cuvettes with 300  $\mu\text{L}$  sample volumes were used for data collection. The data was collected at a wavelength of 6  $\text{\AA}$  with a wavelength spread of 0.14. Sample to detector distances were between 6.8 to 1 m to achieve a  $q$  range of 0.0065 - 0.35  $\text{\AA}^{-1}$ . Samples were concentrated to 2 mg/ml concentration prior to the data collection. Since neutron scattering is non-destructive to the sample, it is possible to collect data over large time periods to compensate for the low flux of neutron beam lines. However the data collection times in these experiments were limited by the amount of user beam line time available.

In order to distinguish between the protein and the nucleic acid SANS signal in the sample, a technique called contrast variation was employed. When the  $\text{D}_2\text{O}$  concentration in the sample buffer was increased the sample scattering length density increased due to the increased coherent scattering by the deuterium in buffer. This is illustrated in Figure 2-3. At  $\sim 12\%$   $\text{D}_2\text{O}$  concentration, the buffer signal would match the signal from the lipid content in the sample. At  $\sim 42\%$   $\text{D}_2\text{O}$ , the buffer signal would match the signal from the protein concentration in the sample. This is a result of the difference in the amount of exchangeable hydrogen atoms available in lipids, proteins and nucleic acids. Proteins have more exchangeable hydrogen atoms than lipids and nucleic acids have more exchangeable hydrogen atoms than proteins. This leads to differences in their scattering ability (Figure 2-3). The samples and buffers used for contrast variation contained 42%  $\text{D}_2\text{O}$ . Subtracting the buffer signal from the sample signal would therefore retain SANS signals that arise only from the DNA content in the sample.

## **SAXS and SANS Data Processing and Refinement**

The ATSAS suite of programs was used to further process the data after raw image processing (136). GNUPLOT was used for data plotting and radius of gyration (R<sub>g</sub>) calculations. Pairwise distribution functions and radius of gyration values were calculated using the GNOM program from the ATSAS suite. DAMMIN was used to generate the 3-dimensional *ab initio* model. Ten DAMMIN simulations were averaged using the DAMAVER program to generate a final model. This model was converted to a SITUS volume map for docking purposes and the models were docked manually into the map using the CHIMERA program (96). Theoretical SAXS curves from the crystal structures of the monomer and the dimer were computed using the CRY SOL. GNOM, DAMMIN, DAMAVER, and CRY SOL are all located within the ATSAS suite.

### **X-ray Crystallography - Data Collection and Structure Determination**

Structure determination by X-ray crystallography would provide the highest resolution view of the structural features of the viral capsid. Crystallization conditions were already available for the AAV capsids and several structures have been previously determined as described in Chapter 1. This study included the structure determination and analysis of AAV5 capsids at the different endosomal pHs.

Crystal screens were set up using the hanging-drop vapor-diffusion method (81) with VDX 24-well plates and siliconized cover slips (Hampton Research, Laguna Niguel, CA, USA). The crystallization drops contained 2  $\mu$ l sample solution (at ~ 10 mg/ml) and 2  $\mu$ l precipitant solution equilibrated against 1 ml precipitant solution. AAV5 crystallization conditions were screened against precipitant solutions containing varying polyethylene glycol (PEG) 8000 (0.5–2.5%), NaCl (250 and 350 mM) and MgCl<sub>2</sub> (5–20 mM) concentrations and a pH range (pH 6.0–8.5) at room temperature (RT) and 277 K.

A buffer concentration of 20 mM for both Bis-Tris (pH 6.0 and 6.5) and Tris–HCl (pH 7.0–8.5) was used for the pH screens.

All the diffraction data was collected at the CHESS F1 beam line. The images were collected at 0.3° oscillation angles with ~ 30 images collected per crystal used with exposure times of 30-45 seconds. The data was collected at a wavelength of 0.97 Å with a 400 mm crystal-to-detector distance. Multiple crystals were used to collect the data and were scaled together after image processing, in order to get enough completeness (at least 60%). The collected diffraction images were processed using *HKL2000* (90). *SCALEPACK* was used to scale different data-sets together and generate the structure factor files (90). All structures were at a resolution of 3.5 Å while the completeness values after scaling were 65% (pH 6.0) 63.2% (pH 5.5) and 45.2% (pH 4.0). The corresponding  $R_{\text{symm}}$  values were 15.3%, 17.2% and 12.5% respectively. The CCP4 suite was used for molecular replacement (137) with the previously solved AAV5 structure as the model (unpublished). All subsequent model refinements were done using the CNS suite of programs (15). AAV5 has non-crystallographic symmetry (NCS) due to the icosahedral nature of the capsid. In order to improve the quality of the data, the refinement process using CNS involved non-crystallographic averaging as well. The data was refined to final R-factor values of 23.1% (pH 6.0), 24.5% (pH 5.5) and 26.3% (pH 4.0). *COOT* was used to visualize and manually refine the models (34). *PyMOL* (DeLano Scientific) and *CHIMERA* (96) were used to visualize the models.

### **Protease Assays**

The protease activity of the VLPs, GFP-coding DNA packaged AAV8, and controls (the serine protease Trypsin (as the positive control) and buffer and enzyme

carbonic anhydrase (as the negative control)) were determined using the PDQ™ (Protease Determine Quick) Protease Assay (Athena enzyme systems).

The PDQ™ Protease Assay is a colorimetric assay used to detect protease activity in aqueous samples. The proprietary substrate is a casein derivative entrapped in a cross-linked matrix with a dye conjugate that responds to a wide range of proteases including serine, metallo-, aspartate and cysteine proteases.

500 µL of each of the VLPs samples (0.1 mg/ml, 30 nM) and molar equivalent amounts of Trypsin and carbonic anhydrase were used for each measurement. Each sample was loaded into the assay vial containing an immobilized proteolytic substrate, at pH 7.5 and 5.5. After specific incubation (1, 2, 3, 4 and 5 hours) times (80) at 37 °C, the reaction was arrested by adding 500 µL of 0.2 N NaOH to the reaction vial. The supernatant solution from the vial was then centrifuged and measured for absorbance on a Beckmann UV-Vis Spectrometer at 450 nm. These experiments were then repeated with protease inhibition, using a cocktail of protease inhibitors (Halt™ Protease inhibitor Single-Use Cocktail from Thermo Scientific) at 10 µL/ml v/v ratio included in the reaction vial. Each experiment was repeated 3 times and the average measured value was used. Errors bars used were the standard deviations of the measurements.

## **Computational Analysis**

### **Secondary Structure Prediction and Modeling**

Predicted models of the VP1/2 N-terminal region were generated using the ROBETTA full-chain protein structure prediction server (65). ROBETTA uses an automated sequence-based structure prediction tool. It uses sequence homology to build homology models for known domains and then uses a *de novo* structure prediction method for domains with no known homology. PyMOL (26) and Coot (34) were used to

structurally superimpose, visualize and generate images of the models. PROCHECK (71) was used to resolve the secondary structural propensity of the models at an amino-acid level. These values were used to theoretically estimate the percentage secondary structure to compare with experimental CD data.

### **pI Calculations**

The ExPASy Compute pI/Mw tool (45) was used to calculate pI values for individual capsid domains and in-house algorithms were used for subsequent calculations for the whole capsid. A pI value of 5.0 was used for DNA to calculate net pI values for capsids with genomic or GFP-coding DNA (22). Capsid monomer copy numbers (VP1:VP2:VP3 1:1:10) were used to scale these values.

### **Intrinsic Disorder Prediction**

The PONDR-Fit algorithm was used to calculate the intrinsic disorder disposition in the capsid proteins (132). PONDR-Fit is a meta predictor because the prediction results from a collection of predictors is used as the input for the PONDR-Fit algorithm. This approach would improve its prediction accuracy as the different intrinsic disorder predictors that it uses for its input data base their predictions on different sequence features and different training models.

Intrinsically disordered protein sequences are typically characterized by a low number of bulky hydrophobic residues with several stretches of polar or charged amino acid residues. The intrinsic disorder results from an inability to fold in such a manner that the hydrophobic regions of the protein form the buried core of the structure. These sequence signatures are used by the PONDR-Fit algorithm to calculate a numerical intrinsic disorder disposition value. This value was plotted against residue number for different AAVs. The plot was scaled by sequence alignment to the AAV1 VP1 sequence

to better compare the different regions on the capsid monomer. Known proteins like Carbonic Anhydrase (no intrinsic disorder – negative control) and calcineurin (intrinsically disordered – positive control) were used to check if the predictions from the algorithm were valid.

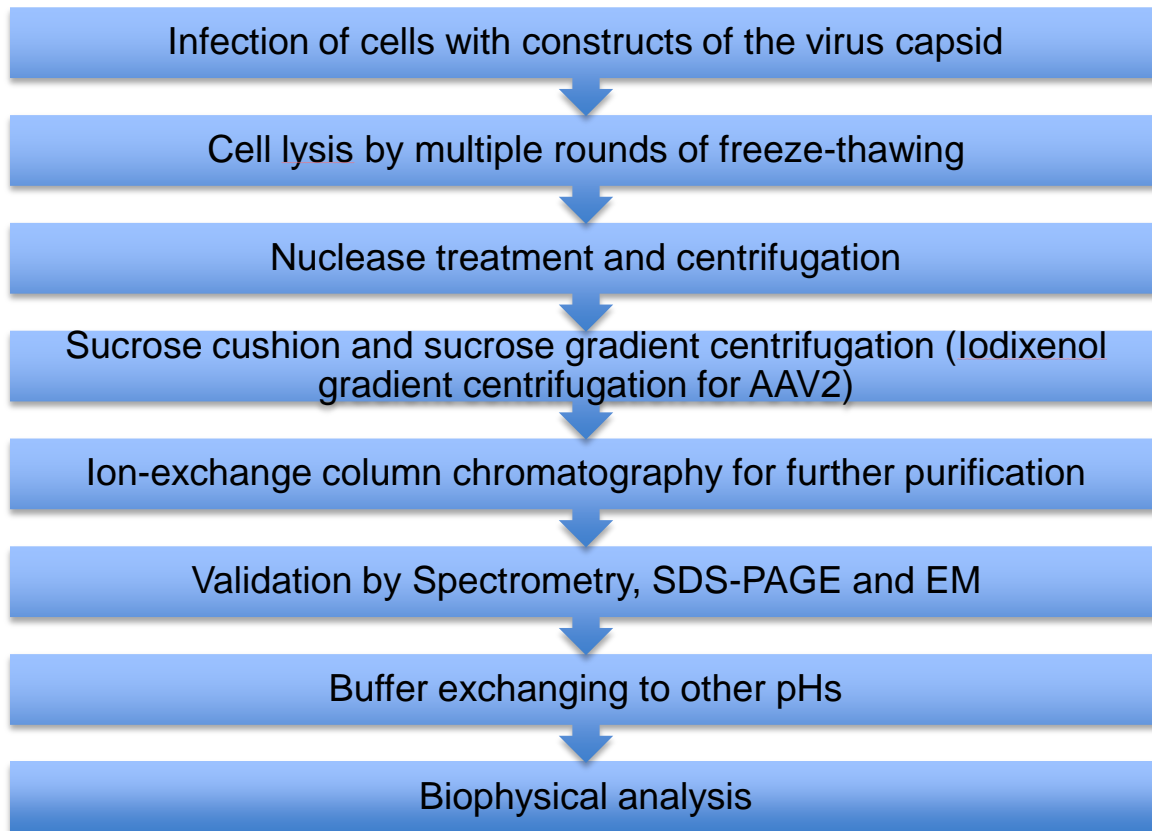


Figure 2-1. Schematic of the production, purification and characterization of AAV empty capsid VLPs, DNA-packaged capsids and capsid mutants for further biophysical analysis

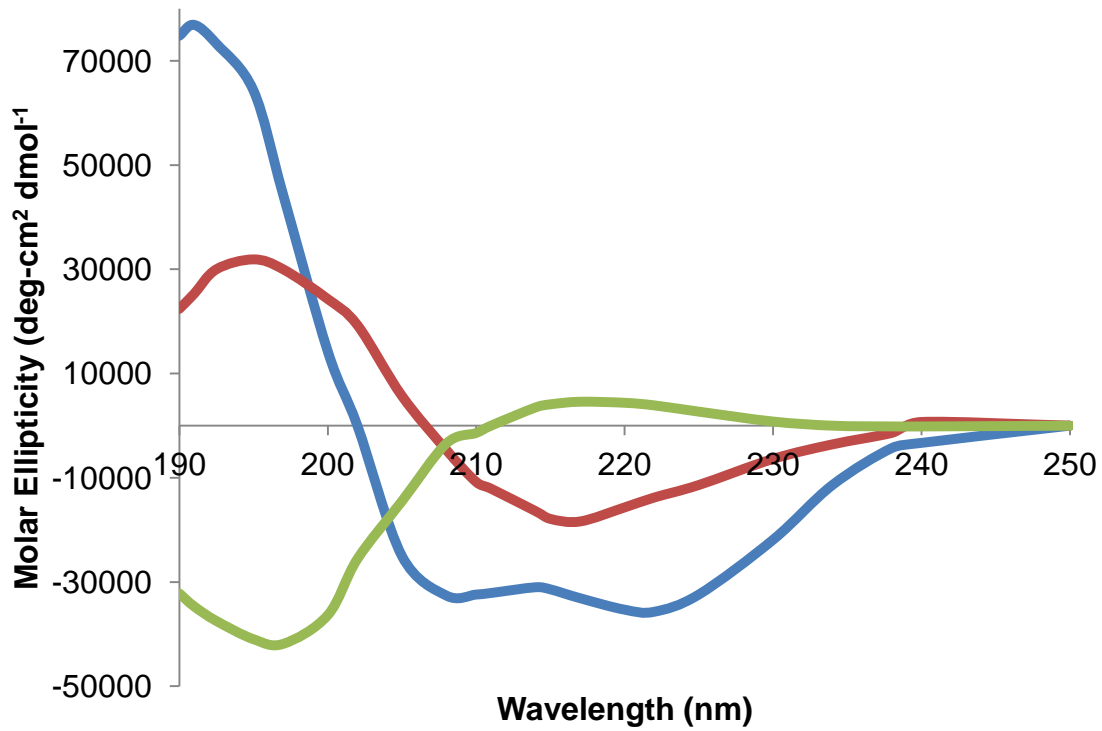


Figure 2-2. Experimental CD curves for pure  $\alpha$ -helix (blue),  $\beta$ -sheet (red) and random coil (green). Values for these curves are taken from Greenfield and Fasman (1969) (48).

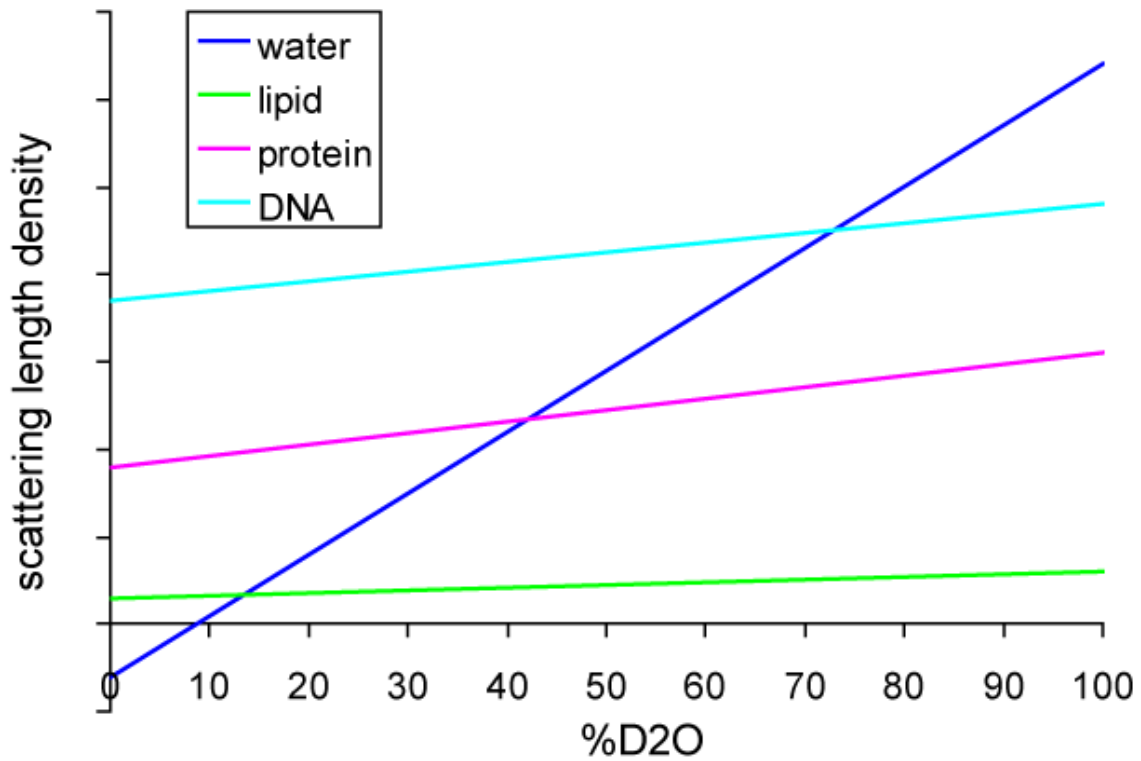


Figure 2-3. Contrast matching in Small-angle Neutron Scattering. A plot of scattering length density Vs percentage concentration of D<sub>2</sub>O in the sample shows that the buffers prepared with 42% D<sub>2</sub>O concentration would match the scattering length density of protein in the sample.

## CHAPTER 3

### GLOBAL CHANGES IN THE SOLUTION STRUCTURE OF AAV CAPSIDS AT DIFFERENT ENDOSOMAL PHS

The Parvovirus capsids are known to undergo structural transitions at different endosomal pHs (53, 85, 109). While it is known that pH alone does not induce these transitions in AAV capsids based on antibody binding assays (111), there may be some (but not all) transitions that do occur in the capsids in response to endosomal acidification.

#### **Crystal Structure of AAV8 at Different pHs**

Crystal structures of AAV8 VLPs and rAAV8-GFP capsids have been previously determined at pH values that mimic the conditions (7.5, 6.0, 5.5 and 4.0) encountered by AAVs during trafficking through the endocytic pathway and the low acidic pH of the lysosome (86). These structures did not show any global changes (corresponding to VP1u externalization) in capsid and retained the space group and unit cell parameters of the structure at pH 7.5. This could be an effect of crystal lattice constraints and steric hindrance. However there were some changes observed in side chain conformation at the different pHs (86). Changes were observed at surface residues R392, Y707, E566, and H529 and were termed as the “pH quartet” (Figure 3-1) (86).

At pH 7.5, the side chain of E566 is in position to form two hydrogen bonds with R392 from a 3-fold-related monomer and a hydrogen bond with the hydroxyl group of Y707 from a 2-fold-related monomer interface. However, as the pH was lowered to 6.0, 5.5, and 4.0, the side chain of E566 was seen to adopt an alternative conformation that facilitates the formation of a hydrogen bond with the imidazole side chain of H529. This lower pH induced interaction is most likely due to a protonation of H529, with a pKa of 6.2, which is now able to donate a hydrogen to the interaction.

The conformational change of E566 at the lower pH results in the loss of interactions with the 3-fold-related R392 and the 2-fold-related Y707 and as a consequence, reduces the inter-subunit contacts between the VP monomers. Concomitant with the change at E566, the side chain of Y707 becomes oriented toward the 2-fold axis. Finally, in the crystal structure of AAV8 where the pH was decreased to 4.0 and then increased back to 7.5, the transitions are reversed to the conformations observed at pH 7.5 (86).

Density consistent with a single dAMP nucleotide was ordered in the interior of the AAV8 VLP structure determined at pH 7.5 (87). For the rAAV8-GFP structures, densities consistent with two connected nucleotides were ordered inside the capsid at pH 7.5 and 6.0, which could be modeled as a dAMP and dCMP dinucleotide (86). The DNA densities in both the VLP and rAAV8-GFP structures became less ordered as the crystal condition was decreased to pH 5.5 and were lost at pH 4.0 (Figure 3-2). The dAMP density was restored when the pH was restored to 7.5, suggesting that the lack of ordering at pH 4.0 was likely due to disrupted interactions with VP3 amino acids with the decreasing pH.

The disappearance of the densities for the dAMP and dinucleotide in the structures of AAV8 VLPs and rAAV8-GFP, respectively, with decreasing pH values was concomitant with the H632 side chain shift described above. These observations taken together would suggest that pH was disrupting the interactions between the capsid and its encapsidated DNA. It is possible that the loss of density for DNA at low pH may be part of a structural rearrangement of the genomic DNA to prepare it for capsid disassembly and DNA ejection/release.

Previous studies suggest, based on antibody assays, that pH alone does not induce the exposure of the VP1u region of the capsid (69, 111). However, while the antibodies may bind to the VP1u at physiological pH, the binding of antibodies to the epitopes on the capsid can be affected by pH change. For example, the epitope for the A1 antibody directed towards the VP1u region has a linear epitope KRVLEPLGL (residues 123-131 by AAV1 numbering) that contains charged residues that could affect the binding of the antibody pH levels lower than physiological pH. Therefore, the lack of VP1u detection by antibodies at lower pH may be a result of ineffective antibody binding rather than a lack of exposure of the VP1u region.

In this chapter Small-angle X-ray Scattering and Small-angle Neutron scattering are used to probe radial changes in the mass distribution of AAV1, AAV5 and AAV8 capsids to confirm if there are changes in arrangement of DNA packaged inside the capsid and if there is a structural change in the VP1u region in response to decrease in pH from 7.5 (physiological) to 4.0 (lysosome). There have been previous studies that have used Small-angle X-ray scattering to observe pH-dependent structural changes in viral capsids. Capsid maturation in *Nudaurelia capensis* omega virus (NwV) involved a ~ 60 Å shrinkage of the T = 4 capsid in response to decrease in pH from 7.0 to 4.5 (78). The large conformational changes occurring in the capsid in response to pH change were tracked using Small-angle X-ray Scattering.

### **Small-angle Scattering**

The method of contrast variation has been described in the SANS section of Chapter 2. Briefly, contrast variation can be used in SANS to observe changes in DNA independent of the protein content in the sample. This permits the elimination of the capsid signal in the SANS data and allows for direct detection of genomic DNA

rearrangement in the capsid in response to pH changes. Small-angle X-ray scattering was used to track other global changes in the virus capsid as well as for control experiments. Very little SANS data is available on the parvoviruses. A study on the Kilham Rat Virus (127) determined the radius of gyration value for the virus to be 105 Å in D<sub>2</sub>O and 104 Å in H<sub>2</sub>O. They used SANS to propose that the virus had a triangulation number of 1 (T=1) and also proposed that the capsid had an inner and outer shell with all three capsid proteins contributing to the inner shell. This may have been the first small-angle scattering documentation of the VP1u region in a parvovirus. Very little structural information exists on the ssDNA structure inside the capsid.

## Results

X-ray crystallographic analysis (method described in detail in Chapter 2) of AAV5 capsids at different endosomal pHs (7.5, 6.0, 5.5 and 4.0) showed no significant changes in the secondary structural state of any amino-acid side chains (including residues corresponding to R392, E566 and Y707 that showed conformational changes in AAV8 (86)).

The experimental details for the SAXS and SANS experiments have been described in Chapter 2. One way of measuring the mass distribution of the VLPs would be to use the Radius of Gyration (R<sub>g</sub>) values of the particles in the sample as measure by small-angle scattering. The R<sub>g</sub> value can be determined by the following equation:

$$I(s) = I(o)e^{(-\frac{1}{3}R_g^2s^2)}$$

Where I is the measured intensity and s is the corresponding angular velocity. This equation is referred to as the guinier approximation and is valid for intensities at low s values. Both SAXS and SANS analysis of the capsid showed R<sub>g</sub> values of around 113

Å for the empty capsid VLPs at pH 7.5 (Table 3-1). These values were comparable to the  $R_g$  values reported for the parvovirus Kilham Rat Virus ( $\sim 104$  Å) in previous studies (127). At lower pHs this value showed a consistent, though small, decrease by  $\sim 3$  Å. This was confirmed independently in both SAXS and SANS experiments. The  $R_g$  values of GFP-coding DNA containing capsids showed a significant  $\sim 15$  Å decrease in  $R_g$  value. This indicated the mass contribution of the DNA contained inside the capsid that would affect the rotational state of the capsid and thereby the  $R_g$  value.

Previous cryo-EM studies have shown that conformational changes are induced in the capsid on complexing with cell surface primary receptor glycans(73). For this study, Neu5Ac  $\alpha$ -2,3 GalNAc  $\beta$ -1,4 GlcNAc was used as a receptor molecule for AAV1 (88). Neu5Ac  $\alpha$ -2,3 Gal  $\beta$ -1,4 GlcNAc was used as a receptor molecule for AAV5 and AAV8. Small-angle X-ray scattering analysis of receptor-complexed AAV1, AAV5 and AAV8 showed very small changes in  $R_g$  values that were within the experimental error (Table 3-2).

The pairwise density distribution function for empty AAV8 capsid VLPs (based on SANS data) at different pHs (Figure 3-3) shows that the minor density changes seen in the capsid occur in the interior of the capsid. There was a  $0.2$  electrons/Å<sup>3</sup> decrease in radial electron density between  $\sim 100$ - $150$  Å. There are also accompanying changes seen at radial distances closer to the surface of the capsid ( $>220$  Å). The regions on the surface show similar values and therefore do not differ much in their density distribution.

Contrast variation analysis of AAV8 capsids containing GFP-coding DNA was preceded by controls experiments with the empty capsid VLPs at 42% D<sub>2</sub>O concentration. The buffer subtracted scattering intensity values were largely negative

indicating a match between the intensity values of the VLP proteins and the buffer, confirming that the contrast variation process was working at 42% D<sub>2</sub>O concentration in the sample and the buffer. The negative intensity values seen are a result of overcompensation in D<sub>2</sub>O concentration. Buffer subtracted intensity values for the GFP-DNA containing capsids would correspond only to the DNA contained within the capsids.

SANS data was collected for AAV8 with GFP-coding DNA packaged at pHs 7.5 and 5.5. The pairwise distribution function for the GFP-coding DNA containing capsids showed a familiar 3 Å decrease in R<sub>g</sub> value from capsids at pH 7.5 ( $54.2 \pm 0.2$  Å) to 5.5 ( $51.1 \pm 0.2$  Å), just as seen in the case of the empty capsids (Figure 3-4). This would indicate that there is minor condensation in the arrangement of the DNA inside of the capsid in response to decrease in pH.

### **Discussion**

No significant residue level changes were observed in the crystal structures of AAV5 determined at the endosomal pHs (7.5, 6.0, 5.5, 4.0). Conformational changes seen in residues R392, E566 and Y707 for AAV8 (86) were not seen in corresponding residues R382, E552 and Y688 in AAV5.

This study hypothesized two structural changes in the AAV8 capsid in response to pH; 1) the externalization of the VP1u and 2) the reorganization of the encapsidated DNA. The small 3 Å decrease in the R<sub>g</sub> value of the AAV8 empty capsid VLPs with decrease in pH from 7.5 to 4.0 would not necessarily confirm the VP1u externalization process. However the corresponding pairwise density distribution function (Figure 3-3) did show changes internal to the capsid as well as on the surface. Accompanying changes were also seen at radial distances closer to the surface of the capsid. This

could be a process where the VP1u is undergoing structural changes in response to decrease in endosomal pH levels.

Using SANS analysis, a similar 3 Å decrease was seen in the GFP-coding DNA packaged in AAV8 with decrease in pH from 7.5 to 5.5. Differences were also observed in the pairwise distribution function from the data. This change would confirm that the DNA condenses in response to decrease in endosomal pHs to prepare the capsid for DNA release (Figure 3-4).

Previous studies on receptor-complexed AAV2 have shown small, residue level changes in the capsid by cryo-EM (73). Observing these changes is beyond the scope of the resolution and experimental error in the SAXS data in this study. The role of the receptor in inducing the process of externalization of the VP1u where pH alone is inadequate remains unconfirmed as no major changes were seen specific to receptor-complexing.

Unlike some RNA viruses (104), DNA inside the AAV capsid is not icosahedrally ordered and therefore is not seen in the crystal structures of the capsid. The crystal structures of AAV8 at different pHs however showed density for two nucleotides at pH 7.5 that was no longer ordered at lower pHs but was regained again at pH 7.5. This prompted the investigation of the potential structural rearrangement of the DNA inside of the capsid. This may be involved in the process of readying the DNA for ejection/release from the capsid or facilitating other structural changes in the capsid that prepare it for disassembly or trafficking to the nucleus.

We have shown by SAXS and SANS that there are changes in the structural organization of the DNA inside the AAV8 capsid in response to decrease in pH. Empty

capsid VLPs also show that the reorganization occurs on the interior of the AAV capsid with decrease in pH. This is in good agreement with structural changes seen on the capsid crystal structures that accompany these changes in the DNA. Taken as a whole, this data suggests that the genomic DNA inside the capsid condenses in preparation for release in synergy with structural changes in the capsid in response to pH change.

Table 3-1. Rg values (Å) of AAV8 obtained from SANS data. All Rg values are expressed in Angstrom units.

Rg (Å)	Buffer	SANS	SAXS
Empty Capsids	pH 7.5	113.2 ± 0.9	114.8 ± 0.4
	pH 6	112.8 ± 0.9	
	pH 5.5	112.9 ± 0.9	
	pH 4	110.8 ± 1.0	111.3 ± 1.3

Table 3-2. R<sub>g</sub> values (Å) of empty VLPs from SAXS data.

pH	AAV1	AAV5	AAV8
7.5	114.3 ± 0.1	109.7 ± 0.1	112.5 ± 0.1
6	113.4 ± 0.1	109.7 ± 0.1	111.1 ± 0.1
5.5	111.5 ± 0.1	110.9 ± 0.1	110.5 ± 0.1
4	111.2 ± 0.1	111.5 ± 0.1	109.1 ± 0.1

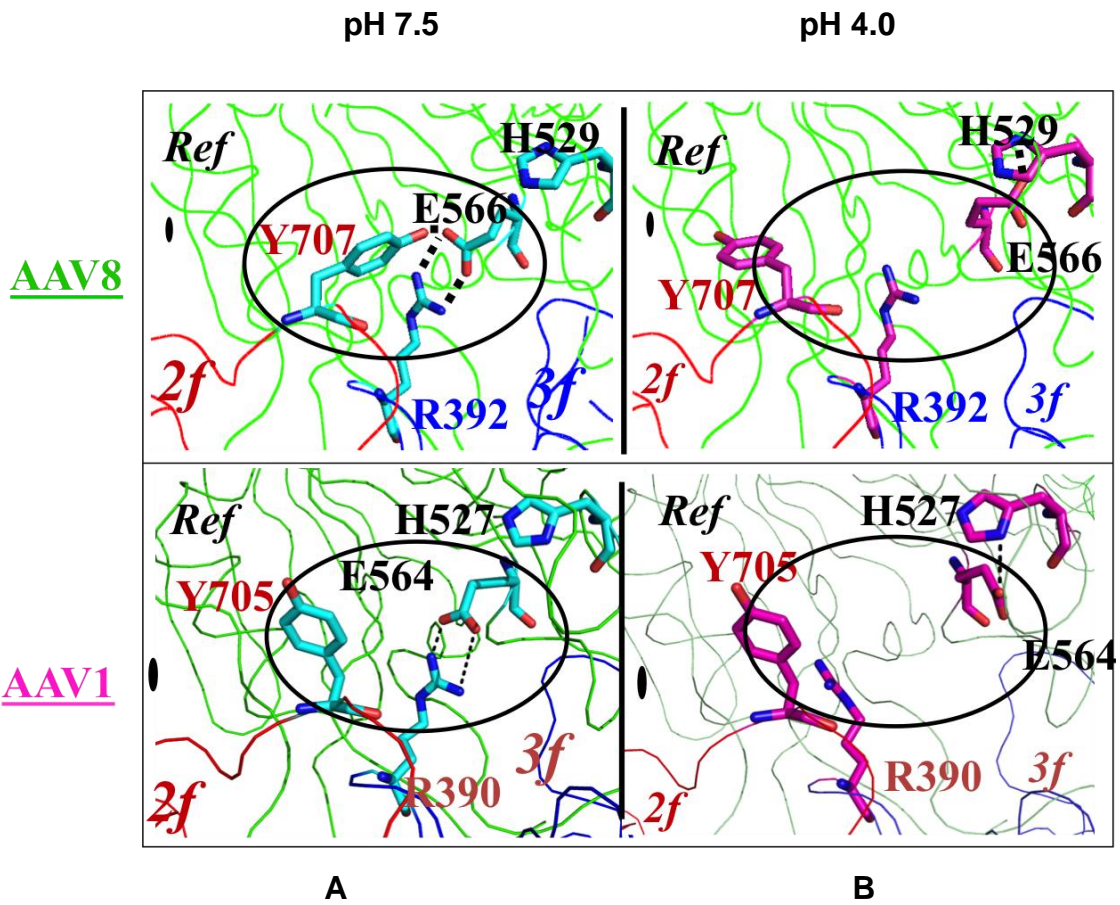


Figure 3-1. Conformational changes in pH quartet region with pH. The residues involved at shown in A) blue at pH 7.5 and in B) purple at pH 4.0 for AAV8 and AAV1.

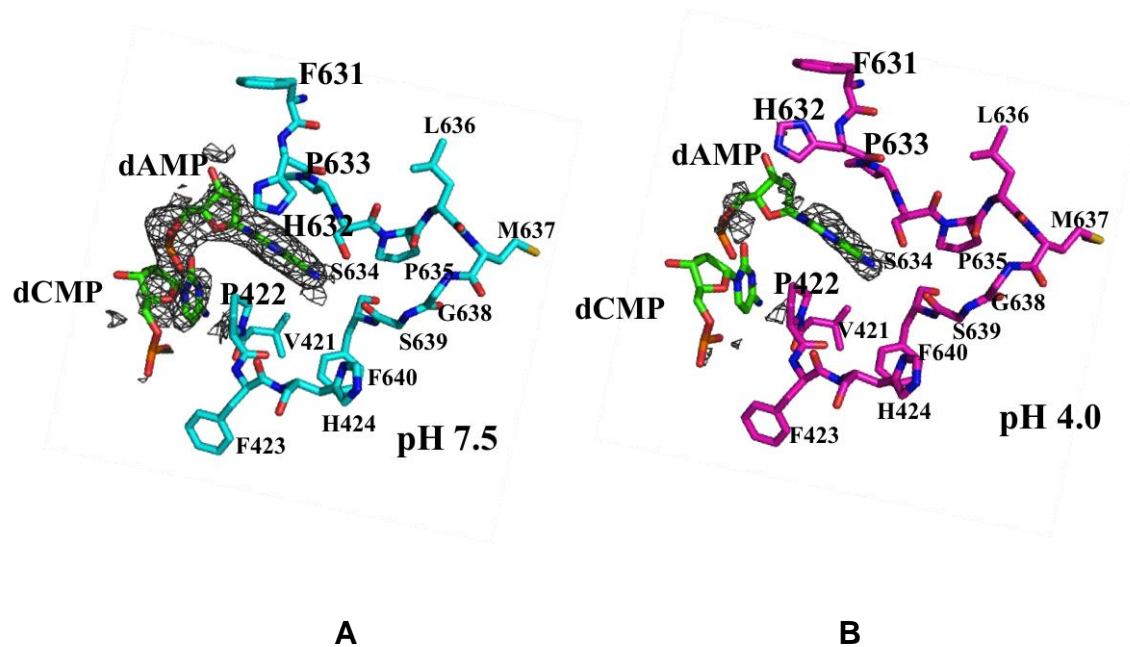


Figure 3-2. Changes in AAV8 DNA propensity at A) pH 7.5 (blue) and B) pH 4.0 (purple). The electron density seen for two nucleotides at pH 7.5 is no longer ordered at pH 4.0. H632 that shows association with the nucleotides at pH 7.5 changes conformation at pH 4.0.

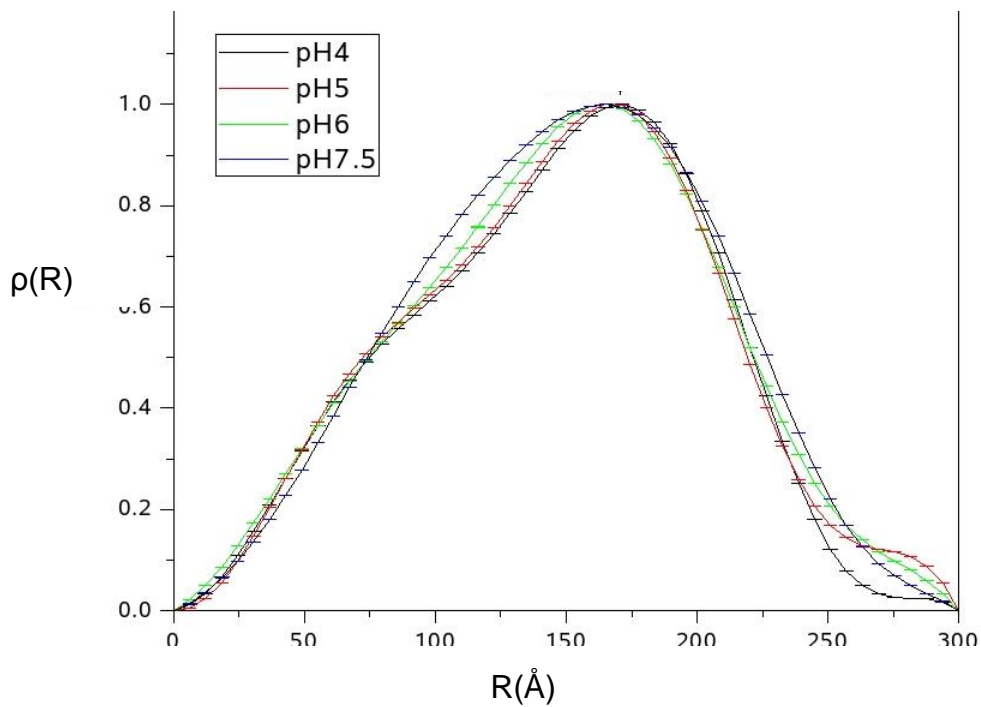


Figure 3-3. Pairwise density distribution function for AAV8 VLPs at different pHs. Through pH 7.5 (purple), 6.0 (green), 5.0 (red) and pH 4.0 (black), changes seen in the radial electron density are in the interior of the capsid.

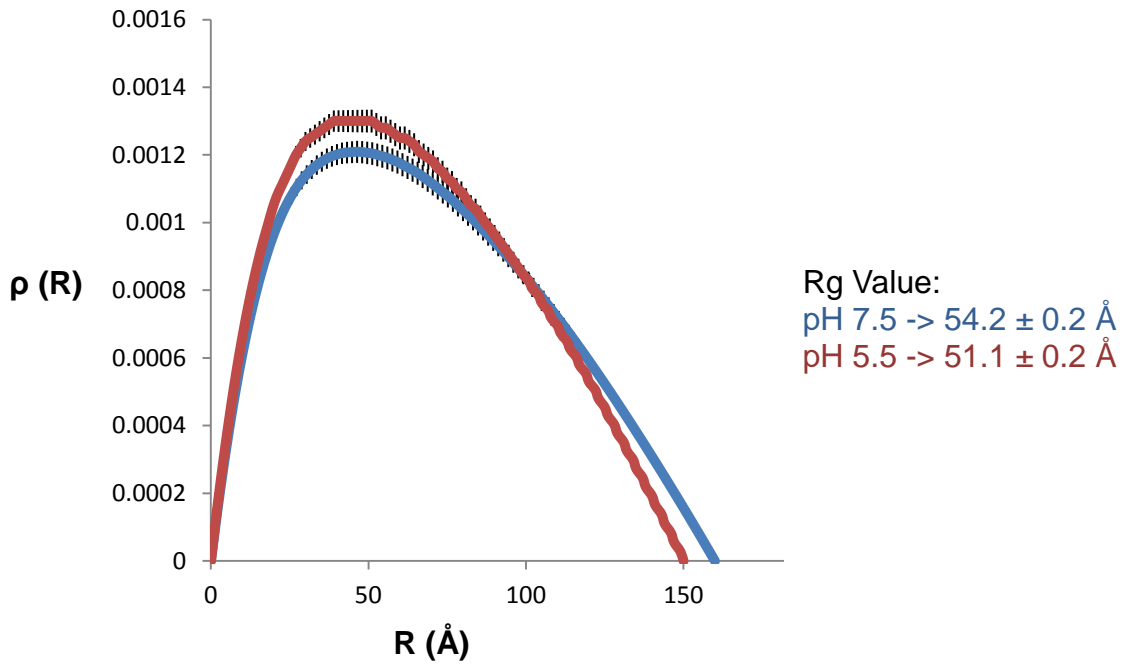


Figure 3-4. Pairwise distribution function of DNA containing AAV8 capsids. The DNA at pH 7.5 is represented in blue while the DNA at pH 5.5 is represented in crimson. A 3 Å change in the Rg value is seen between the two samples in response to pH.

## CHAPTER 4 STRUCTURAL AND BIOPHYSICAL ANALYSIS OF THE VP1-UNIQUE REGION

### **Background**

Structural changes occurring in the VP1u region are crucial to the process of infectivity in AAVs and related parvoviruses (53). However, as described in the introduction Chapter (Chapter 1), the biological mechanism that leads to these structural changes has not yet been identified and the exact nature of these structural changes was also not fully understood. This Chapter describes studies that attempt to identify these structural changes and also the causative factors in the endosome that may lead to such conformational changes.

The AAV VP1u contains a PLA<sub>2</sub> phospholipase domain and two nuclear localization signals, one of which is essential for nuclear entry during an infection. While the AAV PLA<sub>2</sub> does not have as much activity as other known PLA<sub>2</sub>s, mutational analysis have confirmed that altering the HDXXY active site motif causes a decrease in infectivity(113).

In this study, homology models of the capsid N-terminal regions were generated to compare to and interpret experimental results on the VP1u region. To identify the role of intrinsic disorder in the dynamics of the N-terminal regions the capsid monomer sequence of AAV1, AAV2, AAV5 and AAV8 was analyzed for intrinsic disorder in the capsid and the electrostatic state of different regions of the capsid monomers were calculated for AAVs 1-12. Circular Dichroism was used to demonstrate that the VP1/2 N-terminal region in AAV1 has a ordered  $\alpha$ -helical secondary structure. In-house algorithms were used to interpret the CD data and determine the secondary structural nature of the capsids. The  $\alpha$ -helical secondary structure was gradually lost with

decrease in pH from 7.5 to 4 and was regained when the pH was increased back to 7.5, demonstrating a reversible mechanism. This study would be an important step in physically documenting conformational changes in the VP1u region and establishing the order of events in the escape of the capsid from the endosome.

## Results

ROBETTA server (65) models (Figure 4-1) of the first 209 amino acids of the AAV1 VP1 sequence (not seen in the crystal structure) showed a consensus  $\alpha$ -helix motif connected by loop regions. The VP1/2 common region did not show any helices and instead was indicated to comprise of coiled secondary structure. Superimposition of two of these models on a crystal structure of bovine pancreatic phospholipase A<sub>2</sub> (PDB ID: 1BP2) (Resolution: 1.7Å) showed that the helices containing the active site and the calcium-binding site showed a high degree of conservation in structure (28). The RMSDs of these superimpositions were 3.3 Å and 2.8 Å respectively. Based on the Critical Assessment of Techniques for Protein Structure Prediction (CASP) assessment of ROBETTA predicted models (23), these values were quite reasonable. The PLA<sub>2</sub> active site (residues H48, Y52, Y73 and D99 on the bovine pancreatic PLA<sub>2</sub> sequence) was contained within the two superimposed  $\alpha$ -helices (Figure 4-1). The PLA<sub>2</sub> calcium-binding site (residues Y28, G30, G32 and D49 on the bovine pancreatic PLA<sub>2</sub> sequence) was also structurally conserved in the VP1u models superimposed on the structure with D49 located on one of the  $\alpha$ -helices while the other three residues were located on the adjacent two-strand  $\beta$ -sheet (Figure 4-1). These models were also superimposed onto the crystal structure of the AAV1 (PDB ID: 3NG9, Resolution: 2.5 Å) with residue 218 (the first residue seen on the AAV1 crystal structure monomer) overlapping between the VP1 N-terminal model and the crystal structure. When the

VP1u was oriented directly beneath the 2-fold interface (based on previous cryo-EM data from Kronenberg *et al.*) (69), the VP1/2 common loop region was in a position primed to deliver the VP1u through the 5-fold pore (Figure 4-2).

The intrinsic disorder propensity for the AAV VP1 sequence was calculated using PONDR-Fit (132) described in Chapter 2. A plot of the predicted intrinsic disorder disposition versus the capsid protein residue number is shown in Figure 4-3. The PONDR-Fit algorithm showed an intrinsic disorder stretch in the VP1/2 common region (residues ~ 140-202). The intrinsic disorder region continued into the VP3 sequence to ~ residue 220. This is in good agreement with the lack of ordered density for the first 10-15 residues of VP3 in all the solved crystal structures for the AAVs to date. It was also seen that the capsid variable regions (VRs) also demonstrate variability in intrinsic disorder as well while the structurally conserved regions show a consensus low intrinsic disorder disposition.

A detailed description of the pI value calculations is given in Chapter 2. A histogram based on the calculated pI values for the VPs of AAVs 1-12 is given in Figure 4-4. The VP3 and the intact empty capsids show an average pI value of ~ 6.3 through all the AAVs (1-12) because of VP3 dominance in copy number (1:1:10 – VP1:VP2:VP3). The addition of genomic DNA (pI ~ 5.0) to the capsid would effectively decrease the pI by ~ 0.4 to an average pI value of ~ 5.9. Interestingly, the VP1u exhibits a consistent acidic pI of ~ 4.9 while the VP1/2 common region has a more basic pI value of ~ 7.3. There is a greater variability in the pI value of the VP1/2 common region however with pI values ranging from 5 – 10.

## **Ordered Structural State of the VP1u**

Intact empty particles of AAV1 (purification described in Chapter 2) were used in the CD experiments. The CD spectrum of AAV1 at pH 7.5 and 25° C, when deconvoluted (by algorithm described in Chapter 2), showed an ordered  $\alpha$ -helical secondary structure (Figure 4-5). Of the 518 residues seen in the crystal structure, only a short (10 amino acids) conserved  $\alpha$ -helix is observed, that contributes less than 1% of the total secondary structure of the capsid monomer whereas deconvolution of the AAV1 CD spectrum (details described in Chapter 2) showed a 30-40%  $\alpha$ -helical signal. Therefore, this  $\alpha$ -helical component of the capsid must come from the part of the capsid protein that is not observed in the crystal structure, the VP1/2 N-terminal region. It is interesting to note that this effect is seen despite the fact that the VP1 and VP2 together form only ~ 16% of the total amino acid composition of the capsid based on copy number (1:1:10 – VP1:VP2:VP3) and amino acid content. When compared with a VP1 deletion construct of AAV6 (Figure 4-5), which differs from AAV1 at only 6 residues (only one of which is in the VP1u region) it can be confirmed that the  $\alpha$ -helical signal is indeed from the VP1u region. The AAV6 VP1 deletion construct showed a lower  $\alpha$ -helical propensity as observed in the crystal structure (88). It also suggests that the VP1/2 common region does not have an  $\alpha$ -helical propensity, which is in agreement with the intrinsic disorder disposition of the domain and the homology models (Figure 4-1).

## **Loss of $\alpha$ -helicity with Increase in Temperature**

CD was used to experimentally probe structural changes in the VP1u. Electron micrographs were used to ensure that the structural changes observed were not a result of capsid disassembly or breakage. A detailed description of the methodology involved

is provided in Chapter 2. Molar ellipticity values were used to generate normalized and scaled CD spectra that could be compared across experiments.

As the temperature was increased from 25° C to 90° C, the CD spectra for AAV1 (between the wavelengths of 200 and 260 nm) showed a loss of secondary structure at ~ 70° C (Figure 4-6) while electron micrographs showed that the capsids were still intact (Figure 4-7). This would suggest that the changes seen in the CD signal were primarily a local denaturation event of the VPs rather than whole-capsid degradation.

### **Loss of $\alpha$ -helicity with Decrease in pH**

When the ellipticity values at 208 nm for AAV1 at different pHs (7.5, 6, 5.5 and 4) were plotted against temperature (Figure 4-8) it was clear that the transition temperature decreased with decrease in pH. In other words, this indicates that a decrease in pH may serve as a mechanism to destabilize the capsid or make it more flexible. CD experiments at the different pHs (at physiological temperature) of AAV1 capsids showed spectra that would imply different secondary structural characteristics (Figure 4-9) (at pH 6, the AAV1 CD spectrum showed a decrease in the degree of  $\alpha$ -helicity by ~ 10% when compared to the spectrum at pH 7.5). This trend continued at pHs 5.5 and 4 where almost no  $\alpha$ -helical signals (<10% as determined by the in-house deconvolution algorithm) were detectable (Table 4-2). In spite of this, electron microscopy images of the capsids at these different pHs showed that the capsids were not losing their structural integrity in the process. Previous studies on AAV2 have shown that heating the capsid to a temperature of ~ 65° C results in the irreversible externalization of the VP1u region(111). The unfolding of the VP1u region could have a role in the externalization process, as similar losses of  $\alpha$ -helical signal are seen at high temperature (~ 70° C) (Figure 4-6) and low pH (5.5 and below). This unfolding was

found to be irreversible; decreasing the temperature to 25° C did not restore the secondary structural state signal. This data would suggest that the loss of signal might be the unfolding of the secondary structure of the VP1 N-terminal region alone.

### **Restoration of Secondary Structure**

To see if this conformational change was reversible, AAV1 capsid samples were treated at pH 4.0 and then were buffer exchanged back to pH 7.5. Using CD experiments it was observed that the  $\alpha$ -helical signal was restored (Figure 4-9). Electron micrographs were used to confirm that these capsids were also still intact. This suggests that the structural transitions that occur with a decrease in pH from 7.5 to 4.0 were reversible and increasing the pH again to 7.5 at least partially restores the  $\alpha$ -helical conformation of the VP1u region.

### **AAV5 and AAV8**

The CD spectrum of empty AAV8 VLPs at 25° C and pH 7.5 showed a similar  $\alpha$ -helical propensity (~30-40%) to AAV1 as would be expected (Figure 4-10). This  $\alpha$ -helical propensity was absent (<10%) (Table 4-2) at the lower pHs (6.0, 5.5 and 4.0). Unlike a gradual unfolding in the VP1u secondary structure as seen for AAV1, a much more rapid unfolding process was observed for AAV8 with decrease in pH.

The CD spectrum of AAV5 at 25° C and pH 7.5 was more similar to the AAV6  $\Delta$ VP1u construct under the same conditions (Figure 4-11A). SDS-PAGE analysis of the AAV5 baculoviral constructs showed little or no VP1 presence (Figure 4-11B). This would explain the absence of an  $\alpha$ -helical signal for the AAV5 capsids. While the reason for the lack of VP1 packaging in AAV5 capsids is not known, it verifies that the  $\alpha$ -helical signal seen for AAV1 and AAV8 is most likely do to the VP1u secondary structural elements.

## Discussion

The complete reason for the absence of electron density for the VP1/2 N-terminal region in crystal structure of the AAV1 capsid is still unknown. It could be a result of heterogeneity in the presence of VP1 and VP2 in capsids where icosahedral averaging may have lead to disordered features that are attributed to them. However these CD studies show that there is a detectable ordered secondary structure of the VP1/2 N-terminal region. Previous studies have shown phospholipase A<sub>2</sub> protein structures from snake (124) and bee venom (107) to be primarily  $\alpha$ -helical. Since the VP1u (residues 1-137) also contains a PLA<sub>2</sub> domain, it is not surprising that a similar  $\alpha$ -helical propensity is seen for it, from predicted models and from the CD data. There have been previous CD studies on a related parvovirus MVM and the CD spectrum was similar to the ones seen for the AAVs but the spectrum was not deconvoluted (18).

The VP1/2 common region (residues 138-202) in the predicted models does not exhibit helical or  $\beta$ -strand secondary structural elements. When the sequence of VP1 from AAV1, AAV2, AAV5 and AAV8 were analyzed for potential disordered or unstructured regions using the PONDR-Fit algorithm(132), it was observed that the VP1/2 common region and the first ~ 20 results of VP3 were predicted to be highly disordered in comparison to other regions of the capsid. This observation may be another reason for why some of the N-terminal region of VP1 (first ~220 residues), VP2 (first ~60 residues) and VP3 (first ~20 residues) are not ordered in the crystal structure besides just being artifacts of averaging.

Previous studies have observed that the VP1u region is exposed when the capsid is subjected to high temperatures (~ 65° C) at physiological pH (111). While high temperature may not be the biological cause for VP1u exposure during the infective

pathway of the virus, it can be inferred from this study that decrease in endosomal pH results in similar structural changes in the VP1u as seen from increase in temperature; both involve the unfolding of the VP1u region. This may explain how high temperatures are able to induce exposure of the VP1u; by first inducing the unfolding the VP1u region and then the externalization.

This study shows that even though decrease in pH (to 4.0) has not been shown to induce exposure of VP1u (111), there is a definite pH-induced structural change that takes place in the capsid.

The loss of secondary structure with decrease in pH can complicate the question of VP1u externalization during the process of endosomal trafficking of the AAV capsid. The actual biological cause for the exposure of VP1u remains to be identified but change in  $\alpha$ -helicity may have a role in the process of exposure of VP1u. If so, then it may be true that pH would be an important factor in the mechanism of VP1u exposure even though it is not entirely induced by decrease in pH alone. It is possible that including certain other factors may help induce the exposure of VP1u *in vitro*.

An analysis of the calculated isoelectric point (pI) values of different capsid regions for AAV serotypes 1-12 showed that the VP1u has an acidic character with the pI values for all the AAVs of  $\sim 4.8$ . The VP1/2 common region showed more variety with value ranges from 5 to 10 across the 12 serotypes, but the mean value ( $\sim 7.3$ ) was more basic than the VP3 sequence. The VP3 (pI =  $\sim 6.3$ ) is the dominant capsid protein and therefore influenced the pI of the capsids the most. The mean pI for the net capsid across the 12 AAV serotypes was  $\sim 6.3$ .

The accepted pI value for DNA (nucleotides) from literature is ~ 5.0 (61). The VP1u, therefore, is more acidic in nature and this could complicate the picture of both the genomic DNA and the VP1u co-existing in the interior of the capsid. It is possible that charge-charge repulsion between the VP1u and the DNA may help it get oriented in a specific manner to prepare it for release from the capsid. The VP3 and net capsid pI values would indicate that the VP3 sequence and the capsid would have a zwitterionic state at early to late endosomal pHs (~ 5.5 – 6.5) but the VP1u would still be charged. This may be a possible explanation for how the VP1u exhibits specific structural changes in the endosome while the rest of the capsid does not. These differences in pI may also be important in determining the copy numbers of individual capsid monomers in assembling the whole capsid. While steric hindrance may have a role in the localization of VP1 monomer on the capsid (for example, steric clashes would not allow for adjacent monomers on the 5-fold to be VP1), it is possible that the charged state of the different capsid regions determines the distribution and copy number of the specific monomer (VP1, VP2 or VP3) in the capsid.

Since the VP1u is actually ordered in solution while located inside the capsid, it becomes more difficult to visualize the process of externalization while the capsid stays intact. It is possible that the unfolding of the VP1u with pH aids in this mechanism. A study by Levy *et al.* on AAV2 has identified structural changes at the 5-fold pore in the presence of a cell-surface glycan receptor (heparin sulfate) (73). The 5-fold pore seems to open in an iris-like rotation of the ring of residues leading to the widening of the top of the 5-fold channel in the process and this may be in synergy with the unfolding of the VP1u. The unfolded VP1u may easily slide out the expanded 5-fold pore. The

potentially unstructured nature of the VP1/2 common region may have a role in this. The flexibility imparted by the intrinsic disorder in the VP1/2 common region would be useful in permitting large motion of the VP1u to the 5-fold pore. Since this unfolding process has been shown to be reversible (Figure 4-9), the VP1u could adopt its native structure when externalized, possibly when in contact with the endosomal membrane (Figure 4-12).

This study shows that the VP1u in AAV1 was structurally ordered in an  $\alpha$ -helical conformation inside the capsid. This secondary structural state was affected by decrease in pH from 7.5 to 4.0 and negligible secondary structural elements were seen at the lower pH. Increasing the pH again to 7.5 restored the  $\alpha$ -helical conformation in the VP1u. The VP1/2 common region has an intrinsically disordered nature that could impart the flexibility required to permit the externalization of the VP1u through the 5-fold pore. Differences in the charged state of the VP1u and the rest of the capsid may service to delay the process of externalization until a late endosomal pH (~ 6.0) is achieved. This study provides major insights into the potential mechanism of capsid rearrangements in preparation for endosomal escape of the AAV capsid.

Table 4-1. Thermal VP1u structural transition temperatures (in ° C) for AAV1, AAV5 and AAV8\*. The numbers in parenthesis are the errors associated with the values based on triplicate experiments.

AAV serotype	pH			
	7.5	6	5.5	4
1	72 (3)	63 (2)	ID	ID
5	84 (2)	75 (2)	75 (3)	75 (2)
8	72 (3)	ID	ID	ID

\*ID – Indeterminate due to very low signal intensity

Table 4-2. Percentage  $\alpha$ -helicity from deconvolution of CD spectra of AAV1, AAV5 and AAV8 at different pHs.

Serotype	AAV1	AAV5	AAV8
pH 7.5	35-45%	5-15%	35-45%
pH 6.0	25-35%	5-15%	<10%
pH 5.5	<10%	5-15%	<10%
pH 4.0	<10%	5-15%	<10%

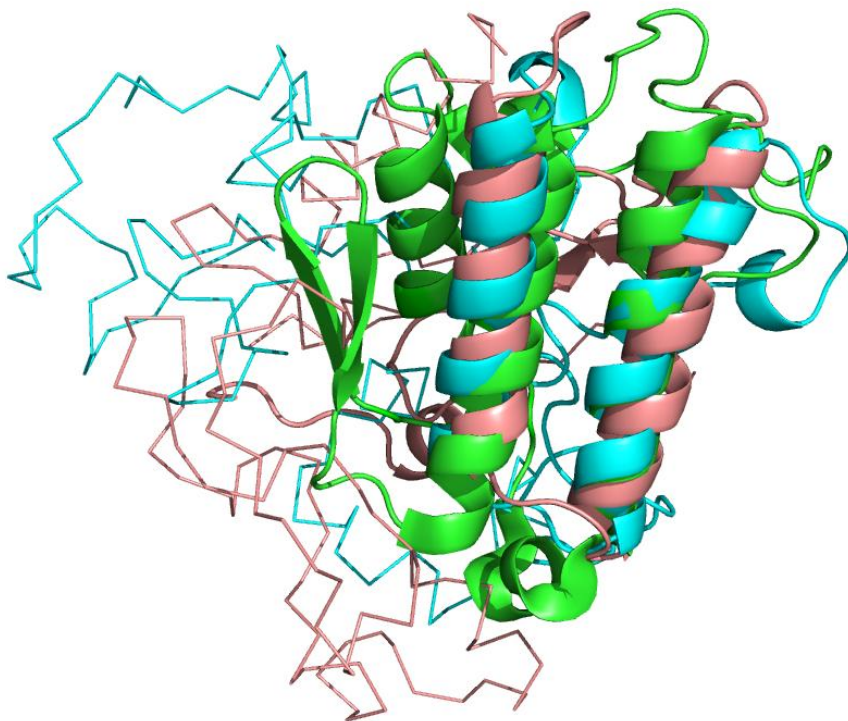


Figure 4-1. Cartoon rendition of superimposition of VP1u models on PLA<sub>2</sub> crystal structure. Two of the VP1u models (cyan and pink) were structurally superimposed on Bovine Pancreatic PLA<sub>2</sub> (green) (PDB ID: 1BP2). The superimposition RMSD values were 3.3 Å and 2.8 Å respectively. The  $\alpha$ -helical active site is well conserved in the models. This image was generated using PyMOL.

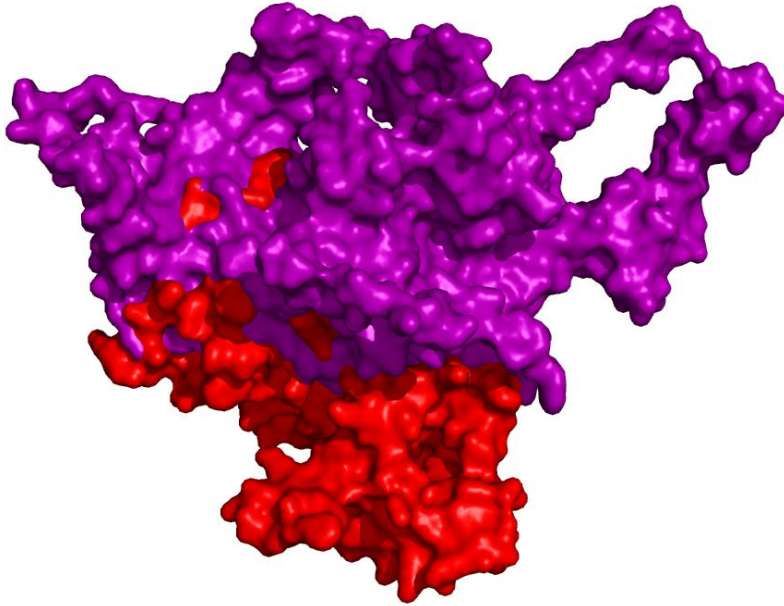


Figure 4-2. Surface rendition of superimposition of VP1u on to the capsid monomer from the crystal structure. The VP1u monomer (red) was structurally superimposed on to overlapping regions (residues 218-255) of the VP3 capsid monomer (purple) from the AAV1 crystal structure (PDB ID: 3NG9). This image were generated using UCSF-CHIMERA (97).

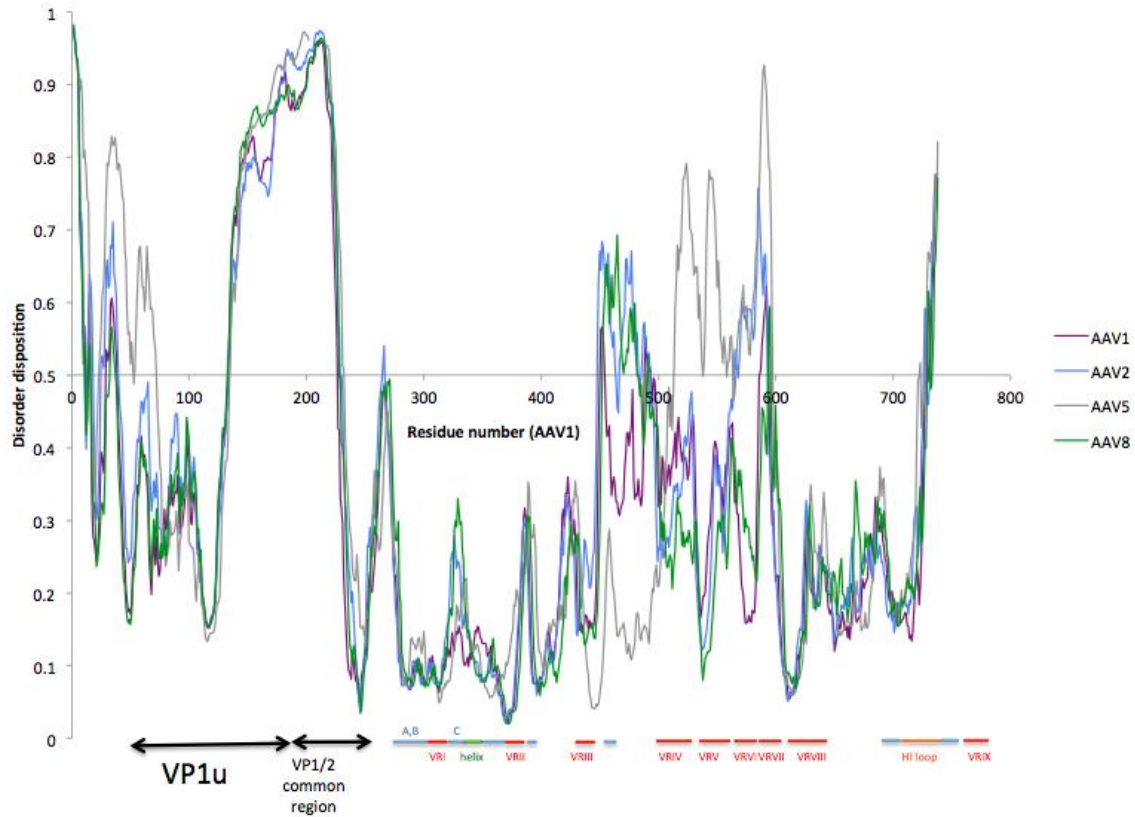


Figure 4-3. PONDR-FIT plot showing intrinsic disorder in VP1/2 common region. Variable regions are marked in red while highly conserved regions of the capsid are in blue, green and orange in the basal markings. AAV1 (purple), AAV2 (blue), AAV5 (gray) and AAV8 (green) show similar disorder propensities with the exception of the variable regions

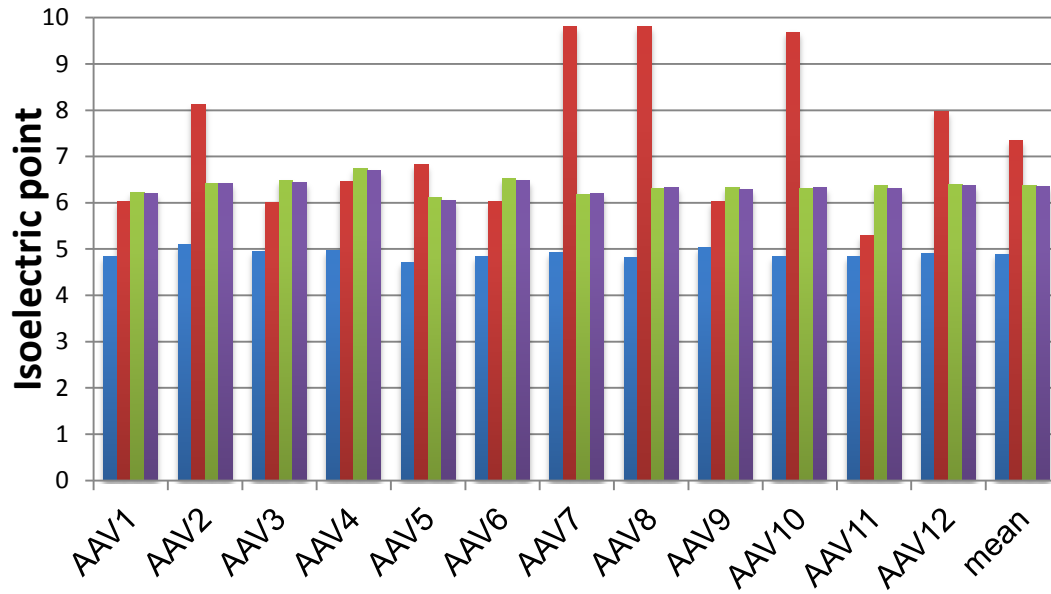


Figure 4-4. Histogram showing pI values across all 12 AAV serotypes. The VP1u (blue) pI values are 1 unit lower than the average pI values of VP3 (green) and the whole capsid (purple). The VP1/2 common region (red) shows a variable basic pI through the serotypes.

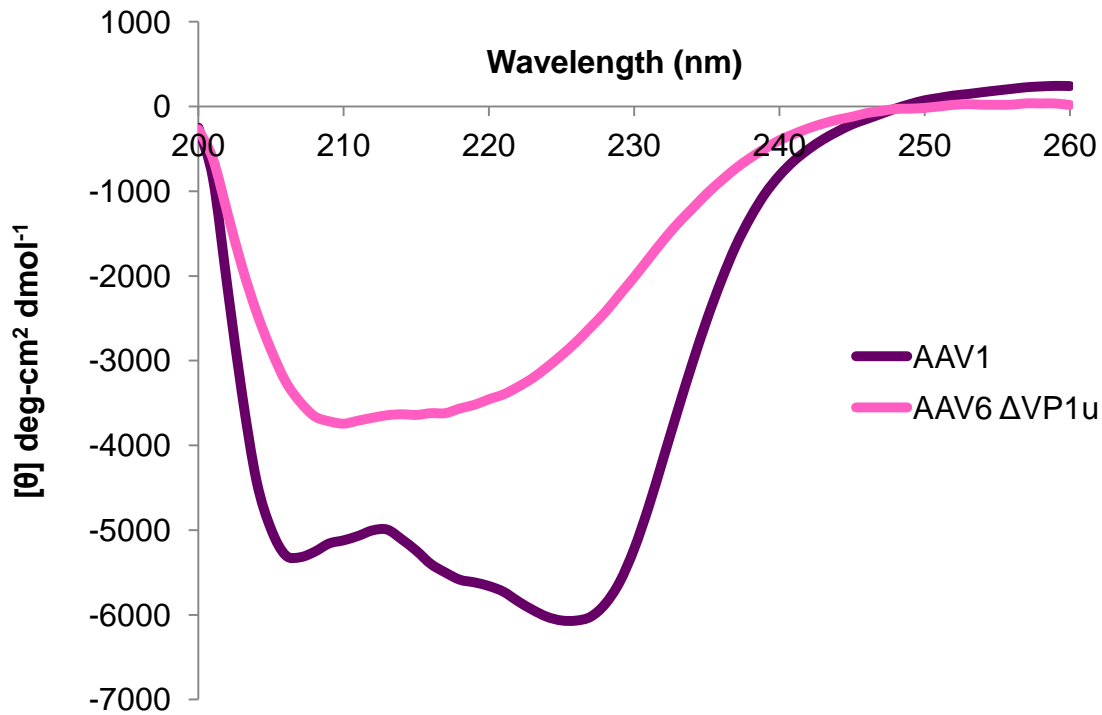


Figure 4-5. CD spectrum of AAV VP1u. AAV1 empty capsid VLPs (purple) show  $\alpha$ -helical propensity while AAV6  $\Delta$ VP1 constructs (pink) show lack of  $\alpha$ -helical propensity confirming that the VP1u is structurally ordered in solution and is  $\alpha$ -helical.

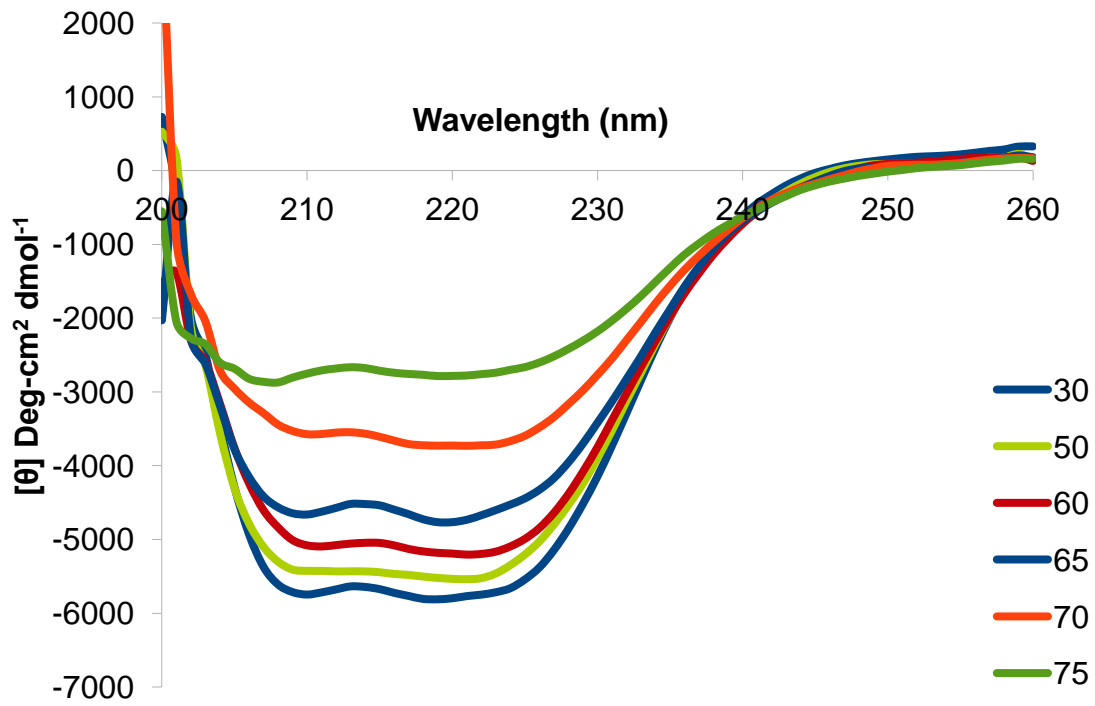


Figure 4-6. CD spectrum of AAV1 empty capsid VLPs at different temperatures. Through temperatures 30° C (blue), 50° C (green), 60° C (red), 65° C (orange), 70° C (brown) and 75° C (black) the VP1u signal is lost with increasing temperature.

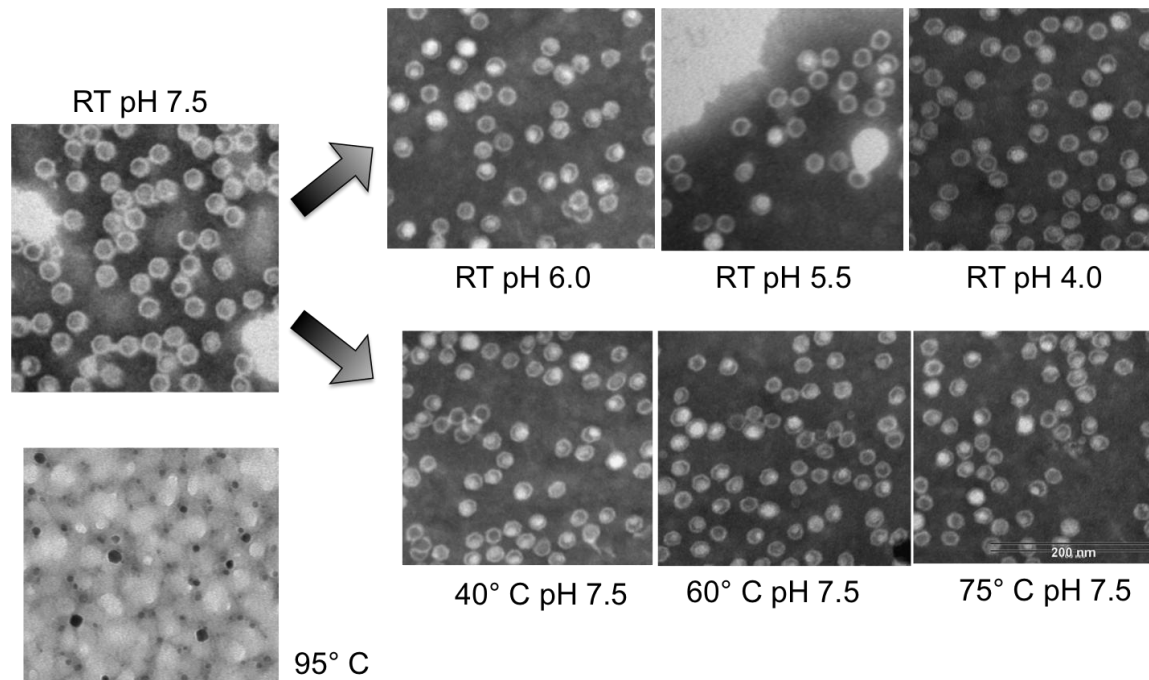


Figure 4-7. Electron micrographs of the AAV1 capsid VLPs. At different temperatures and different pHs, the capsids are still intact. Only on heating to 95° C, the capsids showed complete denaturation

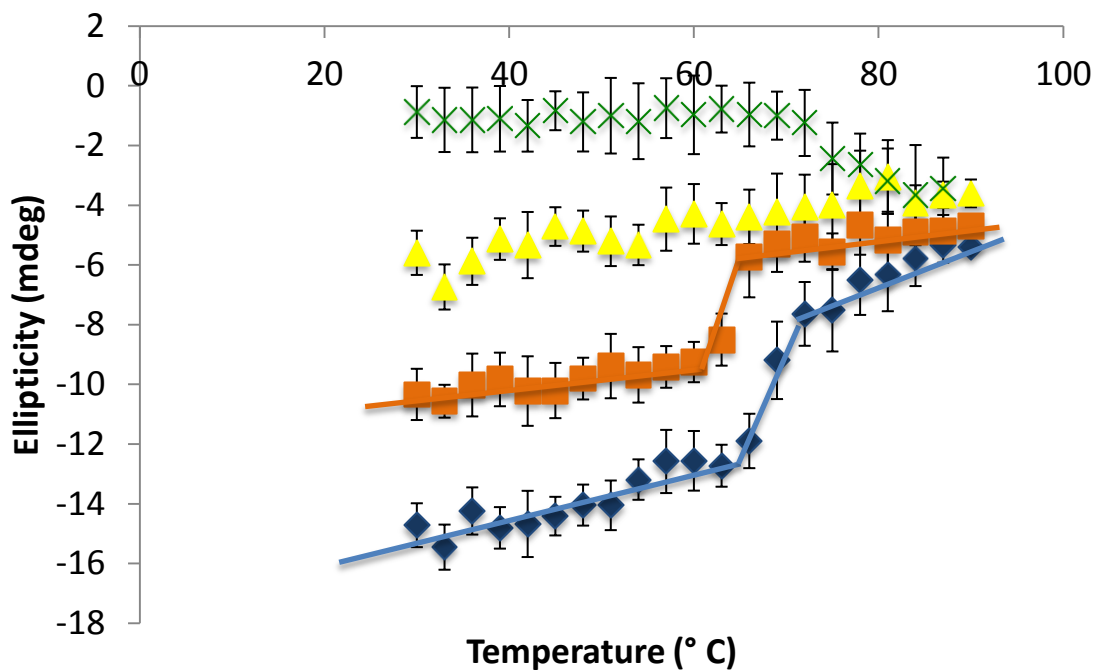


Figure 4-8. Plot of ellipticity values at 212 nm Vs temperature from CD experiments. At different pHs 7.5 (blue), 6.0 (orange), 5.5 (yellow) and 4.0 (green) the ellipticity values decrease with decreasing pH and show transitions at  $\sim 70^{\circ}\text{C}$  at the higher pHs

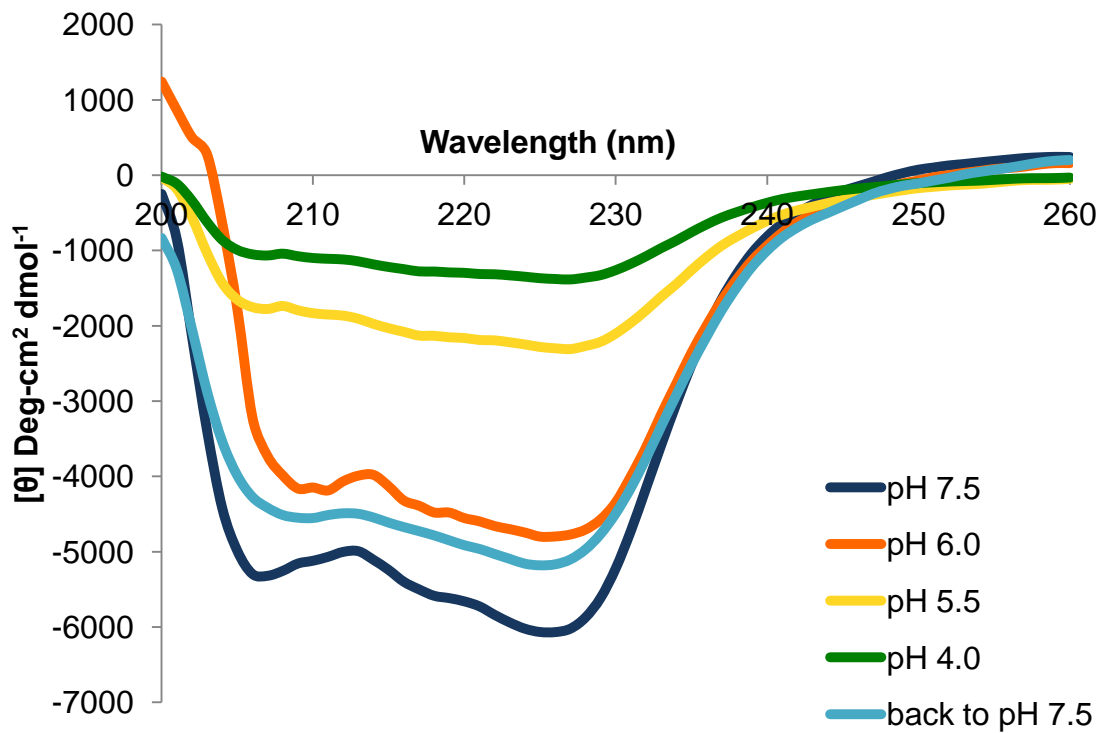


Figure 4-9. CD spectrum of AAV1 empty capsid VLPs at different pHs. At pHs 7.5 (navy blue), 6.0 (orange), 5.5 (yellow) and 4.0 (green) the AAV1 capsid VLPs show loss of secondary structural signal with decreasing pH. This signal is restored at least in part when the pH is restored to 7.5 (light blue)

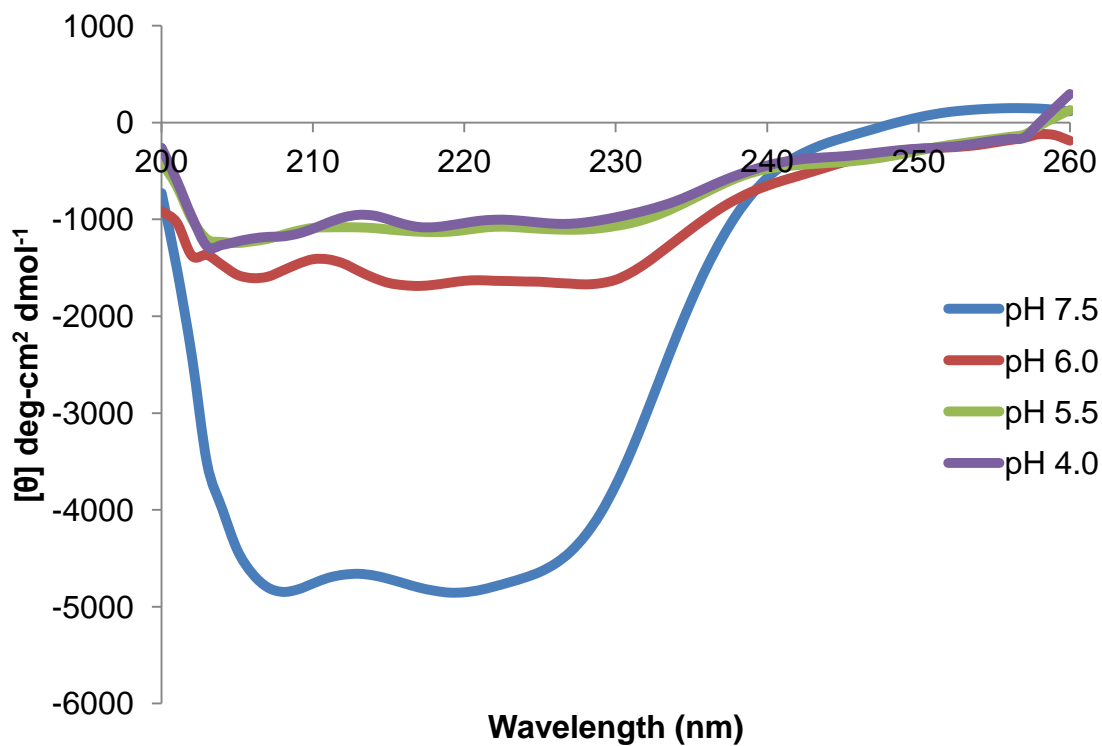


Figure 4-10. CD spectrum of empty AAV8 capsids at different pHs. The  $\alpha$ -helical signal seen at pH 7.5 (blue) is no longer seen at the lower pHs 6.0 (red), 5.5 (green) and 4.0 (purple).

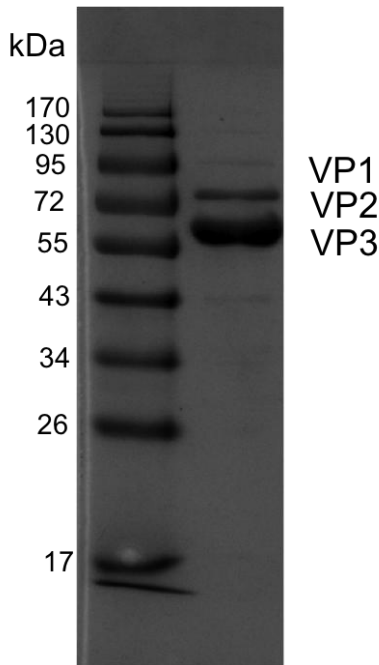
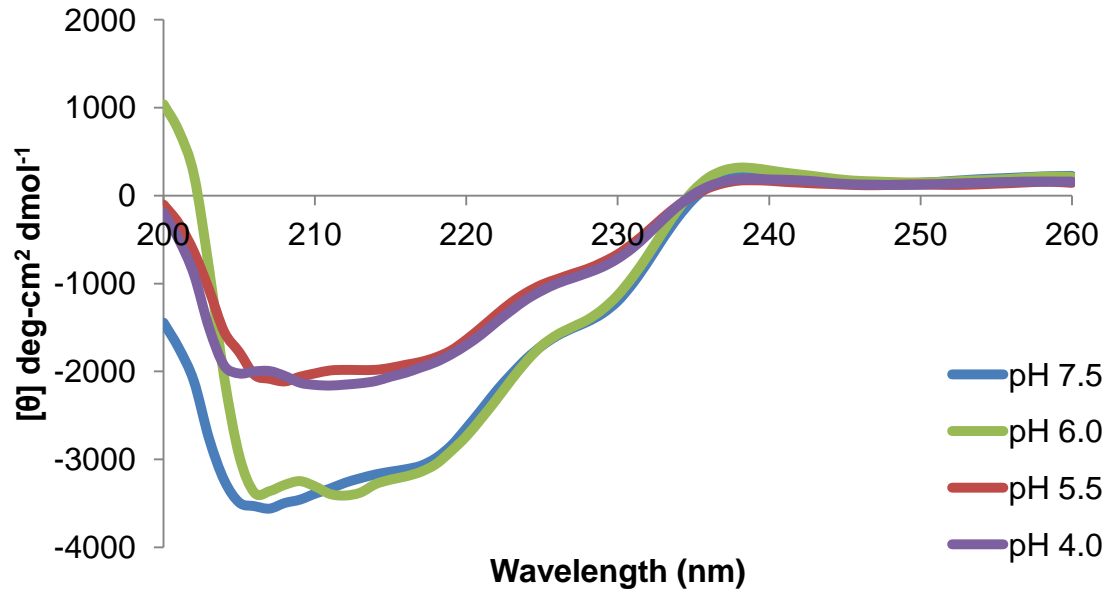


Figure 4-11. CD spectrum of empty AAV5 capsids at different pHs. A) A distinct  $\alpha$ -helical signal is not seen at any pH but there is a single transition from pHs 7.5 (blue) and pH 6.0 (green) to pH 5.5 (red) and pH 4.0 (purple). B) SDS-PAGE gel showing lack of VP1 presence in AAV5 capsids.

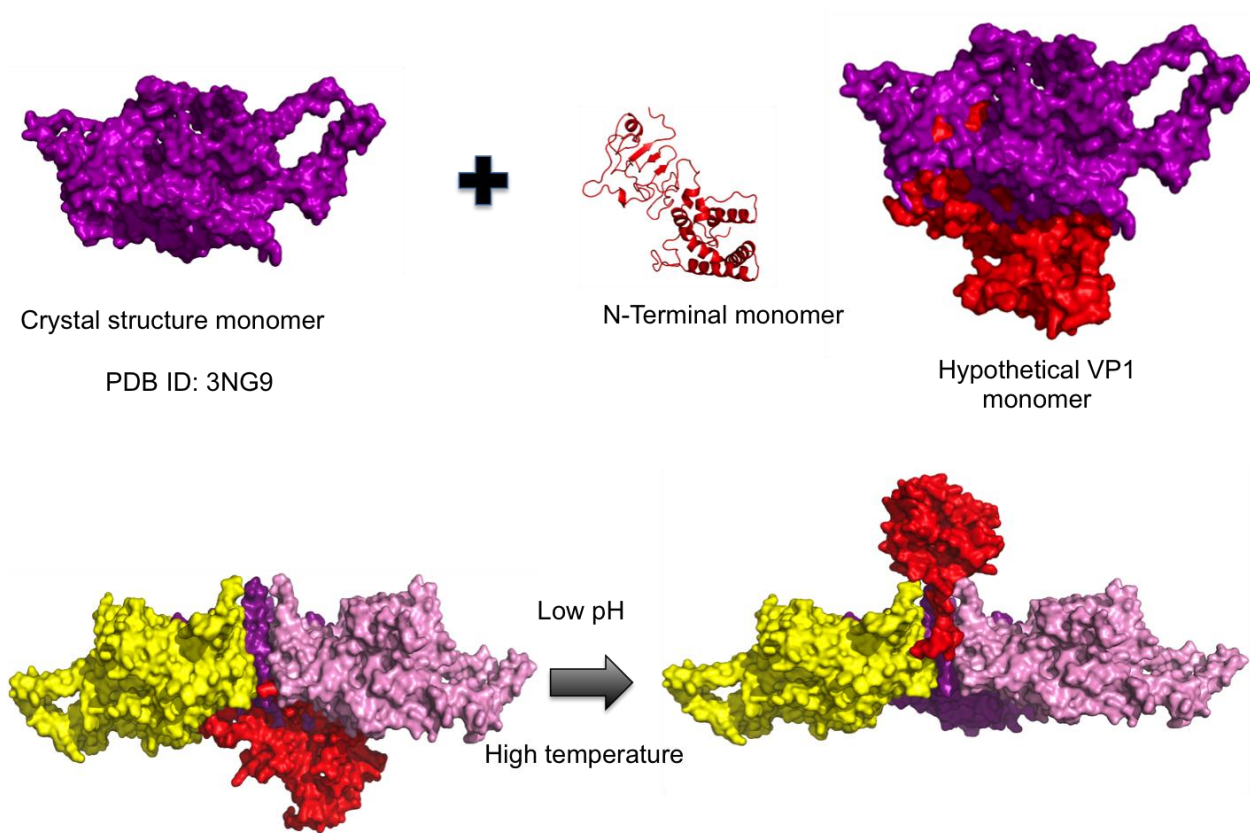


Figure 4-12. AAV1 VP1u externalization model. The VP1u (red) when structurally superimposed on to the AAV1 VP3 crystal structure (1NG9) monomer, appears directly beneath the 5-fold and 2-fold interface. When the VP1u is unfolded with decrease in pH it can be threaded out through the 5-fold pore and when the right conditions are available on the outside of the capsid, it can refold back to a native functional state. The images were generated using PyMOL.

## CHAPTER 5 THE ROLE OF STRUCTURAL STABILITY IN THE INFECTIVE PATHWAY OF ADENO-ASSOCIATED VIRUSES

### **Background**

While structural changes in the AAV capsid associated with endosomal trafficking have been identified, the structure of the capsid when it arrives to the nucleus is still not known. The capsid would either have to eject the DNA inside the nucleus or disassemble to expose the DNA prior to replication. Endosomal cathepsins B and L have been identified as uncoating factors for AAV2 and AAV8 (1). However, the stability of the capsid structure would also have an important role in the capsid disassembly process.

Previous studies have determined the crystal structure of AAV8 at different pHs (7.5, 6.0, 5.5 and 4.0) (86). The PDBe PISA tool (68) and VIPERdb (19) were used to calculate the buried surface area and association energies at the capsid symmetry interfaces (86). Based on this analysis, the 2-fold interface was shown to decrease in buried surface area and association energy with decrease in pH (Table 5-1). This may be part of the structural changes seen in the capsid with response to pH but it is also possible that an embrittlement of the capsid is occurring. It is also possible that structural changes are occurring in the capsid in response to decrease in pH that allow for better flexibility in the capsid (which would serve to help in the process of VP1u externalization) or promote capsid disassembly.

It is therefore important to assess the stability of the capsid in response to pH. This can be done in a number of different ways. Here, thermal stability was chosen, as changes in the thermal denaturation temperature of the capsid would be a good gauge of the structural stability of the viral capsid at different pH conditions.

Previous thermal denaturation studies on related viruses have shown melting temperatures at ~ 70-85° C using DSC and fluorescence experiments (3, 18, 100). For a related parvovirus, MVM, thermal denaturation temperatures were determined to be at ~ 77° C (18) with thermal inactivation of infectivity at ~ 70° C (100). It was also observed that in presence of 1.5 M Guanidium-HCl, the thermal denaturation temperature decreased to ~ 62° C (18) indicating that the structure of the capsid had a role in determining capsid stability. CD experiments on MVM showed no change in the CD spectrum between 200 and 250 nm wavelength even at temperatures as high as 95° C (18). This was concluded as the stabilization of a denatured conformation of the MVM capsid (18).

Since loss of secondary structural state was observed using CD in the VP1u in response to increase in temperature (Chapter 4, Figure 4-8), it was important to verify if this loss is not a result of capsid denaturation. Thermal denaturation studies would be a good way of determining if multiple steps are involved in capsid disassembly. This study uses DSC and EM to analyze the thermal stability of the capsid. The methodology involved is described in detail in Chapter 2.

## **Results**

The Origin program suite (OriginLab, Northampton, Massachusetts) was used to visualize, set baselines and measure melting temperatures. The data from the DSC experiments was plotted on a graph with Temperature on the X-axis and enthalpy value on Y-axis (Figure 5-1). AAV1 and AAV5 showed a single transition point (Figure 5-1) at the thermal melting temperature ( $T_m$ ) for the AAV capsids as opposed to multiple transition points that would correspond to several “step” events in the disassembly process of the virus (for example, from capsids to pentamers to monomers to unfolded

monomers). Single point transitions have been observed in previous studies on a related virus MVM (18) and therefore it was not surprising to observe the same in the case of AAV1 and AAV8.

Thermal denaturation temperatures measured by DSC were interesting, in that they were different from the conformational transition temperatures seen from the CD experiments (Chapter 4: Table 4-1, Table 5-2). For example, the conformational transition temperature for AAV1 at pH 7.5 was  $\sim 70^\circ\text{C}$  while the denaturation temperature as measured by DSC was  $\sim 85^\circ\text{C}$ . This is understandable when compared to the electron microscopy results (Chapter 4: Table 4-1, Figure 5-3) that demonstrated that capsids remained intact at temperatures above the conformational transition temperatures observed in the CD spectra. This verifies that the thermal melting seen in the CD corresponds to only VP1u unfolding and is not a result of whole capsid disassembly.

The different AAV serotypes analyzed show different changes in melting temperature in response to decrease in pH. AAV1 showed a small detectable increase in stability with decrease in pH from 7.5 ( $T_m = 84.8 \pm 0.4$ ) to 5.5 ( $T_m = 87.5 \pm 0.5$ ) and then at pH 4.0 ( $T_m = 81.7 \pm 0.4$ ) it showed a decrease in stability in comparison to pH 7.5 (Table 4-2). AAV5 shows a gradual decrease in melting temperature with decrease in pH from 7.5 ( $T_m = 92.4 \pm 0.3$ ) to 4.0 ( $T_m = 80.3 \pm 0.4$ ) indicating thermal destabilization with decrease in pH (Table 4-2). Unlike AAV1, AAV5 does not show any increase in stability at any of the lower pHs tested. AAV8 at pH 7.5 showed a unique double peak transition (Figure 5-1) ( $74.7 \pm 0.4, 79.1 \pm 0.3$ ) that could potentially signify two different states in the disassembly process. This double peak is not seen at the lower pHs of 6.0,

5.5 and 4.0 (Table 4-2). No transition peaks are observed at the AAV1 and AAV2 (111) VP1u transition temperature ( $\sim 70^\circ \text{C}$ ) for the AAVs studied.

The presence of cell-surface receptor glycans (at 2 receptor molecules : 1 capsid monomer concentration) does not significantly affect the melting temperatures of the AAVs. Neu5Ac  $\alpha$ -2,3 GalNAc  $\beta$ -1,4 GlcNAc was used as a receptor molecule for AAV1 (88). Neu5Ac  $\alpha$ -2,3 Gal  $\beta$ -1,4 GlcNAc was used as a receptor molecule for AAV5 and AAV8. However the presence of  $\text{CaCl}_2$  (2 mM) showed drastic capsid destabilization for AAV1 ( $T_m = 66.5 \pm 0.5$ ) and AAV5 ( $T_m = 74.3 \pm 0.7$ ) at pH 7.5. This was a difference of  $\sim 20^\circ \text{C}$  when compared to the AAV capsids without  $\text{CaCl}_2$  presence. AAV8 did not show destabilization ( $T_m = 76.3 \pm 0.8$ ) with  $\text{CaCl}_2$  presence, but a single peak transition replaced the double peak transition.

AAV1, AAV5 and AAV8 were observed for capsid disassembly and morphological changes by negative stain (Nano-W, Nanoprobes) EM (Figure 5-2). At the four different endosomal pHs tested (7.5, 6.0, 5.5 and 4.0), there was no significant capsid disassembly observed. However, AAV1, AAV5 and AAV8 capsids did show differential stain penetration at the lower pHs when compared to pHs 7.5 and 6.0. The thermal denaturation of the capsids was confirmed by electron microscopy that showed no intact capsids above the melting temperatures seen from the DSC studies (Figure 5-3).

## Discussion

The fact that the melting temperature of the capsid differs from these transition temperature seen for the VP1u transitions (from CD) is a major indicator of the differential structural behavior of the VP1u in comparison to the rest of the capsid. It was also interesting to note that there were no peaks seen corresponding to the thermal

unfolding temperature of the AAV1 or AAV8 VP1u as determined by CD (Chapter 4, Table 4-1).

It is possible that the thermal melting process of the capsid follows a sequence of events for different regions of the capsid. First the VP1u region unfolds followed by the denaturation of the entire capsid. The interactions that hold the capsid monomers together are expected to be of lesser energy than the internal energy of the capsid. However, since a single peak transition was observed from the DSC data for the melting of the capsid, one of two events could be occurring. Either the monomer was unfolding before the capsid inter-monomer interactions were lost (which is very unlikely), or the inter-monomer interactions in the capsid were lost and the unfolding of the monomer was instantaneous. The latter is more likely as the capsid is observed (by electron micrography) to be denatured at the melting temperatures identified by DSC.

The small variations seen in the melting temperatures of the capsids at different pHs were reproducible and distinct. The studied AAV serotypes (AAV1, AAV5 and AAV8) showed different denaturation temperature changes in response to changes in pH. However, the biological effect of these small differences may be debatable as these conditions are not “endosome-like” other than the pH. While pH-induced destabilization of the capsid would promote disassembly of the capsid post-endosomal transport, the consequence of the difference in observed melting temperatures might not be as much as would be required to promote disassembly.

In an attempt to include more endosome-like conditions in the DSC experiments, 2mM CaCl<sub>2</sub> was used in the DSC experiments. The late endosome is known to have

about 2-3 mM  $\text{Ca}^{2+}$  concentration (46).  $\text{Ca}^{2+}$  has been known to affect capsid stability in other non-envelope viruses like Flock House Virus (FHV) (5).

No major morphological differences are observed in the electron micrographs of the capsid at different pHs (7.5, 6.0, 5.5 and 4.0) (Figure 5-2) and temperatures (25° C, 55° C, 75° C) for the AAVs (Figure 5-3). Above the thermal denaturation temperatures for the AAVs (based on DSC data), intact capsids were not observed. While electron micrography may be a very low-resolution method to identify gross morphological changes in the capsid in response to pH, it still is an efficient way of confirming capsid integrity. There was differential stain penetration observed in the AAV1, AAV5 and AAV8 capsids at pHs 5.5 and 4.0 when compared to the higher pHs of 7.5 and 6.0. This can be attributed to structural changes in the capsid that could affect the permeability and staining properties of the capsid.

While thermal stability would be one way of analyzing the inherent stability of the capsid, other methods to analyze structural stability would involve the unfolding/denaturation process of the capsid with increasing chaotropic salt (for example, Guanidium-HCl) concentration. Previous studies on MVM identified that the presence of 1.5 M Guanidium-HCl decreased the melting temperature by ~15° C (18) indicating that the folded state of the capsid had a role in determining the thermal stability of the capsid. This would be a way of testing if, for the AAVs, changes in stability seen in the capsids were a result of increased unfolded states of the capsid or individual regions of the capsid.

This study determines the melting temperatures for the AAV serotypes at different pHs. There are small changes in the melting temperatures at different pHs. These

melting temperatures are different from the transition temperatures seen from CD experiments. These differences show that DSC and CD are measuring two different independent properties of the capsid. This study would impact our understanding the process of AAV capsid disassembly and post-endosomal trafficking.

Table 5-1. Association energies and buried surface areas for AAV8 at pHs 7.5 and 4.0. This data was calculated using the VIPERdb server.

pHs	Association Energy (kcal/mol)			Buried Surface Area (Å <sup>2</sup> )		
	I-2	I-3	I-5	I-2	I-3	I-5
pH 7.5	-67.4	-213.1	-102.1	3235	10373	5058
pH 4	-63.8	-213.7	-101.6	3082	10411	5033

Table 5-2. DSC melting temperatures (in ° C).

	AAV1	AAV5	AAV8
pH 7.5	84.8 ± 0.4	92.4 ± 0.3	74.7 ± 0.4, 79.1 ± 0.3
pH 6.0	86.2 ± 0.7	91.9 ± 0.5	79.1 ± 0.6
pH 5.5	87.5 ± 0.5	83.5 ± 0.9	78.6 ± 0.5
pH 4.0	81.7 ± 0.4	80.3 ± 0.4	73.2 ± 0.8
Back to pH 7.5	85.1 ± 0.3	92.6 ± 0.7	77.5 ± 0.8
Presence of receptor pH 7.5	86.5 ± 0.6	91.5 ± 0.8	75.6 ± 0.5
Presence of receptor pH 5.5	86.2 ± 0.3	84.1 ± 0.6	75.3 ± 0.7
Calcium presence pH 7.5	66.5 ± 0.5	74.3 ± 0.7	76.3 ± 0.8

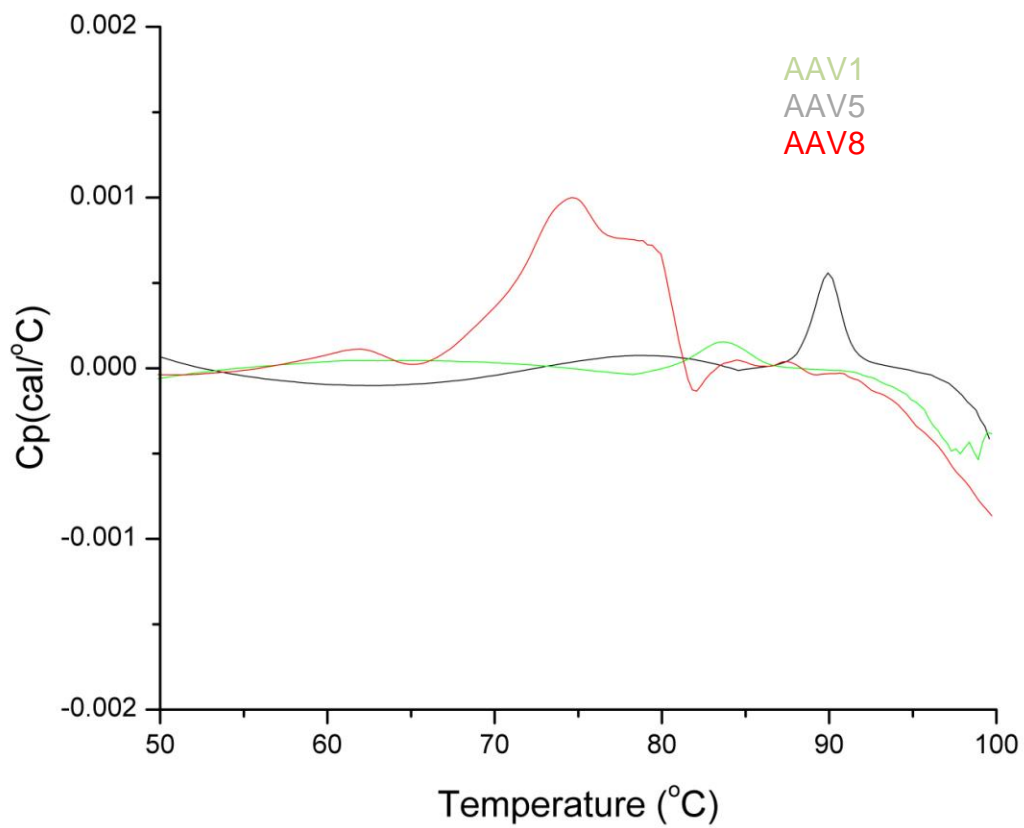


Figure 5-1. DSC curves for AAV1, AAV5 and AAV8. This plot of Temperature versus enthalpy value (Cp) shows the thermal denaturation temperatures for AAV1 (green), AAV5 (gray) and AAV8 (red) as signified by the peaks. The data was plotted using Origin (OriginLab, Northampton, MA)

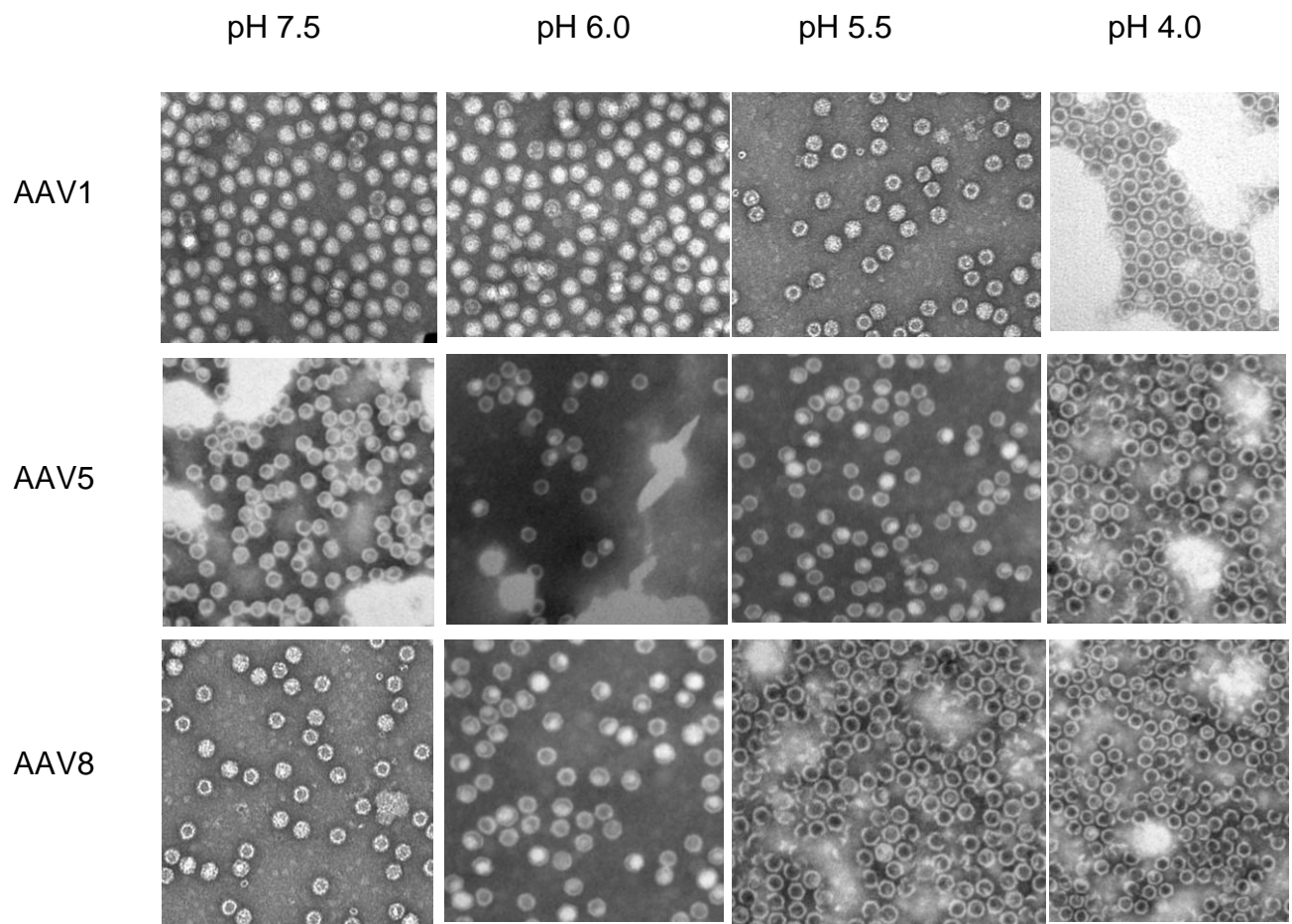


Figure 5-2. Electron micrographs of AAVs 1, 5 and 8 at different pHs. It can be seen that the capsids stay intact even at low pHs. The capsids were stained with Nano-W and the micrographs were collected at 50,000X magnification.

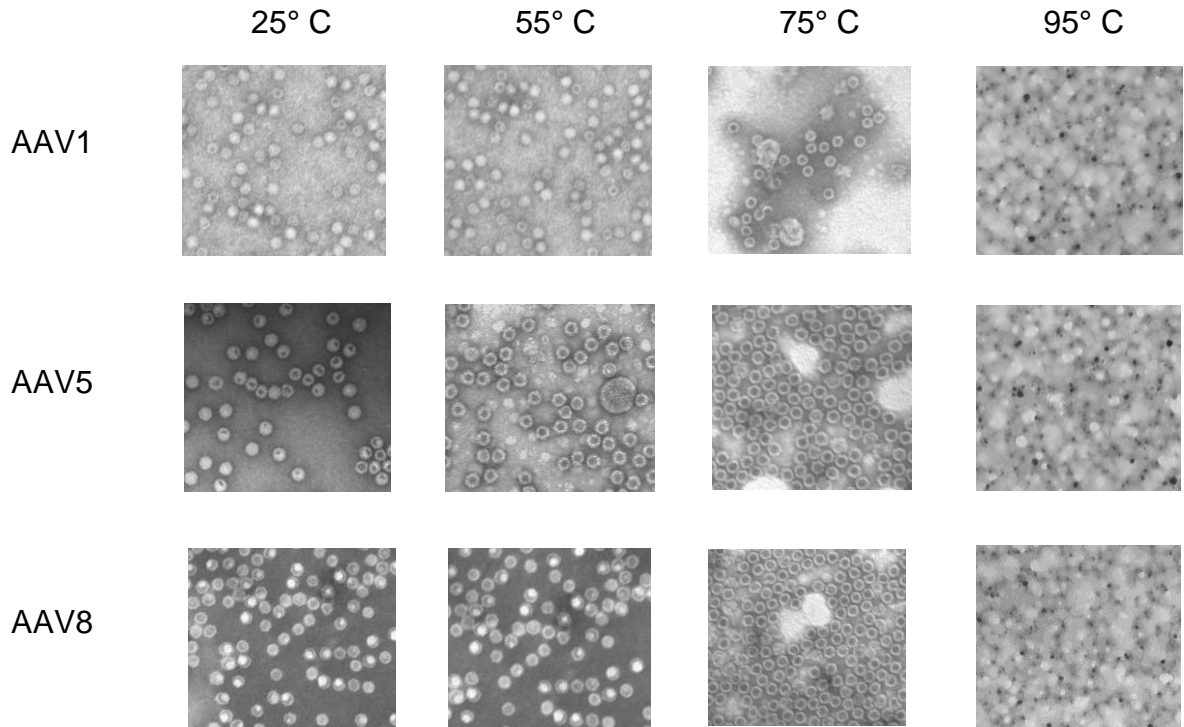


Figure 5-3. Electron micrographs of AAVs 1,5 and 8 at different temperatures. Intact capsids were observed at 25° C, 55° C and 75° C. At 95° C the capsids were found to be denatured. The capsids were stained with Nano-W and the micrographs were collected at 50,000X magnification.

## CHAPTER 6 NOVEL PROTEOLYTIC ACTIVITY IN ADENO-ASSOCIATED VIRUSES

### **Background**

Several virus families have previously been shown to exhibit protease activity, essential to their infectious pathway, these include: Aspartic proteases found in human immunodeficiency virus, nodavirus and tetra virus (59, 66); Cysteine proteases found in poliovirus protease 3C, hepatitis C virus, and foot-and-mouth disease virus L-peptidase (9, 50, 123); and Serine proteases found in astrovirus, Sindbis virus, and tellina virus, among others (2, 8, 95).

Previous studies using two-hybrid screens showed that the AAVs were susceptible to cathepsins B and L and that these cathepsins are essential for AAV2 and AAV8 mediated transduction of mammalian cells (1). This data suggested that cleavage events in the endosome, could prime the AAV capsid for nuclear uncoating. Of note, was the observation that long-term stored AAV capsids often exhibited *in vitro* degradation of VP1-3 (as indicated on SDS-gels, Figure 6-1), which implies that a self-protease activity was possible. Upon close inspection of the AAV2 crystal structure (131) using the interactive modeling program COOT(34), a surface exposed region, near the three-fold axis (E531, D561, E563 and H527) was identified that had structural characteristics of a possible aspartic protease catalytic triad (Figure 6-2, Figure 6-3). Furthermore this site was semi-conserved between all the known AAV structures in the VP1, VP2 and VP3 sequence and implied in the other known sequences (Table 6-1).

### **Results**

Degradation products were observed in B1 antibody (125) western blot analysis of wild type and mutant AAV2 capsids. The B1 antibody was directed towards a linear

epitope in the C-terminal region of VP1, VP2 and VP3 capsid proteins (125). This degradation increased at pH 5.0 in comparison to pH 7.5. One consistent degradation product was observed to be ~ 15 kDa in size. Mass spectrometry analysis (not shown) suggested that multiple potential cleavage sites on the AAV2 capsid sequence. Mutants at these cleavage sites (N469A, S498A, N582A, R585A and D219A) however were unable to abolish protease activity entirely and the degradation products were still observed using western blots.

Protease activity assays were also used to determine if the AAVs tested (AAV1, AAV2, AAV5 and AAV8) had protease activity (Protocol described in Chapter 2). The protease activity assays clearly showed positive for the AAVs tested at pH 7.5 but not 5.5, when compared to the positive (equal molar concentration of trypsin) and negative (buffer and equal molar concentration of carbonic anhydrase) controls (Figure 6-4), with a measured cleavage activity of ~ 1/3 that of trypsin (as seen from the optical density values). As the viruses were concentrated for the assay, the sample flow through (Citrate-Phosphate buffer with 150mM NaCl) was collected and used as a negative control to ensure that the observed protease activity was not an artifact of a contaminant protease in the buffer or the purification process. A test against an uninfected *sf9* lysate supernatant confirmed that the activity seen was not from an impurity from the cells. The observed activities were comparable to protease activities previously reported using this kit (29, 80). Within the experimental uncertainty of the experiment no conclusions could be made to the relative rates of protease activity between the AAVs tested. To confirm that the observations were a proteolytic reaction, the pH 7.5 experiments were repeated in the presence of a cocktail of protease

inhibitors (HALT™ Protease inhibitor Single-Use Cocktail from Thermo Scientific) (Figure 6-5). This stopped the protease activity as the measured ODs were reduced to the negative control values, as was the control - trypsin. Protease activity was also abolished in an AAV2 mutant E563A (preparation and purification described in Chapter 2) (Figure 6-5). To test if DNA packaging in the capsid had an effect on the OD values in GFP-coding DNA packaged AAV8 were assayed. An increase in the protease activity was seen (Figure 6-4) indicating a role for DNA in enhancing protease activity.

### **Discussion**

This study has identified autoproteolytic activity in the capsids of AAV1, AAV2, AAV5 and AAV8. Western blot analysis (Figure 6-1) confirm that lower-molecular weight degradation products are seen for the AAVs and the intensity of these products on the blot increases with decrease in pH from 7.0 to 5.0, indicating that pH has a role in the AAV protease activity. Mutagenesis experiments (N469A, S498A, N582A, R585A and D219A) followed by mass spectrometry and western blot analysis (Figure 6-1) were used to identify the cleavage site but data so far has been inconclusive.

Based on the conserved VP3 structure of AAVs a comparative analysis of the other known AAV structures (AAVs 1-9), showed a putative aspartic catalytic triad (in AAVs 1-9 with the exception of AAV5) for (Table 6-1), which involves the coordination of a water molecule between the two aspartate residues. This may also be the case where one of the aspartates is replaced with a glutamate, in the case of AAV2, AAV4, and AAV9, (Glutamic proteases, Table 6-1). In addition, the other AAVs have amino clusters that could be potential Serine or other yet unclassified proteases. An AAV2 mutant E563A showed absence of protease activity when tested (Figure 6-5). This may indicate a role for this site in the proposed protease activity.

The observation that AAV1, AAV2, AAV5, and AAV8, exhibit protease activity at pH 7.5 but not 5.5, would imply this enzymatic process is required either pre- or post-endosomal entry for efficient infection during virus trafficking through the cytoplasm. Previous studies have identified endosomal cathepsins B and L as uncoating factors for AAV2 and AAV8 (1). The autoproteolytic activity seen in the AAVs is also susceptible to decrease in endosome-like pH levels. It is possible that these activities seen are related or synergistic.

The effect of mutating surface accessible amino acids (that are postulated as involved in the protease activity) is currently in progress as is the identification of what type of protease the AAVs are. This can be done by assaying the AAVs for protease activity in presence of inhibitors specific to each type of protease separately. The role for proteolytic activity in the infective pathway of the AAVs is unknown but since this activity is affected by change in pH, it is possible that the proteolytic activity may be seen when the AAVs are trafficked through the endosome.

Table 6-1. Amino acid conservation in the catalytic triad region.

AAV	Amino acid number and type
1	532Asp, 562Asp, 527His, 564Glu
2	531Glu, 561Asp, 526His, 563Glu
3	532Asp, 562Asp, 527His, 564Glu
4	530Asp, 560Ser, 527Gly
5	518Ser, 551Ser, 514Asn
6	532Asp, 562Asp, 527His, 564Glu
7	514Asn, 518Ser, 551Ser
8	534Glu, 564Ser, 529His
9	532Asp, 562Asn, 527His, 564Glu



Figure 6-1. Western Blot of AAV2 wild type and mutants showing degradation products. A set of degradation products are seen in below the VP3 band. There is an increase of degradation products at pH 5.0 when compared to pH 7.5. The bands were probed with a B1 antibody directed towards the C-terminal domain of the VP1, VP2 and VP3 capsid proteins. This image was taken from Max Salganik.

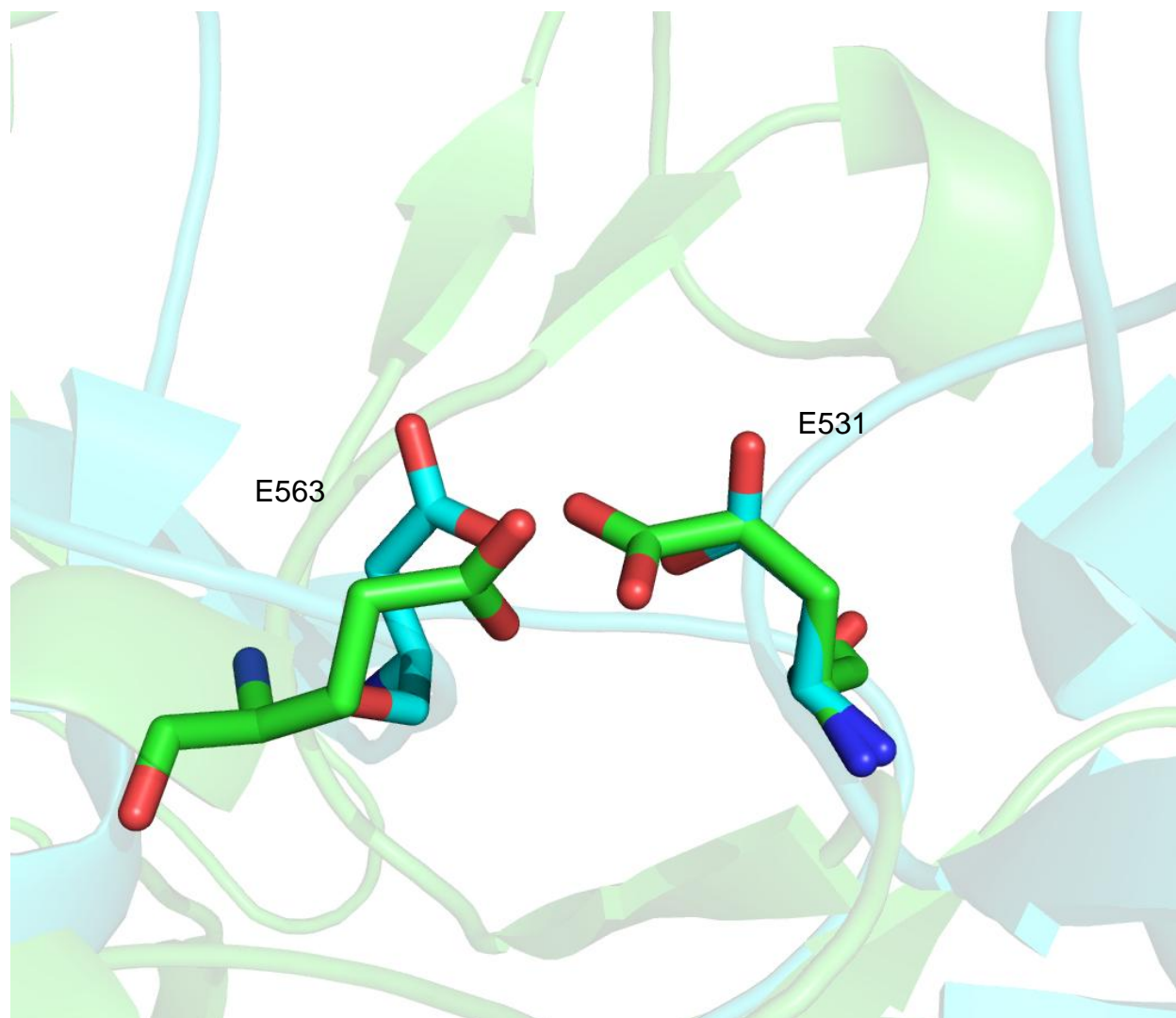


Figure 6-2. Superimposition of hypothesized aspartic protease sites (AAV2) onto catalytic aspartates of an aspartic protease (HIV1 protease). The AAV2 residues (blue) are show similar orientation and proximity as the aspartic protease (green) catalytic aspartates. This figure was made using PyMOL (DeLano Scientific).

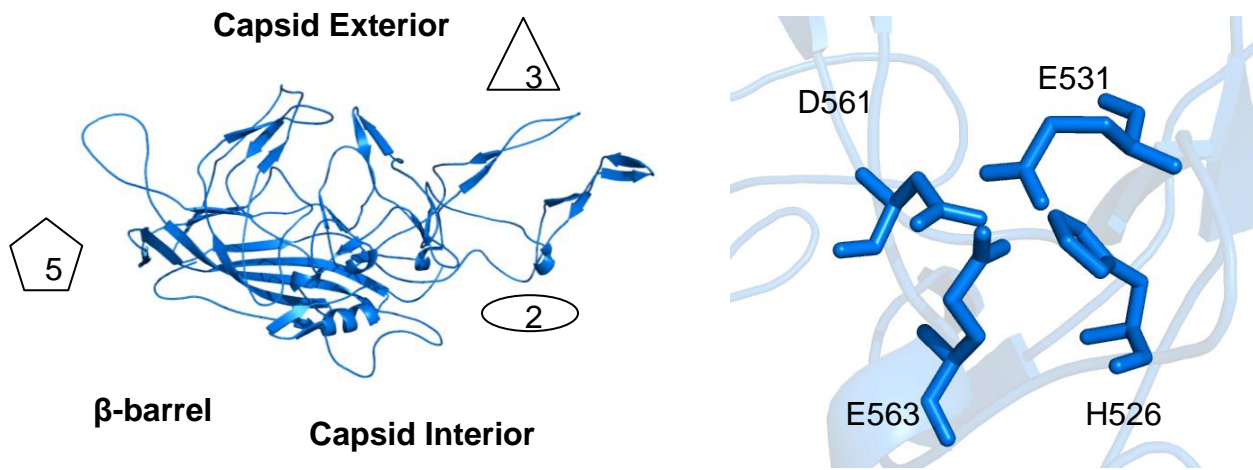


Figure 6-3. AAV1 capsid structure. A) Ribbon diagram of the VP3 structure. The positions of icosahedral 5-, 3-, and 2- fold symmetry axes are as labeled. B) Close-up view of the putative catalytic active site, amino acids are as labeled. The yellow sphere represents an ordered solvent molecule observed in the crystal structure. The figure was generated in PyMOL.

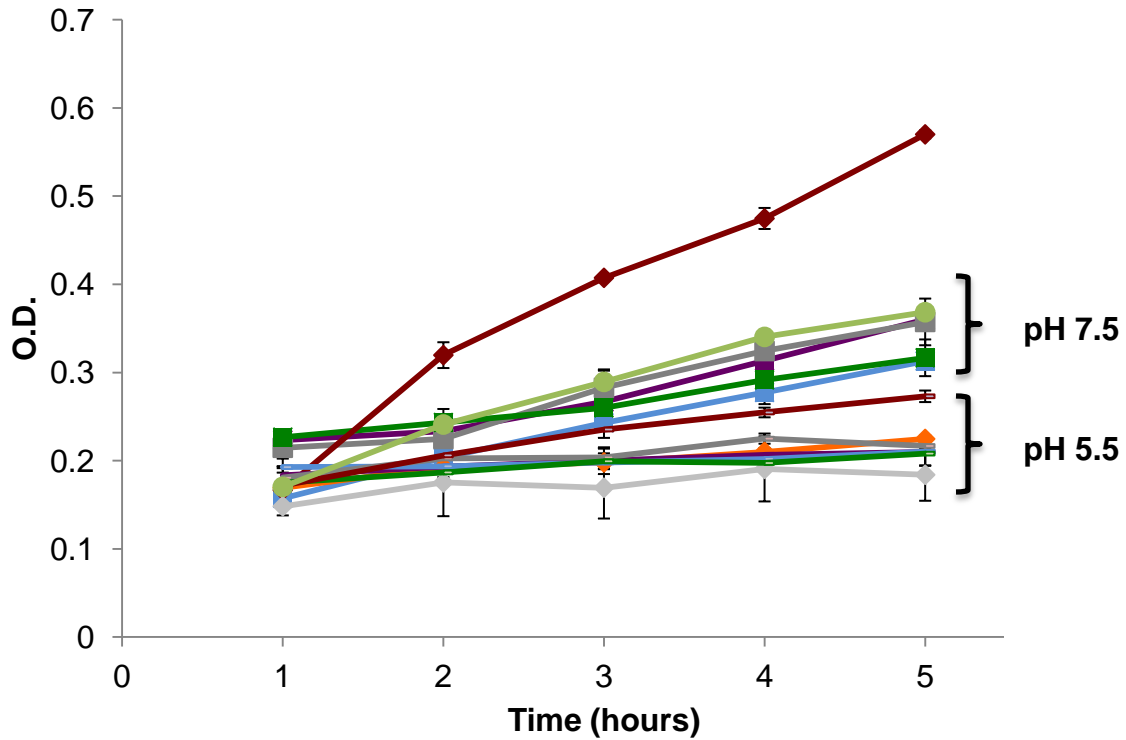


Figure 6-4. Protease activity for AAV1, AAV2, AAV5, and AAV8 at pH 7.5 and 5.5. Plotted are AAV1 (purple), AAV2 (light blue), AAV5 (dark grey), AAV8 (green) (at pH 7.5 and 5.5) and AAV8 with GFP-coding DNA packaged (lime green). Also shown are Trypsin (red - positive control) carbonic anhydrase (orange - negative control) and buffer (light grey - negative control). The OD readings are given in arbitrary units. Each data point was measured in triplicate.

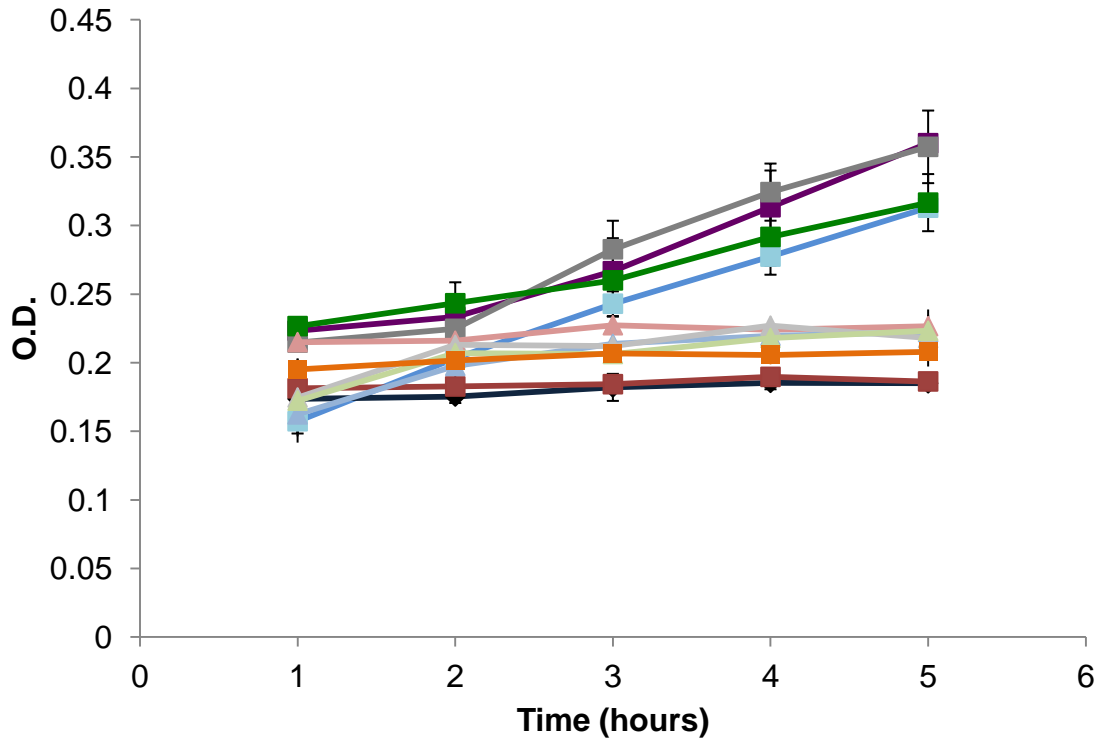


Figure 6-5. Protease activity assay plots for AAV1, AAV2, AAV5 and AAV8 in presence of inhibitors. Plotted are AAV1 (purple), AAV2 (blue), AAV5 (dark grey) and AAV8 (green). With inhibitor presence AAV1 (pink), AAV2 (light blue), AAV5 (light grey), AAV8 (light green) and trypsin (orange) show lack of activity. The AAV2 mutant E563A (black) and the mock cell extract (crimson) also show lack of activity.

## CHAPTER 7 SUMMARY AND FUTURE DIRECTIONS

The crucial role of the VP1u region and structural changes associated with it has been well documented by this study and others (13, 69, 111). But the cellular factors that trigger these changes and the nature of these changes have not yet been established. The primary focus of this study is to establish the nature of the structural changes in the VP1u changes and determine the biological trigger to structural changes in the capsid and the VP1u region. It was determined by CD based assays that the VP1u externalization event that previously was seen in response to high temperature (111) involves the unfolding of the VP1u region. This unfolding occurs in response to temperature as determined previously and pH as well (Chapter 4). The response to pH would be expected, as pH changes are one the primary features of the endosome.

However, while unfolding of the VP1u region has been established, the second step of the mechanism that would involve the process of externalization of the unfolded VP1u has not yet been identified. It can be hypothesized that the unfolded VP1u can be threaded out through the 5-fold pore (based on work by Levy *et al.* (73)) and the ionic state of the VP1u at late endosomal pH could be a trigger to cause the VP1u to thread out.

When the pH of the environment is decreased from 7.5 to 4.0 and then restored to 7.5, CD studies showed reversal of the secondary structural state of the VP1u. This was in agreement with the reversible structural changes seen in the AAV8 crystal structure solved at different pHs (7.5, 6.0, 5.5, 4.0 and at 7.5 restored) (86). A restoration of physiological pH may or may not be the biological trigger for VP1u refolding. This study still proves that the VP1u has the intrinsic propensity to refold to a native functional

state. It is possible that once the VP1u is in contact with the lipid membrane of the endosome, it refolds to regenerate the PLA<sub>2</sub> active site to carry out its function of lysing the endosomal membrane for capsid escape. An analysis of the AAV VP1u sequence indicates a putative C2 lipid binding domain (112) activity, which would be expected for most phospholipases. Future experiments would involve the testing of interactions between the AAV capsid and an *in vitro* reconstitution of the lipid membrane. A number of different techniques can be used to analyze the interactions but one way of biophysically analyzing the interactions would be to label the lipid layer and the capsid with spin labels or fluorescent labels to test by Double Electron-Electron Resonance (DEER) spectroscopy or Forster's Resonance Energy Transfer (FRET) respectively. These methods can be optimized to analyze multiple aspects of the interaction between the lipid layer and the PLA<sub>2</sub> domain like binding, conformational change and even activity. While it has been established that the VP1u contains a PLA<sub>2</sub> activity, the level of activity is still very low in comparison to more potent PLA<sub>2</sub>s like bee venom (107) or snake venom phospholipase (124). Due to this, there have been some concerns on whether the AAV PLA<sub>2</sub> is indeed a true phospholipase. Previous studies do, however, indicate that mutations in the PLA<sub>2</sub> active site motif on AAV2 decrease infectivity (113). Since the VP1u has been known to externalize at high temperature for the AAVs (111), this method has routinely been used to test the AAVs for phospholipase activity. This however can be a destructive method for phospholipase activity determination. As it has been identified in this study, the VP1u domain irreversibly unfolds at the same temperatures used to externalize the VP1u domain. Therefore, it is possible that the low activity seen for the AAV PLA<sub>2</sub> is due to the loss of structure and a resultant loss of

function of the VP1u region. Determining the biological trigger for externalization would be a huge boost to understanding the enzymatic nature of AAV PLA<sub>2</sub> domains.

A construct of the VP1u alone would also be very useful in studying its functions and verifying its structural properties. Some of the major challenges to studying the VP1u region include the unstructured state of the VP1/2 common region and the low copy number of the VP1u region.

While the pI differences between the VP1u and the other regions of the capsid can effect the unique behavior of the VP1u, it may also have a role in determining copy number during the process of capsid assembly. It is very possible that mutations in specific polar or charged residues can alter the electronic configuration of the whole capsid. It would be interesting to see how copy numbers in the capsid are altered by mutagenesis in charged residues that are not located at the inter-monomeric interfaces.

While this study has employed a reductionist approach to *in vitro* simulation of endosomal conditions by studying just pH alone, using other endosomal factors could be key to identifying the actual biological mechanism of endosomal escape. Along with changes in pH the endosome also involves large changes in ionic strength. It may be difficult to account for all the different ions present in the endosome partly because the concentration of a lot of these ions at different endosomal states is still not known properly. One of the known factors is that there is a large decrease in endosomal Ca<sup>2+</sup> (from ~ 30 mM – early endosome to ~ 3 mM – late endosome) ion concentration (46) but an increase in Cl<sup>-</sup> ion concentration. CaCl<sub>2</sub> was identified to destabilize the capsid for AAV1, AAV5 and AAV8. While the implication of this in the endosomal trafficking process is unclear, there is still a major effect of ionic presence on the capsid structure.

The presence of the glycan receptor moieties has not shown any major structural or stability changes to the capsid. It is possible that the glycans will have to be in glycoprotein form to effect structural changes in the capsid, if indeed they have a role in the process. It would be good to test if the presence of co-receptors could have an effect as well.

There seems to be a lot of diversity in the intracellular trafficking process for the AAVs after endosomal escape (53). This study does not shine much light on this area but the altered state of the capsid is important to focus on when looking at post-endosomal trafficking and changes in the capsid. There is some recent evidence suggesting that the AAVs interact with an endoplasmic reticulum (ER) chaperone protein GRP78 (60). This could suggest that the AAVs could exploit the intracellular retrograde transport system and move from the Golgi to the ER to get closer to the nucleus. It would be useful to biophysically analyze the capsid structure under more oxidizing ER conditions.

Most previous studies have employed antibody assays as the primary means of determining the structural changes occurring in the endosome (69, 111). While these assays have been very useful, they are limited by a number of factors including the indirect nature of the assays and the difference in binding ability of the antibodies with changes in conditions. For example, at lower pH (< 7.5), the A1 antibody (128) (directed towards the VP1u region) does not bind well (data not shown). This could be because of the presence of a Glutamate residue in the linear epitope for A1 (128). It is also difficult to check if the binding of A1 is seen as a result of capsid breakage. While there are structural antibodies that bind to intact capsids, they have been seen to still bind to

disassembled capsid products. The design of more robust antibodies would help experiments be a lot more reproducible. A good antibody assay system would be a good compliment to biophysical analysis of capsid structural transitions.

A novel protease activity in the AAVs has been identified in this study. While this study is very preliminary in characterizing the role of protease activity in the trafficking and infective pathway of the virus, it is possible that the activity seen in the virus could have a role in the slow disassembly of the virus. This autocatalytic nature of the virus adds a new dimension to the understanding of the viral life cycle. Further studies would involve the identification of the enzymatic nature of the protease activity and the potential substrate and the effect of mutagenesis of protease activity residues on the infectivity of the virus.

This study adds to our understanding of the structural basis of intracellular viral trafficking in a substantial way. While the direct use of this data in clinical gene therapy may be limited, a thorough understanding of the viral life cycle would go a long way in developing better gene therapy strategies and add to our fundamental understanding of non-envelope viral life cycles.

## LIST OF REFERENCES

1. **Akache B., D. Grimm, X. Shen, S. Fuess, S. R. Yant, D. S. Glazer, J. Park, and M. A. Kay.** 2007. A two-hybrid screen identifies cathepsins B and L as uncoating factors for adeno-associated virus 2 and 8. *Mol. Ther.* **15**:330–339.
2. **Aliperti G., and M. J. Schlesinger.** 1978. Evidence for an autoprotease activity of sindbis virus capsid protein. *Virology* **90**:366–369.
3. **Ausar S. F., T. R. Foubert, M. H. Hudson, T. S. Vedvick, and C. R. Middaugh.** 2006. Conformational stability and disassembly of Norwalk virus-like particles. Effect of pH and temperature. *J. Biol. Chem.* **281**:19478–19488.
4. **Balsinde J., M. A. Balboa, P. A. Insel, and E. A. Dennis.** 1999. Regulation and inhibition of phospholipase A2. *Annu. Rev. Pharmacol. Toxicol.* **39**:175–189.
5. **Banerjee M., J. A. Speir, M. H. Kwan, R. Huang, P. P. Aryanpur, B. Bothner, and J. E. Johnson.** 2010. Structure and function of a genetically engineered mimic of a nonenveloped virus entry intermediate. *J. Virol.* **84**:4737–4746.
6. **Bantel-Schaal U., B. Hub, and J. Kartenbeck.** 2002. Endocytosis of adeno-associated virus type 5 leads to accumulation of virus particles in the Golgi compartment. *J. Virol.* **76**:2340–2349.
7. **Bartlett J. S., R. Wilcher, and R. J. Samulski.** 2000. Infectious entry pathway of adeno-associated virus and adeno-associated virus vectors. *J. Virol.* **74**:2777–2785.
8. **Bass D. M., and S. Qiu.** 2000. Proteolytic Processing of the Astrovirus Capsid. *J. Virol.* **74**:1810–1814.
9. **Belsham G. J., G. M. McInerney, and N. Ross-Smith.** 2000. Foot-and-Mouth Disease Virus 3C Protease Induces Cleavage of Translation Initiation Factors eIF4A and eIF4G within Infected Cells. *J. Virol.* **74**:272–280.
10. **Berns K. I.** 1990. Parvovirus replication. *Microbiol. Rev.* **54**:316–329.
11. **Blechacz B., and S. J. Russell.** 2004. Parvovirus vectors: use and optimisation in cancer gene therapy. *Expert Rev Mol Med* **6**:1–24.
12. **Bleker S., M. Pawlita, and J. A. Kleinschmidt.** 2006. Impact of capsid conformation and Rep-capsid interactions on adeno-associated virus type 2 genome packaging. *J. Virol.* **80**:810–820.

13. **Bleker S., F. Sonntag, and J. A. Kleinschmidt.** 2005. Mutational analysis of narrow pores at the fivefold symmetry axes of adeno-associated virus type 2 capsids reveals a dual role in genome packaging and activation of phospholipase A2 activity. *J. Virol.* **79**:2528–2540.
14. **Brabec M., D. Schober, E. Wagner, N. Bayer, R. F. Murphy, D. Blaas, and R. Fuchs.** 2005. Opening of size-selective pores in endosomes during human rhinovirus serotype 2 in vivo uncoating monitored by single-organelle flow analysis. *J. Virol.* **79**:1008–1016.
15. **Brünger A. T., P. D. Adams, G. M. Clore, W. L. DeLano, P. Gros, R. W. Grosse-Kunstleve, J. S. Jiang, J. Kuszewski, M. Nilges, N. S. Pannu, R. J. Read, L. M. Rice, T. Simonson, and G. L. Warren.** 1998. Crystallography & NMR system: A new software suite for macromolecular structure determination. *Acta Crystallogr. D Biol. Crystallogr.* **54**:905–921.
16. **Burger C., O. S. Gorbatyuk, M. J. Velardo, C. S. Peden, P. Williams, S. Zolotukhin, P. J. Reier, R. J. Mandel, and N. Muzyczka.** 2004. Recombinant AAV Viral Vectors Pseudotyped with Viral Capsids from Serotypes 1, 2, and 5 Display Differential Efficiency and Cell Tropism after Delivery to Different Regions of the Central Nervous System. *Mol Ther* **10**:302–317.
17. **Canaan S., Z. Zádori, F. Ghomashchi, J. Bollinger, M. Sadilek, M. E. Moreau, P. Tijssen, and M. H. Gelb.** 2004. Interfacial enzymology of parvovirus phospholipases A2. *J. Biol. Chem.* **279**:14502–14508.
18. **Carreira A., M. Menéndez, J. Reguera, J. M. Almendral, and M. G. Mateu.** 2004. In vitro disassembly of a parvovirus capsid and effect on capsid stability of heterologous peptide insertions in surface loops. *J. Biol. Chem.* **279**:6517–6525.
19. **Carrillo-Tripp M., C. M. Shepherd, I. A. Borelli, S. Venkataraman, G. Lander, P. Natarajan, J. E. Johnson, C. L. Brooks 3rd, and V. S. Reddy.** 2009. VIPERdb2: an enhanced and web API enabled relational database for structural virology. *Nucleic Acids Res.* **37**:D436–442.
20. **Chao H., Y. Liu, J. Rabinowitz, C. Li, R. J. Samulski, and C. E. Walsh.** 2000. Several Log Increase in Therapeutic Transgene Delivery by Distinct Adeno-Associated Viral Serotype Vectors. *Mol Ther* **2**:619–623.
21. **Chapman M. S., and M. Agbandje-McKenna.** Atomic structure of viral particles, p. 107–123. *In Parvoviruses.* Edward Arnold Ltd., New York.
22. **Chargaff E., and J. N. Davidson.** 1960. *The nucleic acids: chemistry and biology.* Academic Press.

23. **Chivian D., D. E. Kim, L. Malmström, P. Bradley, T. Robertson, P. Murphy, C. E. M. Strauss, R. Bonneau, C. A. Rohl, and D. Baker.** 2003. Automated prediction of CASP-5 structures using the Robetta server. *Proteins* **53 Suppl 6**:524–533.
24. **Cotmore S. F., A. M. D'abramo Jr, C. M. Ticknor, and P. Tattersall.** 1999. Controlled conformational transitions in the MVM virion expose the VP1 N-terminus and viral genome without particle disassembly. *Virology* **254**:169–181.
25. **Davidson B. L., C. S. Stein, J. A. Heth, I. Martins, R. M. Kotin, T. A. Derksen, J. Zabner, A. Ghodsi, and J. A. Chiorini.** 2000. Recombinant adeno-associated virus type 2, 4, and 5 vectors: Transduction of variant cell types and regions in the mammalian central nervous system. *Proceedings of the National Academy of Sciences* **97**:3428 –3432.
26. **Delano W.** 2002. The PyMOL Molecular Graphics System.
27. **Dennis E. A.** 1997. The growing phospholipase A2 superfamily of signal transduction enzymes. *Trends Biochem. Sci.* **22**:1–2.
28. **Dijkstra B. W., K. H. Kalk, W. G. Hol, and J. Drenth.** 1981. Structure of bovine pancreatic phospholipase A2 at 1.7Å resolution. *J. Mol. Biol.* **147**:97–123.
29. **Domisch H., W. O. Chung, M. G. Rohani, D. Williams, M. Rangarajan, M. A. Curtis, and B. A. Dale.** 2007. Protease-activated receptor 2 mediates human beta-defensin 2 and CC chemokine ligand 20 mRNA expression in response to proteases secreted by *Porphyromonas gingivalis*. *Infect. Immun.* **75**:4326–4333.
30. **Douar A. M., K. Poulard, D. Stockholm, and O. Danos.** 2001. Intracellular trafficking of adeno-associated virus vectors: routing to the late endosomal compartment and proteasome degradation. *J. Virol.* **75**:1824–1833.
31. **Duan D., Q. Li, A. W. Kao, Y. Yue, J. E. Pessin, and J. F. Engelhardt.** 1999. Dynamin is required for recombinant adeno-associated virus type 2 infection. *J. Virol.* **73**:10371–10376.
32. **Duan D., Y. Yue, Z. Yan, J. Yang, and J. F. Engelhardt.** 2000. Endosomal processing limits gene transfer to polarized airway epithelia by adeno-associated virus. *J. Clin. Invest.* **105**:1573–1587.
33. **Edwards J., E. Mann, and D. T. Brown.** 1983. Conformational changes in Sindbis virus envelope proteins accompanying exposure to low pH. *J. Virol.* **45**:1090–1097.

34. **Emsley P., and K. Cowtan.** 2004. Coot: model-building tools for molecular graphics. *Acta Crystallogr D Biol Crystallogr* **60**:2126–2132.
35. **Farr G. A., S. F. Cotmore, and P. Tattersall.** 2006. VP2 cleavage and the leucine ring at the base of the fivefold cylinder control pH-dependent externalization of both the VP1 N terminus and the genome of minute virus of mice. *J. Virol.* **80**:161–171.
36. **Farr G. A., and P. Tattersall.** 2004. A conserved leucine that constricts the pore through the capsid fivefold cylinder plays a central role in parvoviral infection. *Virology* **323**:243–256.
37. **Farr G. A., L. Zhang, and P. Tattersall.** 2005. Parvoviral virions deploy a capsid-tethered lipolytic enzyme to breach the endosomal membrane during cell entry. *Proc. Natl. Acad. Sci. U.S.A.* **102**:17148–17153.
38. **Ferrari F. K., T. Samulski, T. Shenk, and R. J. Samulski.** 1996. Second-strand synthesis is a rate-limiting step for efficient transduction by recombinant adeno-associated virus vectors. *J. Virol.* **70**:3227–3234.
39. **Fields B. N., D. M. Knipe, and P. M. Howley.** 2007. *Fields' virology.* Lippincott Williams & Wilkins.
40. **Fisher K. J., G. P. Gao, M. D. Weitzman, R. DeMatteo, J. F. Burda, and J. M. Wilson.** 1996. Transduction with recombinant adeno-associated virus for gene therapy is limited by leading-strand synthesis. *J. Virol.* **70**:520–532.
41. **Fricks C. E., and J. M. Hogle.** 1990. Cell-induced conformational change in poliovirus: externalization of the amino terminus of VP1 is responsible for liposome binding. *J. Virol.* **64**:1934–1945.
42. **Friedmann T.** 1999. *The development of human gene therapy.* CSHL Press.
43. **Gao G.-P., M. R. Alvira, L. Wang, R. Calcedo, J. Johnston, and J. M. Wilson.** 2002. Novel adeno-associated viruses from rhesus monkeys as vectors for human gene therapy. *Proceedings of the National Academy of Sciences* **99**:11854 –11859.
44. **Gao G., L. H. Vandenberghe, M. R. Alvira, Y. Lu, R. Calcedo, X. Zhou, and J. M. Wilson.** 2004. Clades of Adeno-Associated Viruses Are Widely Disseminated in Human Tissues. *Journal of Virology* **78**:6381 –6388.
45. **Gasteiger E., C. Hoogland, A. Gattiker, S. Duvaud, M. R. Wilkins, R. D. Appel, and A. Bairoch.** 2005. Protein Identification and Analysis Tools on the ExPASy Server, p. 571–607. *In* J.M. Walker (ed.), *The Proteomics Protocols Handbook.* Humana Press, Totowa, NJ.

46. **Gerasimenko J. V., A. V. Tepikin, O. H. Petersen, and O. V. Gerasimenko.** 1998. Calcium uptake via endocytosis with rapid release from acidifying endosomes. *Curr. Biol.* **8**:1335–1338.
47. **Govindasamy L., E. Padron, R. McKenna, N. Muzyczka, N. Kaludov, J. A. Chiorini, and M. Agbandje-McKenna.** 2006. Structurally Mapping the Diverse Phenotype of Adeno-Associated Virus Serotype 4. *Journal of Virology* **80**:11556 –11570.
48. **Greenfield N. J., and G. D. Fasman.** 1969. Computed circular dichroism spectra for the evaluation of protein conformation. *Biochemistry* **8**:4108–4116.
49. **Grieger J. C., S. Snowdy, and R. J. Samulski.** 2006. Separate basic region motifs within the adeno-associated virus capsid proteins are essential for infectivity and assembly. *J. Virol.* **80**:5199–5210.
50. **Hanecak R., B. L. Semler, C. W. Anderson, and E. Wimmer.** 1982. Proteolytic processing of poliovirus polypeptides: antibodies to polypeptide P3-7c inhibit cleavage at glutamine-glycine pairs. *Proceedings of the National Academy of Sciences of the United States of America* **79**:3973 –3977.
51. **Hansen J., K. Qing, H. J. Kwon, C. Mah, and A. Srivastava.** 2000. Impaired intracellular trafficking of adeno-associated virus type 2 vectors limits efficient transduction of murine fibroblasts. *J. Virol.* **74**:992–996.
52. **Hansen J., K. Qing, and A. Srivastava.** 2001. Adeno-associated virus type 2-mediated gene transfer: altered endocytic processing enhances transduction efficiency in murine fibroblasts. *J. Virol.* **75**:4080–4090.
53. **Harbison C. E., J. A. Chiorini, and C. R. Parrish.** 2008. The parvovirus capsid odyssey: from the cell surface to the nucleus. *Trends Microbiol.* **16**:208–214.
54. **Hauck B., and W. Xiao.** 2003. Characterization of tissue tropism determinants of adeno-associated virus type 1. *J. Virol.* **77**:2768–2774.
55. **Hauck B., W. Zhao, K. High, and W. Xiao.** 2004. Intracellular viral processing, not single-stranded DNA accumulation, is crucial for recombinant adeno-associated virus transduction. *J. Virol.* **78**:13678–13686.
56. **Hermonat P. L., and N. Muzyczka.** 1984. Use of adeno-associated virus as a mammalian DNA cloning vector: transduction of neomycin resistance into mammalian tissue culture cells. *Proceedings of the National Academy of Sciences* **81**:6466 –6470.

57. **Hernando E., A. L. Llamas-Saiz, C. Foces-Foces, R. McKenna, I. Portman, M. Agbandje-McKenna, and J. M. Almendral.** 2000. Biochemical and physical characterization of parvovirus minute virus of mice virus-like particles. *Virology* **267**:299–309.
58. **Inagaki K., S. Fuess, T. A. Storm, G. A. Gibson, C. F. Mctiernan, M. A. Kay, and H. Nakai.** 2006. Robust Systemic Transduction with AAV9 Vectors in Mice: Efficient Global Cardiac Gene Transfer Superior to That of AAV8. *Mol Ther* **14**:45–53.
59. **Johnson J. E., and A. Schneemann.** 1997. Nodavirus endopeptidase. *Handbook of proteolytic enzymes*. Academic Press Ltd., London.
60. **Johnson J. S., M. Gentsch, L. Zhang, C. M. P. Ribeiro, B. Kantor, T. Kafri, R. J. Pickles, and R. J. Samulski.** 2011. AAV exploits subcellular stress associated with inflammation, endoplasmic reticulum expansion, and misfolded proteins in models of cystic fibrosis. *PLoS Pathog*. **7**:e1002053.
61. **Jordan D. O.** 1955. The physical properties of nucleic acids. *The Nucleic Acids*. Academic Press Ltd., New York.
62. **Kaludov N., K. E. Brown, R. W. Walters, J. Zabner, and J. A. Chiorini.** 2001. Adeno-Associated Virus Serotype 4 (AAV4) and AAV5 Both Require Sialic Acid Binding for Hemagglutination and Efficient Transduction but Differ in Sialic Acid Linkage Specificity. *Journal of Virology* **75**:6884 –6893.
63. **Kern A., K. Schmidt, C. Leder, O. J. Müller, C. E. Wobus, K. Bettinger, C. W. Von der Lieth, J. A. King, and J. A. Kleinschmidt.** 2003. Identification of a heparin-binding motif on adeno-associated virus type 2 capsids. *J. Virol.* **77**:11072–11081.
64. **Kerr J. R.** 2006. Parvoviruses. Hodder Arnold.
65. **Kim D. E., D. Chivian, and D. Baker.** 2004. Protein structure prediction and analysis using the Robetta server. *Nucleic Acids Res* **32**:W526–531.
66. **Kohl N. E., E. A. Emini, W. A. Schleif, L. J. Davis, J. C. Heimbach, R. A. Dixon, E. M. Scolnick, and I. S. Sigal.** 1988. Active human immunodeficiency virus protease is required for viral infectivity. *Proc. Natl. Acad. Sci. U.S.A.* **85**:4686–4690.
67. **Kramer R. M., and J. D. Sharp.** 1997. Structure, function and regulation of Ca<sup>2+</sup>-sensitive cytosolic phospholipase A2 (cPLA2). *FEBS Lett.* **410**:49–53.

68. **Krissinel E., and K. Henrick.** 2007. Inference of macromolecular assemblies from crystalline state. *J. Mol. Biol.* **372**:774–797.
69. **Kronenberg S., B. Böttcher, C. W. von der Lieth, S. Bleker, and J. A. Kleinschmidt.** 2005. A conformational change in the adeno-associated virus type 2 capsid leads to the exposure of hidden VP1 N termini. *J. Virol.* **79**:5296–5303.
70. **Lakadamyali M., M. J. Rust, and X. Zhuang.** 2004. Endocytosis of influenza viruses. *Microbes Infect.* **6**:929–936.
71. **Laskowski R. A., M. W. MacArthur, D. S. Moss, and J. M. Thornton.** 1993. PROCHECK: a program to check the stereochemical quality of protein structures. *Journal of Applied Crystallography* **26**:283–291.
72. **Lerch T. F., Q. Xie, and M. S. Chapman.** 2010. The structure of adeno-associated virus serotype 3B (AAV-3B): insights into receptor binding and immune evasion. *Virology* **403**:26–36.
73. **Levy H. C., V. D. Bowman, L. Govindasamy, R. McKenna, K. Nash, K. Warrington, W. Chen, N. Muzyczka, X. Yan, T. S. Baker, and M. Agbandje-McKenna.** 2009. Heparin binding induces conformational changes in Adeno-associated virus serotype 2. *J. Struct. Biol.* **165**:146–156.
74. **Lombardo E., J. C. Ramírez, J. Garcia, and J. M. Almendral.** 2002. Complementary roles of multiple nuclear targeting signals in the capsid proteins of the parvovirus minute virus of mice during assembly and onset of infection. *J. Virol.* **76**:7049–7059.
75. **Maguire A. M., F. Simonelli, E. A. Pierce, E. N. Pugh, F. Mingozi, J. Bennicelli, S. Banfi, K. A. Marshall, F. Testa, E. M. Surace, S. Rossi, A. Lyubarsky, V. R. Arruda, B. Konkle, E. Stone, J. Sun, J. Jacobs, L. Dell’Osso, R. Hertle, J. Ma, T. M. Redmond, X. Zhu, B. Hauck, O. Zeleniaia, K. S. Shindler, M. G. Maguire, J. F. Wright, N. J. Volpe, J. W. McDonnell, A. Auricchio, K. A. High, and J. Bennett.** 2008. Safety and Efficacy of Gene Transfer for Leber’s Congenital Amaurosis. *New England Journal of Medicine* **358**:2240–2248.
76. **Mani B., C. Baltzer, N. Valle, J. M. Almendral, C. Kempf, and C. Ros.** 2006. Low pH-dependent endosomal processing of the incoming parvovirus minute virus of mice virion leads to externalization of the VP1 N-terminal sequence (N-VP1), N-VP2 cleavage, and uncoating of the full-length genome. *J. Virol.* **80**:1015–1024.
77. **Maroto B., N. Valle, R. Saffrich, and J. M. Almendral.** 2004. Nuclear export of the nonenveloped parvovirus virion is directed by an unordered protein signal exposed on the capsid surface. *J. Virol.* **78**:10685–10694.

78. **Matsui T., H. Tsuruta, and J. E. Johnson.** 2010. Balanced electrostatic and structural forces guide the large conformational change associated with maturation of T = 4 virus. *Biophys. J.* **98**:1337–1343.
79. **McLaughlin S. K., P. Collis, P. L. Hermonat, and N. Muzyczka.** 1988. Adeno-associated virus general transduction vectors: analysis of proviral structures. *Journal of Virology* **62**:1963 –1973.
80. **McNeil H. J., P. E. Shewen, R. Y. C. Lo, J. A. Conlon, and M. W. Miller.** 2003. Novel protease produced by a *Pasteurella trehalosi* serotype 10 isolate from a pneumonic bighorn sheep: characteristics and potential relevance to protection. *Veterinary Microbiology* **93**:145–152.
81. **McPherson A.** 1989. Preparation and analysis of protein crystals. R.E. Krieger Pub. Co.
82. **Miller E. B., B. Gurda-Whitaker, L. Govindasamy, R. McKenna, S. Zolotukhin, N. Muzyczka, and M. Agbandje-McKenna.** 2006. Production, purification and preliminary X-ray crystallographic studies of adeno-associated virus serotype 1. *Acta Crystallographica Section F Structural Biology and Crystallization Communications* **62**:1271–1274.
83. **Mitchell M., H.-J. Nam, A. Carter, A. McCall, C. Rence, A. Bennett, B. Gurda, R. McKenna, M. Porter, Y. Sakai, B. J. Byrne, N. Muzyczka, G. Aslanidi, S. Zolotukhin, and M. Agbandje-McKenna.** 2009. Production, purification and preliminary X-ray crystallographic studies of adeno-associated virus serotype 9. *Acta Crystallographica Section F Structural Biology and Crystallization Communications* **65**:715–718.
84. **Mori S., L. Wang, T. Takeuchi, and T. Kanda.** 2004. Two novel adeno-associated viruses from cynomolgus monkey: pseudotyping characterization of capsid protein. *Virology* **330**:375–383.
85. **Mount J. D., R. W. Herzog, D. M. Tillson, S. A. Goodman, N. Robinson, M. L. McClelland, D. Bellinger, T. C. Nichols, V. R. Arruda, C. D. Lothrop, and K. A. High.** 2002. Sustained phenotypic correction of hemophilia B dogs with a factor IX null mutation by liver-directed gene therapy. *Blood* **99**:2670 –2676.
86. **Nam H.-J., B. L. Gurda, R. McKenna, M. Potter, B. Byrne, M. Salganik, N. Muzyczka, and M. Agbandje-McKenna.** 2011. Structural studies of adeno-associated virus serotype 8 capsid transitions associated with endosomal trafficking. *J. Virol.* **85**:11791–11799.
87. **Nam H.-J., M. D. Lane, E. Padron, B. Gurda, R. McKenna, E. Kohlbrenner, G. Aslanidi, B. Byrne, N. Muzyczka, S. Zolotukhin, and M. Agbandje-McKenna.** 2007. Structure of Adeno-Associated Virus Serotype 8, a Gene Therapy Vector. *Journal of Virology* **81**:12260 –12271.

88. **Ng R., L. Govindasamy, B. L. Gurda, R. McKenna, O. G. Kozyreva, R. J. Samulski, K. N. Parent, T. S. Baker, and M. Agbandje-McKenna.** 2010. Structural characterization of the dual glycan binding adeno-associated virus serotype 6. *J. Virol.* **84**:12945–12957.
89. **Opie S. R., K. H. Warrington Jr, M. Agbandje-McKenna, S. Zolotukhin, and N. Muzyczka.** 2003. Identification of amino acid residues in the capsid proteins of adeno-associated virus type 2 that contribute to heparan sulfate proteoglycan binding. *J. Virol.* **77**:6995–7006.
90. **Otwinowski Z., and W. Minor.** 1997. Processing of X-ray diffraction data collected in oscillation mode, p. 307–326. *In* *Macromolecular Crystallography Part A.* Academic Press.
91. **Pacak C. A., C. S. Mah, B. D. Thattaliyath, T. J. Conlon, M. A. Lewis, D. E. Cloutier, I. Zolotukhin, A. F. Tarantal, and B. J. Byrne.** 2006. Recombinant Adeno-Associated Virus Serotype 9 Leads to Preferential Cardiac Transduction In Vivo. *Circulation Research* **99**:e3 –e9.
92. **Di Pasquale G., and J. A. Chiorini.** 2006. AAV transcytosis through barrier epithelia and endothelium. *Mol. Ther.* **13**:506–516.
93. **Di Pasquale G., B. L. Davidson, C. S. Stein, I. Martins, D. Scudiero, A. Monks, and J. A. Chiorini.** 2003. Identification of PDGFR as a receptor for AAV-5 transduction. *Nat. Med.* **9**:1306–1312.
94. **Patterson S., and J. S. Oxford.** 1986. Early interactions between animal viruses and the host cell: relevance to viral vaccines. *Vaccine* **4**:79–90.
95. **Petit S., N. Lejal, J.-C. Huet, and B. Delmas.** 2000. Active Residues and Viral Substrate Cleavage Sites of the Protease of the Birnavirus Infectious Pancreatic Necrosis Virus. *J. Virol.* **74**:2057–2066.
96. **Pettersen E. F., T. D. Goddard, C. C. Huang, G. S. Couch, D. M. Greenblatt, E. C. Meng, and T. E. Ferrin.** 2004. UCSF Chimera--a visualization system for exploratory research and analysis. *J Comput Chem* **25**:1605–1612.
97. **Pettersen E. F., T. D. Goddard, C. C. Huang, G. S. Couch, D. M. Greenblatt, E. C. Meng, and T. E. Ferrin.** 2004. UCSF Chimera--a visualization system for exploratory research and analysis. *J Comput Chem* **25**:1605–1612.

98. **Quesada O., B. Gurda, L. Govindasamy, R. McKenna, E. Kohlbrenner, G. Aslanidi, S. Zolotukhin, N. Muzyczka, and M. Agbandje-McKenna.** 2007. Production, purification and preliminary X-ray crystallographic studies of adeno-associated virus serotype 7. *Acta Crystallographica Section F Structural Biology and Crystallization Communications* **63**:1073–1076.
99. **Rabinowitz J. E., F. Rolling, C. Li, H. Conrath, W. Xiao, X. Xiao, and R. J. Samulski.** 2002. Cross-Packaging of a Single Adeno-Associated Virus (AAV) Type 2 Vector Genome into Multiple AAV Serotypes Enables Transduction with Broad Specificity. *Journal of Virology* **76**:791–801.
100. **Reguera J., E. Grueso, A. Carreira, C. Sánchez-Martínez, J. M. Almendral, and M. G. Mateu.** 2005. Functional relevance of amino acid residues involved in interactions with ordered nucleic acid in a spherical virus. *J. Biol. Chem.* **280**:17969–17977.
101. **Rivera V. M., G. Gao, R. L. Grant, M. A. Schnell, P. W. Zoltick, L. W. Rozamus, T. Clackson, and J. M. Wilson.** 2005. Long-term pharmacologically regulated expression of erythropoietin in primates following AAV-mediated gene transfer. *Blood* **105**:1424–1430.
102. **Ros C., C. Baltzer, B. Mani, and C. Kempf.** 2006. Parvovirus uncoating in vitro reveals a mechanism of DNA release without capsid disassembly and striking differences in encapsidated DNA stability. *Virology* **345**:137–147.
103. **Ros C., and C. Kempf.** 2004. The ubiquitin-proteasome machinery is essential for nuclear translocation of incoming minute virus of mice. *Virology* **324**:350–360.
104. **Rudnick J., and R. Bruinsma.** 2005. Icosahedral packing of RNA viral genomes. *Phys. Rev. Lett.* **94**:038101.
105. **Sanlioglu S., P. K. Benson, J. Yang, E. M. Atkinson, T. Reynolds, and J. F. Engelhardt.** 2000. Endocytosis and Nuclear Trafficking of Adeno-Associated Virus Type 2 Are Controlled by Rac1 and Phosphatidylinositol-3 Kinase Activation. *Journal of Virology* **74**:9184–9196.
106. **Schmidt M., A. Voutetakis, S. Afione, C. Zheng, D. Mandikian, and J. A. Chiorini.** 2008. Adeno-associated virus type 12 (AAV12): a novel AAV serotype with sialic acid- and heparan sulfate proteoglycan-independent transduction activity. *J. Virol.* **82**:1399–1406.
107. **Scott D. L., Z. Otwinowski, M. H. Gelb, and P. B. Sigler.** 1990. Crystal structure of bee-venom phospholipase A2 in a complex with a transition-state analogue. *Science* **250**:1563–1566.

108. **Seisenberger G., M. U. Ried, T. Endress, H. Büning, M. Hallek, and C. Bräuchle.** 2001. Real-time single-molecule imaging of the infection pathway of an adeno-associated virus. *Science* **294**:1929–1932.
109. **Shen X., T. Storm, and M. A. Kay.** 2007. Characterization of the relationship of AAV capsid domain swapping to liver transduction efficiency. *Mol. Ther.* **15**:1955–1962.
110. **Singer A. G., F. Ghomashchi, C. Le Calvez, J. Bollinger, S. Bezzine, M. Rouault, M. Sadilek, E. Nguyen, M. Lazdunski, G. Lambeau, and M. H. Gelb.** 2002. Interfacial kinetic and binding properties of the complete set of human and mouse groups I, II, V, X, and XII secreted phospholipases A2. *J. Biol. Chem.* **277**:48535–48549.
111. **Sonntag F., S. Bleker, B. Leuchs, R. Fischer, and J. A. Kleinschmidt.** 2006. Adeno-associated virus type 2 capsids with externalized VP1/VP2 trafficking domains are generated prior to passage through the cytoplasm and are maintained until uncoating occurs in the nucleus. *J. Virol.* **80**:11040–11054.
112. **Stahelin R. V.** 2009. Lipid binding domains: more than simple lipid effectors. *J. Lipid Res.* **50 Suppl**:S299–304.
113. **Stahnke S., K. Lux, S. Uhrig, F. Kreppel, M. Hösel, O. Coutelle, M. Ogris, M. Hallek, and H. Büning.** 2011. Intrinsic phospholipase A2 activity of adeno-associated virus is involved in endosomal escape of incoming particles. *Virology* **409**:77–83.
114. **Suikkanen S., T. Aaltonen, M. Nevalainen, O. Välilehto, L. Lindholm, M. Vuento, and M. Vihinen-Ranta.** 2003. Exploitation of microtubule cytoskeleton and dynein during parvoviral traffic toward the nucleus. *J. Virol.* **77**:10270–10279.
115. **Suikkanen S., M. Antila, A. Jaatinen, M. Vihinen-Ranta, and M. Vuento.** 2003. Release of canine parvovirus from endocytic vesicles. *Virology* **316**:267–280.
116. **Summerford C., and R. J. Samulski.** 1998. Membrane-associated heparan sulfate proteoglycan is a receptor for adeno-associated virus type 2 virions. *J. Virol.* **72**:1438–1445.
117. **Thomas C. E., T. A. Storm, Z. Huang, and M. A. Kay.** 2004. Rapid uncoating of vector genomes is the key to efficient liver transduction with pseudotyped adeno-associated virus vectors. *J. Virol.* **78**:3110–3122.

118. **Thompson J. D., D. G. Higgins, and T. J. Gibson.** 1994. CLUSTAL W: improving the sensitivity of progressive multiple sequence alignment through sequence weighting, position-specific gap penalties and weight matrix choice. *Nucleic Acids Res.* **22**:4673–4680.
119. **Vihinen-Ranta M., D. Wang, W. S. Weichert, and C. R. Parrish.** 2002. The VP1 N-terminal sequence of canine parvovirus affects nuclear transport of capsids and efficient cell infection. *J. Virol.* **76**:1884–1891.
120. **Walters R. W., M. Agbandje-McKenna, V. D. Bowman, T. O. Moninger, N. H. Olson, M. Seiler, J. A. Chiorini, T. S. Baker, and J. Zabner.** 2004. Structure of Adeno-Associated Virus Serotype 5. *Journal of Virology* **78**:3361 –3371.
121. **Walters R. W., S. M. P. Yi, S. Keshavjee, K. E. Brown, M. J. Welsh, J. A. Chiorini, and J. Zabner.** 2001. Binding of Adeno-associated Virus Type 5 to 2,3-Linked Sialic Acid Is Required for Gene Transfer. *Journal of Biological Chemistry* **276**:20610 –20616.
122. **Warrington K. H. Jr, O. S. Gorbatyuk, J. K. Harrison, S. R. Opie, S. Zolotukhin, and N. Muzyczka.** 2004. Adeno-associated virus type 2 VP2 capsid protein is nonessential and can tolerate large peptide insertions at its N terminus. *J. Virol.* **78**:6595–6609.
123. **Welbourn S., and A. Pause.** 2007. The hepatitis C virus NS2/3 protease. *Curr Issues Mol Biol* **9**:63–69.
124. **White S., D. Scott, Z. Otwinowski, M. Gelb, and P. Sigler.** 1990. Crystal structure of cobra-venom phospholipase A2 in a complex with a transition-state analogue. *Science* **250**:1560 –1563.
125. **Wistuba A., S. Weger, A. Kern, and J. A. Kleinschmidt.** 1995. Intermediates of adeno-associated virus type 2 assembly: identification of soluble complexes containing Rep and Cap proteins. *J. Virol.* **69**:5311–5319.
126. **Witz J., and F. Brown.** 2001. Structural dynamics, an intrinsic property of viral capsids. *Arch. Virol.* **146**:2263–2274.
127. **Wobbe C. R., S. Mitra, and V. Ramakrishnan.** 1984. Structure of the capsid of Kilham rat virus from small-angle neutron scattering. *Biochemistry* **23**:6565–6569.
128. **Wobus C. E., B. Hügler-Dörr, A. Girod, G. Petersen, M. Hallek, and J. A. Kleinschmidt.** 2000. Monoclonal Antibodies against the Adeno-Associated Virus Type 2 (AAV-2) Capsid: Epitope Mapping and Identification of Capsid Domains Involved in AAV-2–Cell Interaction and Neutralization of AAV-2 Infection. *J Virol* **74**:9281–9293.

129. **Wu Z., A. Asokan, J. C. Grieger, L. Govindasamy, M. Agbandje-McKenna, and R. J. Samulski.** 2006. Single amino acid changes can influence titer, heparin binding, and tissue tropism in different adeno-associated virus serotypes. *J. Virol.* **80**:11393–11397.
130. **Xiao W., K. H. Warrington Jr, P. Hearing, J. Hughes, and N. Muzyczka.** 2002. Adenovirus-facilitated nuclear translocation of adeno-associated virus type 2. *J. Virol.* **76**:11505–11517.
131. **Xie Q., W. Bu, S. Bhatia, J. Hare, T. Somasundaram, A. Azzi, and M. S. Chapman.** 2002. The atomic structure of adeno-associated virus (AAV-2), a vector for human gene therapy. *Proceedings of the National Academy of Sciences* **99**:10405 –10410.
132. **Xue B., R. L. Dunbrack, R. W. Williams, A. K. Dunker, and V. N. Uversky.** 2010. PONDR-FIT: a meta-predictor of intrinsically disordered amino acids. *Biochim. Biophys. Acta* **1804**:996–1010.
133. **Yan Z., R. Zak, G. W. G. Luxton, T. C. Ritchie, U. Bantel-Schaal, and J. F. Engelhardt.** 2002. Ubiquitination of both adeno-associated virus type 2 and 5 capsid proteins affects the transduction efficiency of recombinant vectors. *J. Virol.* **76**:2043–2053.
134. **Zádori Z., J. Szelei, M. C. Lacoste, Y. Li, S. Gariépy, P. Raymond, M. Allaire, I. R. Nabi, and P. Tijssen.** 2001. A viral phospholipase A2 is required for parvovirus infectivity. *Dev. Cell* **1**:291–302.
135. **Zolotukhin S., M. Potter, I. Zolotukhin, Y. Sakai, S. Loiler, T. J. Fraiters Jr, V. A. Chiodo, T. Phillipsberg, N. Muzyczka, W. W. Hauswirth, T. R. Flotte, B. J. Byrne, and R. O. Snyder.** 2002. Production and purification of serotype 1, 2, and 5 recombinant adeno-associated viral vectors. *Methods* **28**:158–167.
136. (IUCr) ATSAS 2.1 - towards automated and web-supported small-angle scattering data analysis.
137. 1994. The CCP4 suite: programs for protein crystallography. *Acta Crystallogr. D Biol. Crystallogr.* **50**:760–763.

## BIOGRAPHICAL SKETCH

Bala completed his Bachelor in Technology (B. Tech.) in industrial biotechnology at Anna University, Chennai, India in 2007. His undergrad research (under the guidance of Dr. Pennathur Gautham) was on the systemic bioleaching of lignite by acidophilus bacteria. He joined the IDP at the University of Florida in August 2007. After a set of rotations, he joined the McKenna Lab and the Department of Biochemistry and Molecular Biology in April 2008. His doctoral thesis was on pH-mediated structural transitions in Adeno-Associated Viruses. His areas of interest include Structural Virology, Macromolecular Crystallography, Molecular Biophysics and Enzymology. His interests outside academics include sports, music, computers, animal care and community service.